Atomic Structure and Dynamics of Defects in Transition Metal Dichalcogenide Bilayers

Si Zhou

Department of Materials

Linacre College

University of Oxford

Supervisor: Prof. Jamie H. Warner

Submitted in Conformity with the Requirements

for the Degree of DPhil in Materials Science

Declaration

The material contained within this thesis has not previously been submitted for a degree at the University of Oxford or any other university. The research reported within this thesis has been conducted by the author unless indicated otherwise.

Copyright Notice

Abstract

Transition metal dichalcogenides (TMDs), such as MoS_2 and WS_2, are direct band gap semiconductors in their monolayer form and indirect band gap semiconductors in bulk. They offer band gaps in the red visible spectrum and semiconducting properties that expand the application of the two-dimensional (2D) materials beyond what graphene alone can achieve. These layered materials are stacked through weak interlayer van der Waals interactions. Their bilayer structures offer an extra layer degree of freedom, which introduces performance enhancements compared to their monolayer counterpart. Interaction between MoS_2 or WS_2 layers as well as the specific stacking arrangement can significantly modify their electrical, optical and vibrational properties. The presence of defective structures has been proved to exert significant influences on TMD monolayers. Understanding the atomic structures and the dynamics of these defects in layered materials and their differences from those in monolayers is important for revealing their impact on TMD bilayers, leading approaches for their future device application.

Aberration-corrected transmission electron microscopy (AC-TEM) is one of the leading approaches to study the atomic structure of defects on 2D materials, laying the foundation for the first experiment, which involves the production and aggregation as well as observation of vacancies and line defects in differently stacked MoS_2 bilayers at atomic-level resolution. DFT calculated models prove the main discrepancy between defective monolayer and bilayer systems, which is assigned to the interlayer van der Waals force in the bilayer system. In the next experiment, we move forward to probe the atomic structure of a more complex defective structure, the anti-phase grain boundary in MoS_2 bilayers using annular dark field scanning transmission electron microscopy (ADF-STEM). Our results show the anti-phase GB in the

bottom layer leads to the coexistence of both 2H and 3R stacking in the same bilayer domain, which is attributed to the lattice compression in the dislocation core due to the interlayer van der Waals force in the bilayer system. In the next experiment, the use of *in-situ* heating holder in the ADF-STEM makes the direct visualization of atomic structures and dynamics at elevated temperatures possible. Surface ripples, which are also denoted as stacking boundaries due to their morphologies in bilayer systems are analyzed at both micrometer and nanometer levels. These surface ripples introduce two perfect stacking orders with nanometer-wide transition regions, the morphology of which is decided by the interlayer van der Waals forces. The reversibility of these structures under temperature perturbation and beam irradiation is also studied.

Acknowledgement

I would like to deliver my sincere gratitude to my supervisor Prof. Jamie H. Warner, who provided a valuable supervision over my DPhil studies and research. I remember the first day I joined his group, he showed us his passion and rigorous attitude towards science, which greatly inspired me as a fresher in 2D materials studies. As I finished writing up my first paper in year one, he offered generous help in reconstructing the whole paper and guiding me to seek for the key sciences underlying the plain data and how to tell the whole story in a proper logic flow. I would also like to acknowledge his patience and generosity in supporting my DPhil projects such as training my skills in using TEM and relevant image processing methods, which, during the past few years, has shaped my understanding in scientific research.

I also owe my acknowledgement to my collaborators and colleagues, who attributed their expertise and knowledge to my DPhil research. Prof. Jeffery Grossman, Dr. Huashan Li and Dr. Shi Zhe at Massachusetts Institute of Technology provided substantial contributions on theoretical calculations which have been crucial in supporting my experimental observations; Dr. Hidetaka Sawada, Prof. Angus Kirkland, Dr. Christopher Allen and Dr. Mohsen Danaie at Diamond Light source and Dr. Shanshan Wang and Dr. Chuncheng Gong at University of Oxford consistently trained me on TEM operation skills of JEOL-2200, JEOL-2100, ARM 300F and ARM 200F as well as corresponding image analysis methods; Ms Wenshuo Xu has always been helpful in training my CVD synthesis and sample transfer skills, securing the bilayer sample quality for the subsequent atomic-level observation.

I want to express a special thank to my families. My parents have always been supportive for my decisions. They could argue or disagree at times, but not once pushed me to live a life I repel. My father spent his whole life on improving our life quality and my mother gave up her career decades ago to raise my sister and me. The dedication they made for this family is imprinted in my mind. My wife, Mengge Chen, a special girl from my hometown who stepped into my life 17 years ago, is also currently doing her DPhil in History Faculty at University of Oxford. I am thankful for her companion all these years and her courage and assistance whatever obstacles came up. We had issues during my final DPhil year and I am happy we came through. Hopefully, we could finish our DPhil studies in the same year and get ready to embrace the next chapter in our life.

Publications

My accomplished works during DPhil studies are listed as below, which include works published, submitted or close to be submitted.

Chapter 4

1. **Zhou, S.**; Wang, S.; Li, H.; Xu, W.; Gong, C.; Grossman, J.C.; Warner, J.H. Atomic structure and Dynamics of Defects in 2D MoS_2 Bilayers. *ACS Omega* **2017**, *2*,3315-3324.

Chapter 5

2. **Zhou, S.**; Wang, S.; Shi, Z.; Sawada, H.; Kirkland, A. I.; Li, J.; Warner, J. H. Atomically Sharp Interlayer Stacking Shifts at Anti-phase Grain Boundaries in Overlapping MoS_2 Secondary Layers. *Nanoscale* **2018**, *10*, 16692-16702.

Chapter 6

3. **Zhou, S.**; Wang, S.; Chen, J.; Warner, J. H. In-situ High Temperature Observation of Surface Ripples in Transition Metal Dichalcogenide Bilayers. *Journal of Materials Research* **2019**, *399*,1-10.

Co-Author

4. Chen, J.; **Zhou, S.**; Wen, Y.; Ryu, G. H.; Allen, C.; Lu, Y.; Warner, J. H. *In-situ* High Temperature Atomic Level Dynamics of Large Inversion Domain Formations in Monolayer MoS_2. *Nanoscale* **2019**, *11*, 1901-1913.

5. Xu, W.; Li, S.; **Zhou, S.**; Lee, J. K.; Wang, S.; Sarwat, S. G.; Wang, X.; Bhaskaran, H.; Pasta, M.; Warner, J. H. Large Dendritic Monolayer MoS_2 Grown by Atmospheric Pressure

Chemical Vapor Deposition for Electrocatalysis. *ACS Appl. Mater. Interfaces* **2018**, *10*, 4630–4639.

6. Li, S.; Lee, J. K.; **Zhou, S.**; Pasta, M.; Warner, J. H. Synthesis of Surface Grown Pt Nanoparticles on Edge-Enriched MoS_2 Porous Thin Films for Enhancing Electrochemical Performance. *Chemistry of Materials* **2019**, *31*, 387-397.

7. Chen, Q.; Li, H.; **Zhou, S.**; Xu, W.; Chen, J.; Sawada, H.; Warner, J. H. Ultralong 1D Vacancy Channels for Rapid Atomic Migration during 2D Void Formation in Monolayer MoS_2. *ACS nano* **2019**, *12*, 7721-7730.

8. Ryu, G. H.; France-Lanord, A.; Wen, Y.; **Zhou, S.**; Grossman, J. C.; Warner, J. H. Atomic Structure and Dynamics of Self-Limiting Sub-Nanometer Pores in Monolayer WS_2. *ACS nano* **2018**, *12*, 11638-11647.

9. Wang, S.; Sawada, H.; Han, X.; **Zhou, S.**; Li, S.; Guo, Z. X.; Warner, J. H. Preferential Pt Nanocluster Seeding at Grain Boundary Dislocations in Polycrystalline Monolayer MoS_2. *ACS nano* **2018**, *12*, 5626-5636.

10. Sinha, S.; Sheng, Y.; Griffiths, I.; Young, N. P.; **Zhou, S.**, Kirkland, A. I.; Warner, J. H. *In-Situ* Atomic-Level Studies of Gd Atom Release and Migration on Graphene from a Metallofullerene Precursor. *ACS nano* **2018**, *12*, 10439-10451.

11. Chen, T.; Zhou, Y.; Sheng, Y.; Wang, X.; **Zhou, S.**; Warner, J. H. Hydrogen-Assisted Growth of Large-Area Continuous Films of MoS_2 on Monolayer Graphene. *ACS Appl. Mater. Interfaces* **2018**, *10*, 7304-7314.

Table of Contents

Chapter 1

Introduction

1.1 Project Aims

The objective of this doctorate project is to systematically study the defective structures in Transition metal dichalcogenide (TMD) bilayers such as MoS_2 and WS_2, including their atomic structures, dynamics and behavior differences from those in the monolayer counterparts due to the interlayer van der Waals Force.

1.2 Thesis Scope

This thesis covers my research on TMD bilayers over the past 4 years at the Department of Materials and Linacre College, University of Oxford. It begins with a comprehensive review of work been accomplished in 2D materials, especially the defective structures in molybdenum disulfide (MoS_2) and tungsten disulfide (WS_2) in both their monolayer and bilayer forms. Transmission electron microscopy (TEM), as the key characterization technique for my investigation, the development of which is also summarized. The methodologies applied to my doctorate studies are discussed in detail in Chapter 3 including sample preparation and transfer, Optical, TEM observation and data acquisition and subsequent image analysis.

Imaging the lattice and defective structures in MoS_2 and WS_2 bilayers at atomic resolution is achieved using Oxford-JEOL 2200 Monochromated AC-TEM with corrected spherical and chromatic aberration. In Chapter 4, I started with imaging the 2H and 3R stacked lattice

under different defocus value and identifying both single and double sulfur vacancies by their unique contrast differences. The vacancies exist in both layers and can migrate between layers. As they aggregate into line defects with different lengths and widths, their configuration is studied in-depth. This first part of my work shows how defective structures in bilayer system, starting from the simplest ones, can differ from those in the monolayer system.

In Chapter 5, I moved forward to a more complex defect, the grain boundary, which was frequently investigated in graphene and TMD monolayers, but scarcely studied in TMD bilayers. The anti-phase grain boundary (GB), which introduces a 60º lattice rotation in monolayers, leads to a sharp interlayer boundary between 2H and 3R stacked domains. Their coexistence in the same bilayer region is achieved due to interlayer van der Waals force. The ‘meandering’ configuration of this GB is traced and the its direction is proved to be tunable by controlling the dislocation cores. Formation mechanism of these GBs in bilayers are also revealed for their controllable growth for future device uses.

During my observation, for MoS_2 and WS_2 bilayers, two identical or distinct perfect stacking can also exist with a few-nanometer wide stacking boundary, rather than a sharp interface such as the anti-phase GB. The boundaries are proved as surface ripples which nucleate mainly from strain introduction to the bilayer system. As illustrated in Chapter 6, these surface ripples are investigated at both micrometer and nanometer scales, the morphology of which is decided by the interlayer can der Waal forces. Under temperature perturbation and beam irradiation, the nucleation and annihilation of these stacking boundaries are proved to be controllable.

My whole doctorate work has been forcusing on the defective structures in bilayers and their differences compared with those existing in monolayers, laying foundation for the controlled nanoengineering of TMD bilayer-based devices. These conclusions and outlooks are summarized in Chapter 7.

Chapter 2

Literature review

2.1 Introduction

This chapter unfolds a comprehensive overview of works on Transition Metal Dichalcogenide monolayers and bilayers, mainly focusing on the atomic-level structure studies of defects using advanced imaging technologies such as scanning transmission electron microscopy (STEM) and aberration-corrected transmission electron microscopy (AC-TEM) and their dynamic studies using in-situ heating method.

2.2 Transition Metal Dichalcogenide

Two-dimensional nanomaterials become eye-catching due to their potential applications in next-generation optoelectronics devices and nanoelectronics.[1-5] Graphene, as the first 2D material available to us, has been widely used in optical electronics, biological engineering and energy storage areas.[6-8] In recent decades, the scientific community builds interest in two-dimensional materials beyond graphene, especially transition metal dichalcogenides (TMDs) due to their attractive electronic and optical properties.[9-11]

2.2.1 An Overview of TMDs

Hexagonal boron nitride (h-BN) and Graphene have been attracting a large amount of attention due to their unique properties. Since becoming popular back in 2004, graphene, boasting unique excellent electrical conductivity, electric structure and outstanding strength, was evaluated as “a rapid rising star on the horizon of material science”.[12]

However, it has no band gap, which limited the applications of this “rising star”. There were several attempts to solve this problem, namely to introduce this band gap: cutting graphene into nanoribbons, antidot engineering or chemical doping.[13-20] As a tradeoff, its superior conductivity is lost when a band gap is introduced into graphene by these methods. Unlike insulating hexagonal boron nitride (h-BN) and conductive graphene,[21-22] atomic-layered TMDs are semiconductor materials with required bandgaps, making it possible to fabricate devices with higher performance and lower power consumption.[23-25] With h-BN as insulators, graphene as conductors and TMDs as semiconductors, they make three basic building blocks available for nanoelectronics.

TMDs are layered materials hold together by weak van de Waals force.[26] As shown in **Figure 2-1**, the typical structural formula for TMDs is MX_2, where M stands for transitional metals such as W, Ti, Mo and X for chalcogenides like Se, Te, S.[27] MoS_2 and WS_2 monolayers, as the most intensively studied, show fairly high mobility, excellent mechanical characteristics, and outstanding optical properties. These intriguing properties can find use in gas sensors, logical devices, photodetectors, flexible electronics as well as transistors.[28-41] MoS_2 was the first semiconducting TMD obtained in a monolayer form. When decreasing its thickness from bulk to a layer, MoS_2 transforms its band structure from an indirect bandgap to a direct one, making it complementary to the zero-bandgap graphene and behave as a promising candidate in nanoelectronic and optoelectronic applications.[42-47] Furthermore, 2D MoS_2 can perform as a low-cost, highly efficient electrocatalyst for hydrogen evolution reaction, an activity that can be further promoted by the increase of edge sites and defect density as well as proper heteroatom substitutional doping.[48-51]

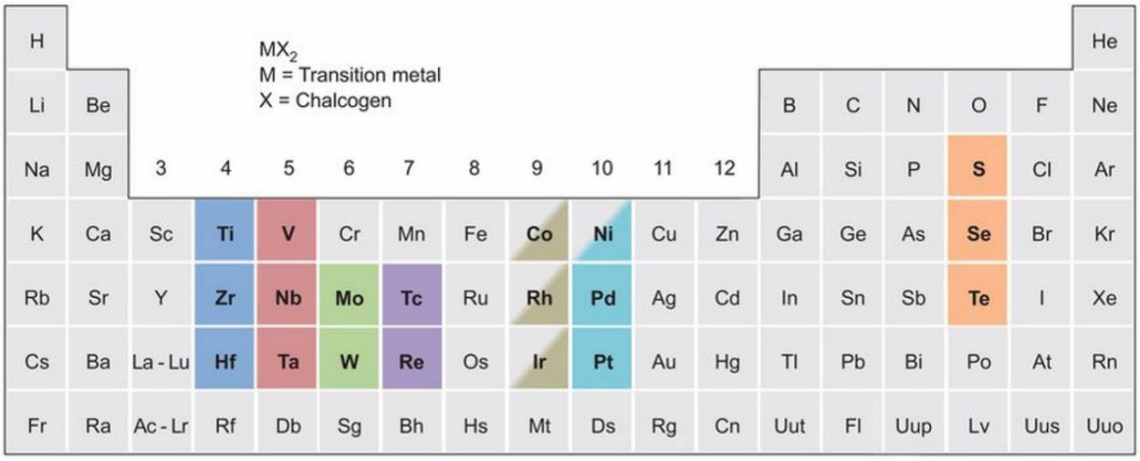

Figure 2-1 Periodic table showing the diversity of TMDs. The transition metals that are fully highlighted predominantly crystallize into layered structures with three chalcogen elements, while those partially highlighted (Co, Rh, Ir and Ni) can form some non-layered structures. Reprinted with permission from ref. 27 © 2013 Macmillan Publishers Limited.

For monolayer and few-layer TMD synthesis, there are two main strategies: top-down and bottom-up, each of which includes various methods. For top-down fabrication, physical or chemical-based processes can be utilized to break the van der Waals forces between layers of a crystal, in order to isolate single or a few layers. Novoselov et al. mechanically exfoliated various single-layer 2D crystals from bulk materials, such as $NbSe_2$, graphite, MoS_2, BN in 2004.[1] However, they found limitations in device application since TMDs prepared by this method have quite small size at micron scale. Alternatively, chemical exfoliation method, which produces TMD nanosheets in solution phase, has been developed to realize high-yield and large-scale. Coleman and co-workers demonstrated that bulk TMD crystals can be effectively exfoliated by direct sonication in common solvents (e.g. N-methyl-pyrrolidone [NMP] and dimethylformamide [DMF]).[52-55] A number of single or a few-layer TMD nanosheets were prepared from their bulk crystals using this method, examples such as MoS_2, WS_2, $MoTe_2$, $MoSe_2$, $NiTe_2$, $TaSe_2$, and $NbSe_2$. However, the yield of single-layer sheets produced by these methods is still low due to limitations of

the sonication process, and the lateral size of the sheets ranges from several nm to several hundred μm, which is relatively small. In the 1970s, the intercalation of layered TMDs with n-butyllithium in hexane followed by exfoliation in water via sonication was developed to produce single-layer TMD nanosheets.[56-59] In this process, the lithium (Li) ions were intercalated into the layered spacing, and they reacted with the TMDs to form Li-intercalated compounds (e.g. for MoS_2, the compound is $LixMoS_2$, where x is the number of Li atoms). The Li-intercalated compounds were then sonicated in water or ethanol to obtain well-dispersed single-layer sheets. In contrast with top-down approaches, bottom-up methods allow 2D crystals to grow into larger sizes with required shapes at a larger scale. The chemical vapor deposition (CVD) method is the most effective way to achieve large-area growth for numerous TMDs.[60-67] There are basically four CVD approaches for growing monolayer or few-layered TMDs which are shown in **Figure 2-2**. The first approach displayed in **Figure 2-2**(a) is a two-step thermolysis process, which is used to obtain high-quality thin film. The thermal decomposition of precursors happens under reductive and inert environment, while the presence of H_2 at low temperature avoids oxidation and converts $(NH_4)_2MoS_4$ precursor directly into MoS_2.[68] The second approach is by sulfurization/selenization/tellurization of pre-deposited metal or metal oxide films on suitable substrate. Metal or metal-containing precursors can be deposited by techniques such as spin coating, and thermal evaporation, e-beam evaporation and atomic layer deposition (ALD). [69-72] As a typical example shown in **Figure 2-2**(b), rhomboidal MoO_2 nucleated and grew on substrate through thermal evaporation, and then was reduced by sulfur vapor at 650-850 °C, and finally MoO_2 was sulfurized to MoS_2 layer-by-layer at higher temperature. A physical vapor transport method shown in **Figure 2-2**(c) is the third approach. For example, the MoS_2 powder are involved as precursor which was kept at higher temperature zone and finally high

quality MoS_2 was deposited on insulating substrate via vapor–solid growth mechanism under Ar gas.[73] The forth approach is the most common techniques to synthesize TMD layers. This CVD method involves vapor phase reaction of transition metal oxides/halides and chalcogen precursors.[74] The three-step reaction for growth of MoS_2 from MoO_3 and sulfur powder are shown in **Figure 2-2**(d).

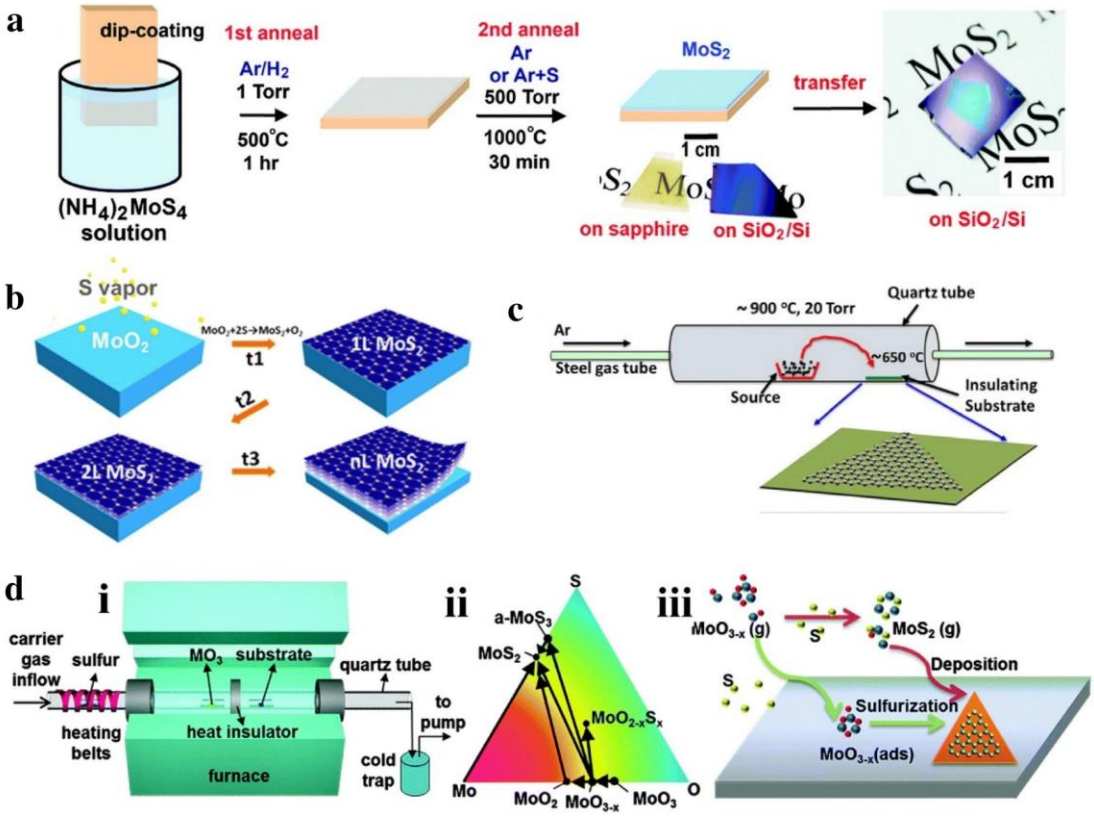

Figure 2-2 4 types of growth routes for TMDs. (a) Two-step thermolysis process synthesis from $(NH_4)_2MoS_4$ precursor on SiO_2/Si or sapphire substrates followed by the two-step annealing process on insulating substrates and finally transferred onto another substrate. Reprinted with permission from ref. 68 © Copyright 2012, American Chemical Society. (b) Layer by layer deposition of MoS_2 from MoO_3 by surface sulfurization and transferred to another substrate one by one. Reprinted with permission from ref. 72 © Copyright 2013, American Chemical Society. (c) Simple vapor transport method showing MoS_2 films were deposited on insulating substrate at high temperature from MoS_2 powder precursor under inert atmosphere. Reprinted with permission from ref. 73 © Copyright 2013, American Chemical Society. (d) (i) LPCVD system setup for TMDs, (ii)

Mo–O–S ternary phase diagram illustrating the pathways for the CVD growth of MoS_2 from MoO_3 precursors, and (iii) Possible growth routes of MoS_2 by the reaction of MoO_{3-x} and S. Reprinted with permission from ref. 74 © Copyright 2015, Royal Society of Chemistry

For monolayer TMDs such as monolayer WS_2 and MoS_2, there are two different crystal symmetries: the 2H (trigonal prismatic D3h) and 1T (octahedral Oh) phases which possess distinct electronic structures.[75] As shown in **Figure 2-3**(a), MoS_2 can exist in two different crystal symmetries, the structures of which have distinct electronic structures. For 2H phase, the hexagonal lattice has three-fold symmetry and ABA (S-Mo-S) atomic stacking sequence. The 1T phase shows a different stacking of ABC (S-Mo-S) with bottom S plane occupying the hollow center of a 2H hexagonal lattice. Normally, exfoliated MoS_2 nanosheets have natural 2H phase while those produced by chemical Li-intercalation transform to the metastable structure 1T.[29] For mechanical exfoliated single-layer MoS_2, 2H and 1T phases coexist.[76] It was found that in MoS_2 monolayer, the 1T and 2H polytype structures can form a chemically monolithic two-dimensional crystalline solid. A selected region with 2H stacking structure can be turned into 1T stacking structure by Li intercalation. The obtained heterostructure is stable after exfoliation and removal of Li atoms. The two phases are coherently bonded to each other, as shown in **Figure 2-3**(b). Experimentally, the difference in the lattice mismatch of the two regions cannot be resolved. This indicates that the phase boundary at the interface is strain-free. The two phases exhibit quite different electronic structures due to the changes in the crystal symmetry: 2H phase is semiconducting, while the 1T phase is metallic,[77-84] Therefore, the obtained heterostructures are highly inhomogeneous, consisting of nanometer-sized semiconducting and metallic domains.

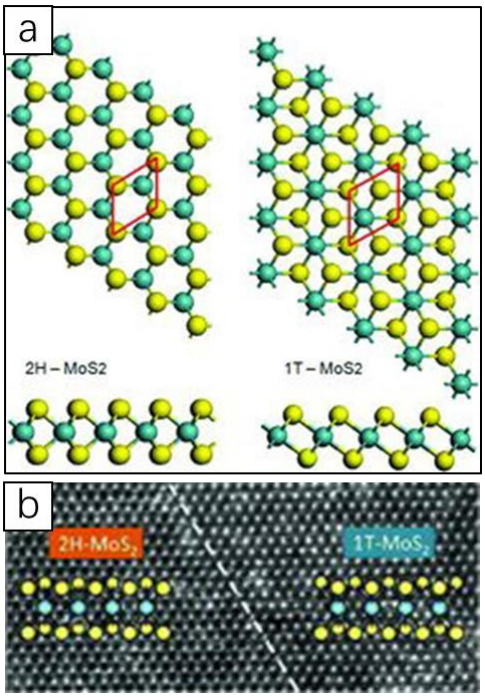

Figure 2-3. Crystal structure of TMD monolayers. (a) Single-layer 2H and 1T polytypes of MoS_2 (top and side view). The outlined unit cell of 2H structure contains one basis atom, while the unit cell of 1T structure contains two basis atoms. The S atoms are light gray/yellow and the Mo atoms are dark gray/blue. (b) Transmission electron microscopy image of the interface between 1T and 2H phases in two-dimensional layer of MoS_2. Reprinted with permission from ref. 75 © Copyright 2015, American Chemical Society.

The electronic band structures of TMD semiconductors directly influence their optical properties. The direct bandgap in TMD monolayers enable them to absorb or emit photons with a much higher efficiency than the multilayers or the bulk.[85-86] Since the radiative recombination rate increases significantly with the decreasing thickness of 2D TMDs, strong photoluminescence (PL) is observed in TMD monolayers owing to their direct bandgaps.[87] The indirect–direct bandgap transition enables the intensity of the PL emission to enhance significantly from a bilayer to a monolayer. As shown in **Figure 2-4**(a) and (b), The PL quantum yield (QY) also increases greatly with the decreasing layer number.[88-89] The pronounced peak in the PL spectrum of monolayer WS_2 is located at 2.0 eV,

corresponding to the emission of A excitons.[87] However, there are two peaks for monolayer MoS_2, which are located at 1.8 eV and 2.0 eV.[85] The energy variation is attributed to the splitting at the valence band maximum in monolayer MoS_2 due to the spin–orbit effect. The direct gap transitions at the K point in the Brillouin zone between the maxima of split valence bands and the minimum of the conduction band, known as A_1 and B_1 transitions, can generate A and B excitons, respectively, upon laser excitation, giving the dominant features in both the PL and the optical absorption spectra of MoS_2.[90-92] The band structure of MoS_2 is contributed by different spatially distributed atomic orbitals from Mo and S atoms as well as their hybridization states, which can be influenced by crystal structure dimensions and element variations with different sensitivities. Therefore, it is easy to understand why the mechanical strain loading and chemical/physical doping are two of the most commonly used approaches for bandgap engineering of monolayer MoS_2.[93-97] The vibrational properties of MoS_2 and WS_2 associated with their phonon dispersions have been calculated by *ab initio*, and have been investigated experimentally by Raman spectroscopy. Raman spectroscopy is non-destructive technique to explore the structural and vibrational properties of TMDs. It relies on the inelastic scattering of materials of monochromatic light. For atomically thin TMDs, E_{2g}^1 and A_{1g} are the two typical Raman signatures. the A_{1g} mode corresponds to the out-of-plane lattice vibration in which metal atoms stay still and two chalcogen atoms move perpendicularly against the atomic plane in opposite direction, while the E_{2g}^1 mode corresponds to in-plane vibration where two chalcogen atoms and metal atom move in the opposite direction within the atomic plane.[98-99] Raman spectroscopy can provide information about van der Waals interactions (e.g. layer number and substrate effect), doping level and lattice strain of MoS_2 mainly through studying the

frequency of characteristic peaks. The Raman spectroscopy of MoS_2 with different layer numbers and monolayer WS_2 are shown in **Figure 2-4**(c) and (d), respectively.

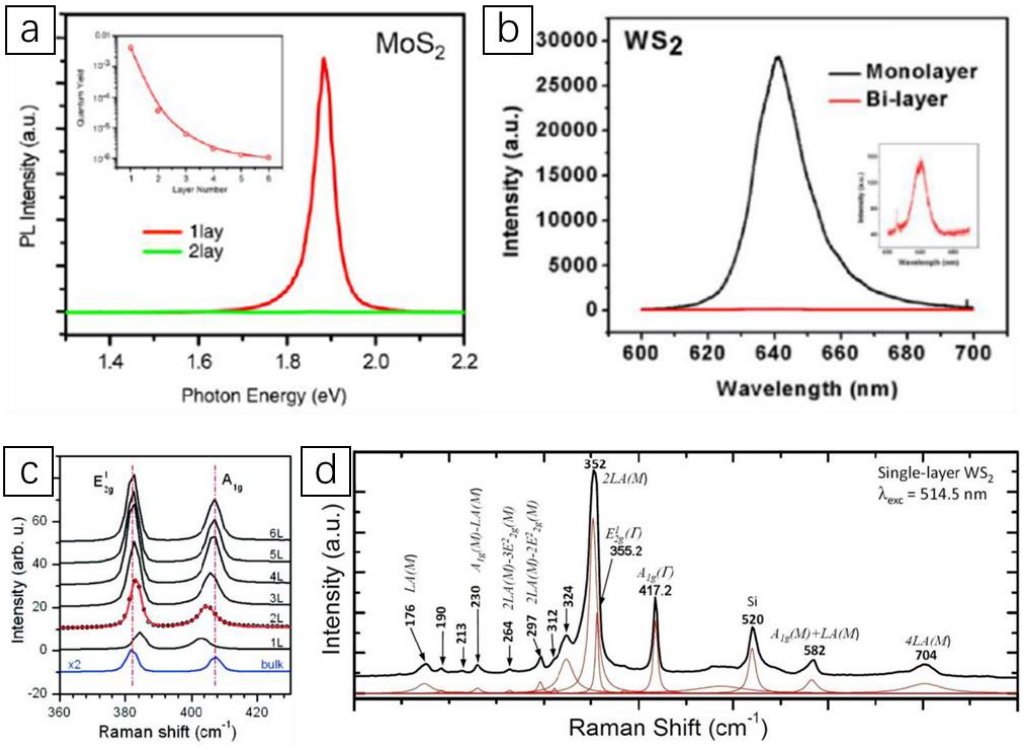

Figure 2-4 PL and Raman spectra of monolayer and few-layer MoS_2 and WS_2. (a) PL spectra for mono- and bilayer MoS_2. Inset: PL QY with the layer number of MoS_2. Reprinted with permission from ref. 88 © Copyright 2010, American Physics Society. (b) PL spectra of mono- and bilayer WS_2. Inset: the magnified PL peak of bilayer WS_2. Reprinted with permission from ref. 89 © Copyright 2015, Nature Publishing Group. (c) Raman spectra of MoS_2 with different layer numbers. Reprinted with permission from ref. 98 © Copyright 2010, American Chemical Society. (d) Raman spectra of monolayer WS_2 with Lorentzian fits. Reprinted with permission from ref. 99 © Copyright 2013, Nature Publishing Group.

2D MoS_2 is reported to possess outstanding mechanical properties by experiments using the Atomic force microscopy (AFM) probe. Bertolazzi et al. measured the stiffness and breaking strength of mechanical exfoliated monolayer MoS_2, yielding an in-plane stiffness of 180±60 Nm^{-1}, which corresponds to an effective Young's modulus of 270±100 GPa.[100]

Such a high Young's modulus is comparable to that of steel (180 GPa). Fracture takes place when an effective strain reaches between 6% and 11% with an average breaking strength of 15±3 Nm^{-1} (23 GPa). Castellanos-Gomez et al. measured the elastic properties of suspended MoS_2 nanosheets having thickness variations from 5 to 25 layers and obtained their average Young's modulus as high as 330 ± 70 GPa.[102] In addition, the transistor made up of MoS_2 thin films exhibits remarkably high flexibility, being capable to preserve its carrier mobility at a curvature of 0.75 mm.[103] The first-principle calculation can also predict the ideal biaxial tensile strength and elastic modulus, which shows a good agreement with experimental observations.[104]

2.2.2 TMD Bilayers

TMDs are stacked through weak interlayer van der Waals interactions. For 2D TMDs such as WS_2 and MoS_2, their bilayer structures offer an extra layer degree of freedom, which introduces performance enhancements compared to the monolayer counterpart. A change from monolayer to bilayer modifies the band structure, providing tunability in electrical, optical, vibrational and chemical properties.[105-108] For instance, it has been reported that few-layer MoS_2 shows higher carrier mobility, better chemical stability and a more sensitive field-induced effect in transistors than its monolayer counterpart.[109-118] The gas sensing behavior of few-layer thick MoS_2 has been found to be better than that of single-layer MoS_2 due to the instability of the single-layer form in reactive gas environments.[119-120] Moreover, the band gap of bilayer MoS_2 can be tuned by applying a vertical electric field.[121] For these reasons, few-layer TMDs are good candidates for nanodevices due to the degree of freedom offered by additional layers.

Fabricating few-layer MoS_2 with specific stacking order can be achieved by two main routes: (i) sequential mechanically stacking of MoS_2 monolayers with a precise control over twist angles, (ii) growth of few-layer MoS_2 followed by a selection of quantified stacking sequences. Direct growth of few-layer MoS_2 crystals has the advantage of scalable production and no interlayer contamination and in particular, chemical vapor deposition (CVD) growth of MoS_2 has been achieved with wafer scale coverage. CVD growth of monolayer MoS_2 is often carried out using amorphous substrates such as SiO_2/Si wafers, whereas the second layer of MoS_2 grows on the crystalline monolayer MoS_2 surface. In few-layer MoS_2, stacking of 1H-MoS_2 layers results in two polytypes: hexagonal 2H and rhombohedral 3R.[122-123] Naturally occurring MoS_2 crystals (molybdenite) are predominantly 2H type due to its lower formation energy. Because of the rarity of 3R-MoS_2, most of the studies have focused on 2H-MoS_2, and only a few studies have been done for 3R-MoS_2.[124-125] In the 2H polytype (**Figure 2-5**(a) and (c)), the projected pattern will depend on the number of layers: monolayers will produce a simple hexagonal pattern with a single atomic column around each of the 2D Bravais lattice point, while multilayers will produce a honeycomb pattern with two atomic columns around each of the 2D Bravais lattice point. The lattice spacing is 3.16 and 3.15 Å for MoS_2 and WS_2, respectively. In the 3R polytype (**Figure 2-5**(b) and (d)), the Mo^{4+}/W^{4+} ions in the monolayer and bilayer regions will form hexagonal and honeycomb patterns, respectively, similarly to the 2H polytype. However, the trilayers will form hexagonal patterns with much smaller lattice spacing (1.83 Å for MoS_2 and 1.82 Å for WS_2). It must be also noted that, while the patterns formed in the bilayer regions are similar for both 2H and 3R polytypes, the actual structures are fundamentally different. **Figure 2-5**(e) and (f) show HR-TEM images of MoS_2 trilayers

in 2H and 3R stacking orders. The images can be correlated with the crystal structures in **Figure 2-5**(c) and (d), respectively.

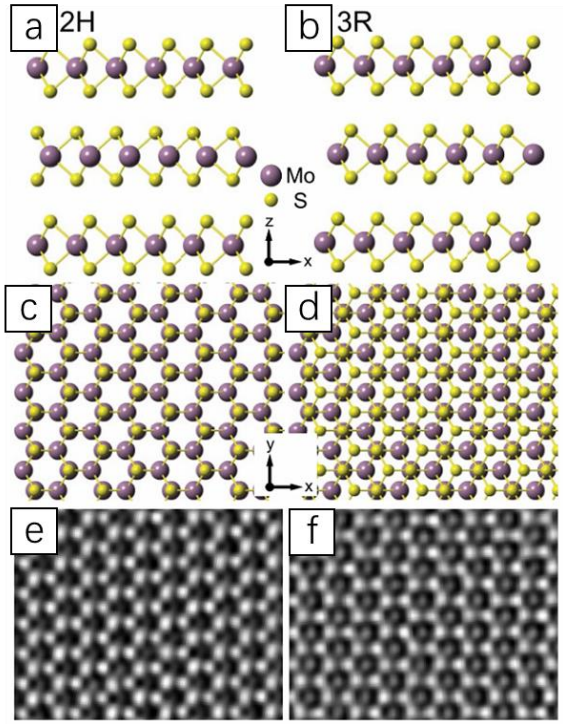

Figure 2-5 Crystal structures of 2H- and 3R-MoS_2. Side view of (a) 2H- and (b) 3R-MoS_2. Top view of (c) 2H- and (d) 3R-MoS_2. HRTEM images of 3TL MoS_2 with (e) 2H and (f) 3R stacking orders. Reprinted with permission from ref. 122 © Copyright 2016, American Chemical Society.

Since stacking sequence is one of the key attributes to layered materials, the effects of different stacking sequences on the electronic and other properties of two-dimensional (2D) materials are of great interest. Although the crystal structure of each layer is identical, the properties of few-layer crystals are sensitively dependent on the stacking sequence due to different interlayer interactions.[126] Different stacking sequences modify the crystal symmetry, which varies the Coulomb interaction between layers resulting in different equilibrium interlayer distances.[127-128] Therefore, many physical properties of 2D layered materials including bandgap size, phonon vibration frequency, magnetism and

superconductivity can be manipulated by altering the layer stacking configuration.[129-130] Interaction between MoS_2 or WS_2 layers as well as the specific stacking arrangement can significantly modify their electrical, optical and vibrational properties.[131-137] Theoretical calculations have predicted that the stacking sequence in bilayer MoS_2 plays an important role in its electronic band structure. [138] Experimental studies have found that the relative rotation angle in bilayer MoS_2 significantly modifies the direct/indirect band gap and interlayer coupling.[139-14] The recently observed spin/valley polarization in symmetry-breaking 3R-phase bulk MoS_2 (another commonly observed phase of bulk MoS_2) further elucidates the key role of stacking sequences (or crystal structure) in the properties of layered MoS_2.[141] These differently stacked MoS_2 also perform distinct properties in terms of Raman and RL.[142-143] Interlayer interaction between adjacent MoS_2 layers with different stacking order has been investigated by stacking two CVD-grown monolayer MoS_2 with a range of different twisting angles or CVD-grown bilayer MoS_2. These reports show clear stacking angle dependence of the optical properties of bilayer MoS_2. In addition, the stacking alters the band gap, which can be engineered by rotating or sliding the layers.[144-145] Therefore, the understanding and controlling of TMD bilayer stacking is significant when considering their future device applications.

2.3 Defects in TMDs

The extraordinary performances of the 2D materials only appear with extremely low defect concentration. However, according to the second law of thermodynamics, a certain degree of lattice disorder must exist in crystals, and impurity atoms are always unintentionally introduced during the production process. Therefore, understanding the structure and behavior of the abnormal part in 2D materials is crucial for the manipulation of their

performances for a specific application. The precise control of the defect creation and dopant introduction will accelerate the realization of defect engineering. For TMDs, the presence of defects influences the photoluminescence spectra, electronic transport behavior and photosensing capabilities.[146-150] Understanding the structure of defects is important for developing an accurate picture of their impact on properties.

Point defects include vacancies, substitutional dopants with intrinsic or foreign elements, and adatoms (**Figure 2-6**(a)).[151-157] The agglomeration of vacancies forms vacancy lines (**Figure 2-6**(b-e)), which is one of the line defects.[158-159] Other line defects include grain boundaries (**Figure 2-6**(f-g)),[157,160-164] either between two domains with different orientations or phases or at the interface of lateral heterostructures, as well as edge termination. Other complex defects studied in TMD monolayers include ripples (**Figure 2-6**h) and inversion domains (**Figure 2-6**i).[165-168]

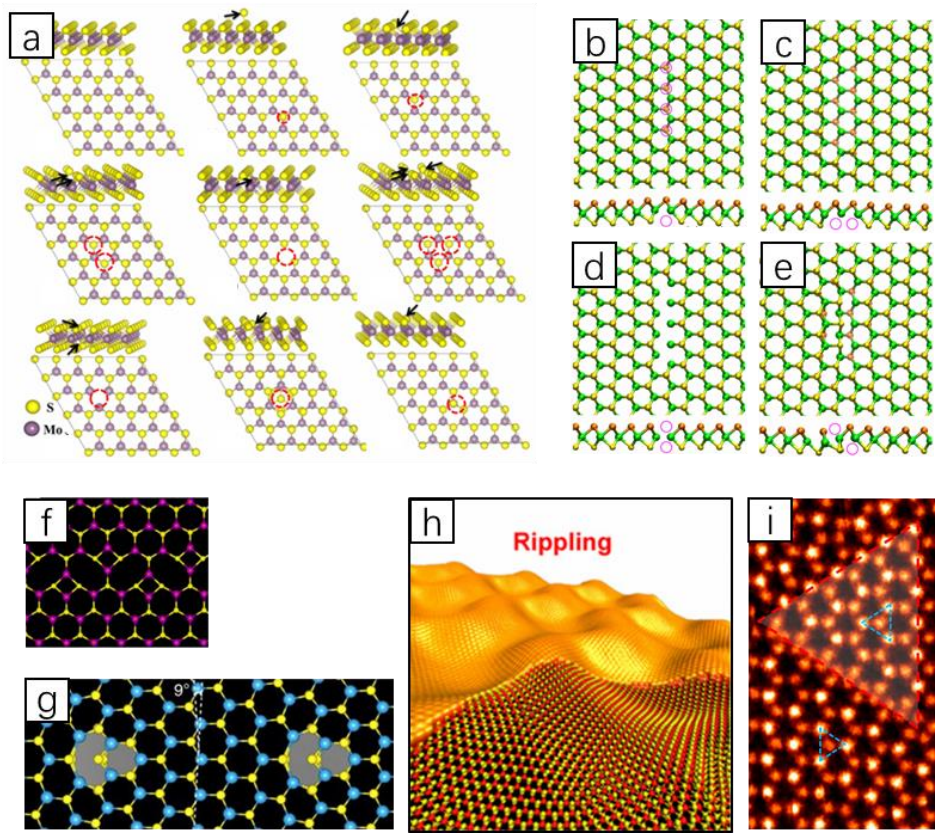

Figure 2-6 An over view of defective structures in TMDs. (a) Atomic structure of pristine 5×5 supercell of MoS_2 monolayer with S adatom on top of the top S atom, S mono-vacancy, di-S vacancies (neighboring), Mo vacancy, S tri-vacancy, di- S vacancies (top and bottom of the MoS_2 monolayer), S coordinated with 3 Mo atoms on top and S adatom on top of a Mo atom. Reprinted with permission from ref. 151 © Copyright 2014, IOP Publishing Ltd Printed in the UK. (b-e) Various models of one single vacancy line, two neighboring vacancy lines in the same S layer, two vacancy lines coinciding in top and bottom layers and two vacancy lines in staggered configuration. Reprinted with permission from ref. 158 © Copyright 2013, American Physical Society. (f-g) Relaxed structure for the dislocation cores of a 60° mirror twin grain boundary and a 9° tilt gain boundary. (f) Reprinted with permission from ref. 157 © Copyright 2013, American Chemical Society. (g) Reprinted with permission from ref. 160 © Copyright 2014, Macmillan Publishers Limited. (h) An illustration of rippling in monolayer MoS_2. Reprinted with permission from ref. 165 © Copyright 2013, Nature Publishing Group. (i) Atomic structure of monoselenium vacancy, 60° grain boundaries, and inversion domain embedded in pristine monolayer $MoSe_2$. Reprinted with permission from ref. 166 © Copyright 2015, American Chemical Society.

2.3.1 Point Defects

The most basic and commonly observed defects in TMDs are vacancies. **Figure 2-7**(a-f) display STEM-ADF images of several different point defects which are frequently observed in the CVD grown MoS_2 monolayers,[157] including single sulfur vacancy (V_S), double sulfur vacancy (V_{S2}), complex vacancy of Mo and neighboring three sulfur (V_{MoS3}), complex vacancy of Mo and neighboring three disulfur pairs (V_{MoS6}), and antisite defects such as a Mo atom substituting a 2S column (Mo_{S2}) or a 2S column substituting a Mo atom ($S2_{Mo}$). The STEM-ADF imaging, which boasts the atom-by-atom chemical analysis capability, brings clear identification of a monosulfur vacancy from disulfur vacancy, and antisite defects from regular lattice sites, by quantitatively analyzing the image intensity. The optimized defect structures from DFT calculations are shown in **Figure 2-7**(g), which are in excellent agreement with the experimental STEM images. Specifically, most of the defect structures maintain the 3-fold symmetry, while MoS_2 explicitly breaks the symmetry with Mo locating closer to two of the three nearest-neighbor Mo atoms and at one of the two S layers. It is also possible for other atomic species to replace lattice atoms by substituting elements. When considering the extent to which a foreign atom may substitute onto a crystal lattice, the ion's relative size, electronegativity, valence, and end member crystal structure are all relevant factors. The lanthanide contraction makes possible a wide variety of dopants from across the transition metal block.[169] To date, almost the entirety of the transition metal series has been examined with density functional theory (DFT) as substitutional dopants in MoS_2.[170-175] Several metallic dopants other than W have already been observed experimentally in few to monolayer MoS_2 films, including Mn, Nb, Fe, Re, Au, and Co. [176-181] Similarly, substitution of many potential dopants onto chalcogen sites

has been considered computationally.[182] While chalcogen site doping may be favorable in sulfur deficient crystals, excepting oxygen, to our knowledge no substitutive dopants have been identified experimentally.

Foreign atoms can also be adatoms adsorbed on the TMDs' surface rather than substituting onto the lattice. Ataka and Ciraci have conducted a systematic investigation based on theoretical calculation for 16 individual adatoms (C, Co, Cr, Fe, Ge, Mn, Mo, Ni, O, Pt, S, Sc, Si, Ti, V, and W) as adatoms on 2H-MoS_2.[183] Six individual minimum-energy structures of adatom-MoS_2 after relaxation have been found among these elements and the results are listed in **Figure 2-7**(h). Some atoms, such as C, Co, Fe, O, Ti, V and W, have been predicted to possess two favorable binding sites, while the rest of them only have had one. Decoration of adatoms on MoS_2 surface has been theoretically proved to have crucial influence on the electronic and magnetic properties.

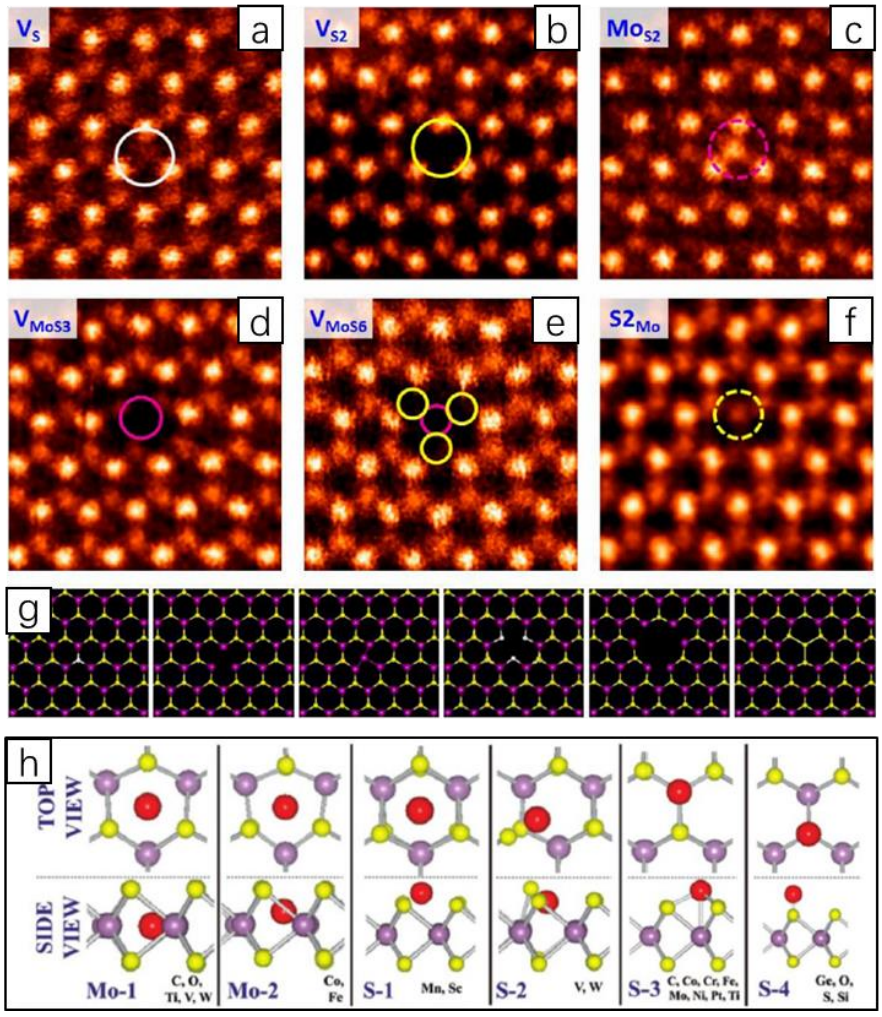

Figure 2-7 Intrinsic point defects and foreign adatoms in monolayer TMDs. (a-f) ADF images with atomic resolution of different type of intrinsic defects present in MoS_2 monolayers, including V_S, V_{S2}, Mo_{S2}, V_{MoS3}, V_{MoS6}, and $S2_{Mo}$. (g) Fully relaxed structural models of the point defects experimentally observed. From left to right: V_S, V_{S2}, Mo_{S2}, V_{MoS3}, V_{MoS6}, and $S2_{Mo}$. Purple, yellow, and white balls represent Mo, top layer S, and bottom layer S, respectively. Reprinted with permission from ref. 157 © Copyright 2013, American Chemical Society. (h) Top- and side-view illustration of adsorption structures of 16 types of adatoms in monolayer MoS_2 after relaxation. Red balls are adatoms, and Mo and S are purple and yellow. The elements that applies to the models are listed in each side-view schematic. Mo-n or S-n indicate the initial position of the adatom on the Mo or S plane. Reprinted with permission from ref. 183 © Copyright 2011, American Chemical Society.

2.3.2 Line Defects and Grain Boundaries

Prolonged electron beam irradiation causes the concentration of point defects to increase, with a tendency to initially aggregate into small clusters and then form extended line defect networks.[159] **Figure 2-8**(a) shows the detailed lattice structure corresponding to the early stage of vacancy agglomeration, where isolated point defects begin to migrate and gather into small clusters and short lines in different geometries, as indicated by white circles and lines. As the size of the vacancy cluster grows, the amount of bond reconstruction increases, as shown by the red and yellow circles in **Figure 2-8**(a). The defect clusters primarily adopt linear geometry. These line defects have a certain length along the zigzag direction determined by the number of missing S atoms but can also grow across more than one zigzag lattice line to obtain width in the armchair direction. The width of a line defect is essentially the number of adjoining parallel S vacancy lines (n) and denoted as nSVL. Some S point defects agglomerate into ultrashort 1SVL, 2SVL, and 3SVL, as shown in **Figure 2-8**(b-d), respectively, and become the nucleation of future extended line defects. **Figure 2-8**(b) displays a series of AC-TEM images showing line defects having only one line of single S vacancies (1SVL) but with lengths of 7 SVs. The formation of 1SVL alters the local stoichiometry from MoS_2 to Mo_3S_5, whereby the coordination of Mo atoms with S atoms at the defect site changes from 6-fold to 5-fold and S atoms maintain the 3-fold coordination with Mo atoms as in a pristine lattice. The DFT-calculated atomic model in **Figure 2-8**(e) shows that the generation of 1SVL triggers a slight out-of-plane distortion (side view), leading to the splitting of double-stacked S atoms adjacent to 1SVL in the top-down view. **Figure 2-8**(c) displays 2SVL that has two adjacent parallel sulfur vacancy lines. Similar to 1SVL, 2SVL also induces a slight out-of-plane distortion at the defect site

(**Figure 2-8**(f)). The lowest coordination number of Mo atoms with S atoms further decreases from 5-fold for 1SVL to 3-fold for 2SVL. The 2SVL further increases in width by S vacancies agglomerating along the armchair direction, forming 3SVL, as shown in **Figure 2-8**(d), which generally has structure similar to the 2SVL in terms of the S bond reconstruction. The DFT-calculated relaxed atomic model in **Figure 2-8**(g) shows that the energetically stable structure still has staggered arrangements of S line vacancies alternating between the top and bottom S planes. In the 2D projected view, the periodical structure at the defect site transforms from hexagonal in the pristine lattice to rectangular, highlighted by the red box in **Figure 2-8**(g).

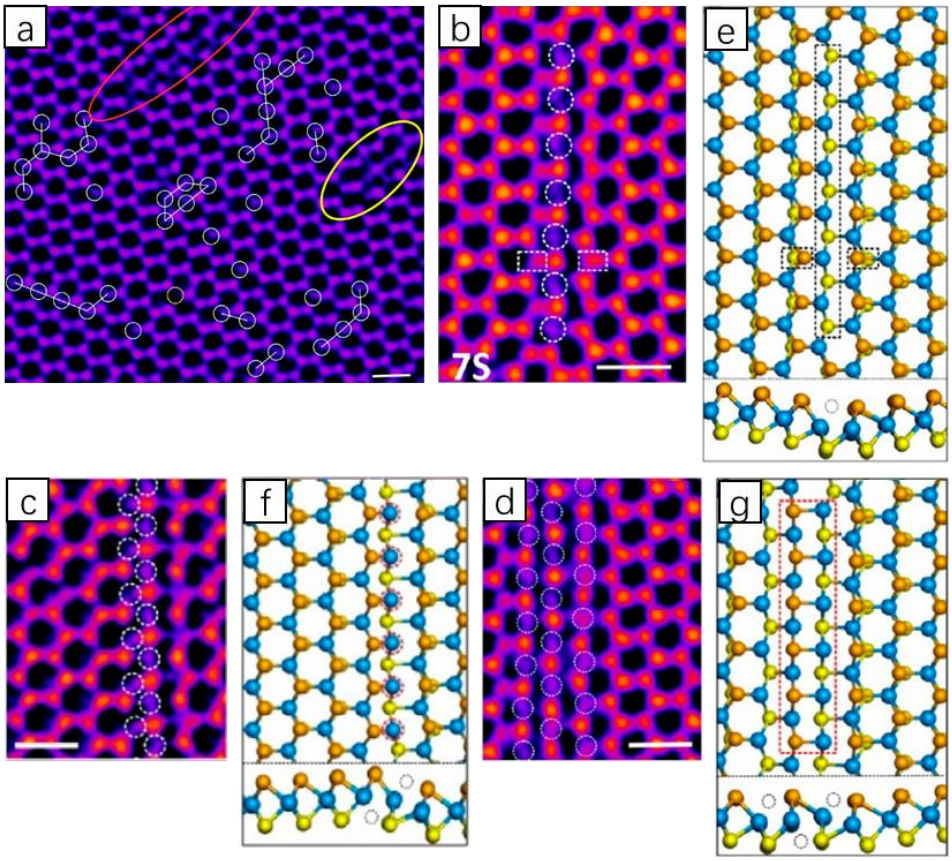

Figure 2-8 Formation mechanism and atomic structure of SVLs. (a) AC-TEM image showing detailed configurations of agglomerated S point defects into lines in different geometries, varying in length and width, which are marked by white circles and lines. The red and yellow ellipses show two line defect examples that both have two parallel S vacancy lines aggregated but in different lengths, which show a detectable variation on the lattice contraction level along the armchair direction. The scale bar corresponds to 0.5 nm. (b−d) AC-TEM images showing 1SVL, 2SVL with two adjacent single S vacancy lines and 3SVL with three single S vacancy lines highlighted by white circles. (e-g) DFT-calculated atomic model for SVLs shown in b-d. Reprinted with permission from ref. 159 © Copyright 2016, American Chemical Society.

TMDs synthesized by CVD method are polycrystalline. When two single-crystal domains with different orientations merge during the growth process, grain boundaries (GB) form (**Figure 2-9**(a) and (c)).[160] The atomic structures of GB vary with the intersecting angle of the two grains and far more complicated than the case of graphene. **Figure 2-9**(a) shows two S-zz triangles intersecting at an angle of 40°±0.5°. **Figure 2-9**(b) shows a

corresponding composite DF-TEM image of the crystal structure. The composite image is constructed by overlaying color-coded DF-TEM images acquired from the crystallographic orientations shown in the diffraction pattern of **Figure 2-9**(a). The intersection of the grains forms an abrupt, faceted tilt boundary. In addition to tilt boundaries, there is a second common line defect in MoS_2 crystals: mirror twin boundaries. In monolayer MoS_2, mirror twins are the intersections of two MoS_2 crystals with a relative in-plane rotation of 180° that effectively swaps the positions of Mo and S lattice sites. **Figure 2-9**(c) shows the bright-field image of two triangles meeting at 180°, and **Fig. 2-9**(d) shows the corresponding DF-TEM image. The mirror twin appears clearly as an intensity change in DF-TEM images, through the same diffraction asymmetry seen in **Fig. 2-9**(d).

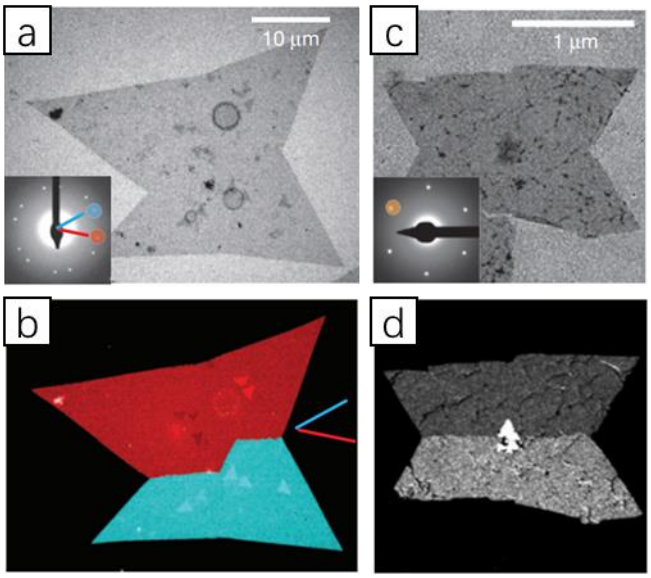

Figure 2-9 Tilt and mirror twin grain structures in MoS_2 monolayers. (a) Bright-field TEM image of two triangles that have grown together. Inset diffraction pattern shows the two crystal orientations are 40°±0.5° apart (measured between the red and cyan lines, which are at equivalent spots in the diffraction pattern). (b) Colour-coded overlay of DF-TEM images corresponding with the two red- and cyan-circled spots in a shows a tilt grain boundary as a faceted line connecting the two triangles. (c) Bright-field image of a mirror twin composed of 180°-rotated triangles, with

diffraction pattern inset. (d) Dark-field image which indicates the presence of a mirror twin boundary between the darker and lighter regions. Reprinted with permission from ref. 160 ©Copyright 2013, Macmillan Publishers Limited.

The dislocation cores of GBs include topologically conventional one with five- and 7- fold (5|7) rings, but also new core structures with 4|4, 4|6, 4|8, and 6|8 fold rings.[157] **Figure 2-10**(a) displays a 60° grain boundary in MoS_2. The GB is composed of 4-fold rings and is parallel to the zigzag direction with a point sharing at a 2S site (named as 4|4P structure). The structure of the 4|4P type GB and corresponding structure model are shown in **Figure 2-10**(b). Unlike the Mo atoms which retain the regular 6-fold coordination, the S atoms at the GB change from the 3-fold coordination to a 4-fold coordination. It is well-known that GBs are usually not perfectly straight and are linked by various GB kinks that can have important influences on the material properties.[184] As can be seen from **Figure 2-10**(c), the GB is composed of few parallel 4|4P segments which are connected by two octagonal kinks, contributing to 4|4P segments with different lengths. Another type of 60° GB consisting of strings of 4- fold rings with edge sharing (4|4E) can also form, as shown in **Figure 2-10**(d). STEM-ADF image analysis shows that the S sites along the GB are occupied by monosulfur atoms, that is, 50% S coverage, generating bonds between the S atoms from one grain and Mo atoms from the other. The 4|4E GB with 50% S coverage renders 5- and 3-fold coordination for Mo and S atoms at the GB, respectively, a decrease in coordination for Mo. As confirmed by DFT calculations, the energy of 4|4E GB with 50% S coverage is about 0.1 eV/Å lower than that with full S coverage, even under S-rich conditions. Moreover, the 4|4E GBs have the same local stoichiometry as the energy-favorable 4|4P structure, and the energy difference is only 0.04 eV/Å. Similar to the 4|4P GBs, GB kinks were also observed in the 4|4E GB. As highlighted in **Figure 2-10**(e), the 4|4E GBs are

linked by a 4-fold coordinated Mo, a further decrease in coordination for Mo.

Besides the mirror-symmetric 4|4P and 4|4E 60° GBs, Tilt grain boundaries with different tilt angle were also studied. [157] **Figure 2-10**(f) shows an 18.5° GB composed of 5|7 and 6|8 structures as schematically shown in the STEM-ADF image. The detailed atomic structures for the 5|7 and 6|8 dislocation cores are shown in **Figure 2-10**(g) and (h), respectively. The 5|7 structure can serve as the basic dislocation core structure, and the addition of monosulfur or disulfur into the Mo−Mo bonds generates the 6|8 structures observed at the same GB. The transition only happens under S-rich conditions. Therefore, the grain boundary with 6|8 structures shown in **Figure 2-10**(f) might be synthesized in a S-rich environment. However, another GB with 4|6 structures is also observed(**Figure 2-10**(i)and (j)) with 4- and 6- fold rings joined by 4-fold coordinated S atoms. The pristine 4|6 structure (**Figure 2-10**(i)) can be derived from S-oriented 5|7 structures by removing 2 S atoms, which is energetically favorable under Mo-rich conditions. The dislocation core density caused by the local growth environment imply possibilities of precise GB structures control. Through tuning the local chemical growth ingredient, the local properties of GB structures can be altered.

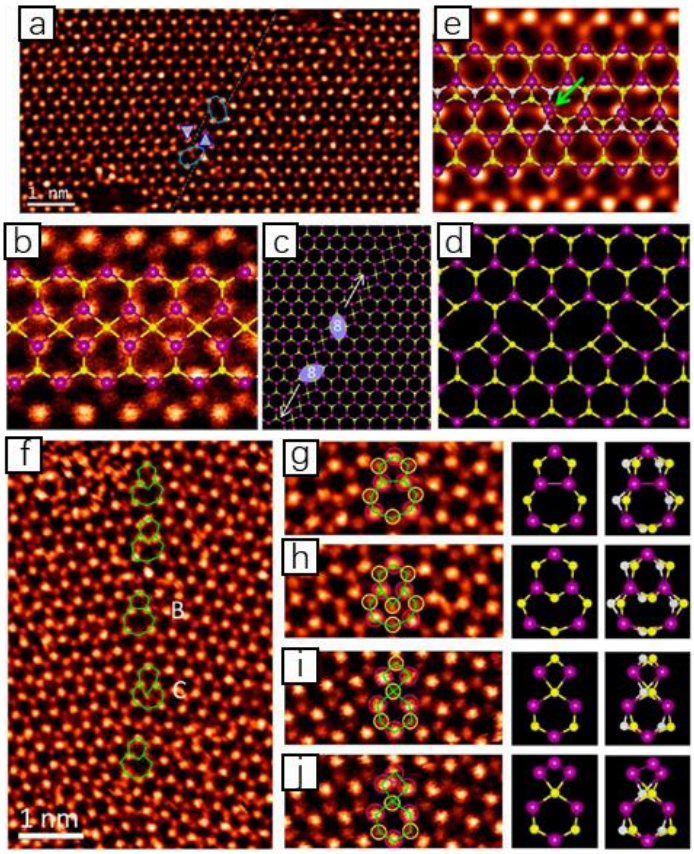

Figure 2-10 Atomic structure of mirror twin and tilt grain boundaries in monolayer MoS_2. (a) ADF image of a 4|4P 60° grain boundary. The green dash line highlights the position of the 4|4P grain boundary, and the grain boundary steps are linked by octagons as indicated. The blue triangles illustrate the orientation of the two grains with 60° rotation. (b) ADF image of the 4|4P 60° GB structures with the structural model overlaid. (c) Schematic structure of the GB and GB kinks as shown in a. (d) Relaxed structure for 4|8 GB, representing a 4|4P GB with the highest kink density. (e) ADF image and overlaid structural model of a 4|4E type 60° grain boundary, and the grain boundary steps are linked by 4-fold coordinated Mo atoms as highlighted. (f-h) STEM-ADF images of an 18.5° grain boundary consisting of dislocations with five- and seven-fold rings (5|7) and dislocations with six- and eight-fold rings (6|8). g and h are the zoom-in view of the 5|7 and 6|8 structures from the regions indicated in f. (i, j) ADF images of a 17.5° grain boundary consisting of dislocations with four- and six-fold rings (4|6), either pristine (i) or with Mo-substitution (j). The 2D and 3D structural models for the various dislocation structures are placed next to the corresponding ADF images. Reprinted with permission from ref. 157 ©Copyright 2013, American Chemical Society.

2.3.3 Ripples

Ripples are intensively studied in monolayer or few-layer graphene.[185-192] Thermal vibrations, edge instabilities, thermodynamically unstable (interatomic) interactions, strain in 2D crystals, thermal contraction, dislocations, solvent trapping, pre-strained substrate-relaxation, surface anchorage and high solvent surface tension during transfer cause wrinkles or ripples to form on graphene. These corrugations on graphene can modify its electronic structure, create polarized carrier puddles, induce pseudomagnetic field in bilayers and alter surface properties.[193] Similar to monolayer graphene, suspended TMD monolayers can also be stabilized by the formation of ripples. The formation of ripples results in the degradation of mobility of the carrier mass and alteration of electronic structures in these 2D materials.[167] Buckling and ripple formation has also been predicted using molecular dynamics (MD) simulations under uniaxial compression.[194] The size of the ripples generated during compression is observed to be associated with the strain rate and length of the sample.[195]

Theoretical research predicted that the ripple structures in MoS_2 will generate effective local strain, which can provide a suitable platform for engineering its electronic structure. A MoS_2 ripple model is shown in **Figure 2-11**(a).[165] Corresponding wavelength and height of the ripple structure are denoted as λ and h, respectively. **Figure 2-11**(b) shows a representative AFM topographical image of rippled MoS_2 nanoplates. The thickness of the nanoplate is determined to be ~0.7 nm corresponding to monolayer MoS_2. Ripple structures in MoS_2 can be clearly seen. The ripple wavelength and height are measured to be 90 nm and 3 nm, respectively, as shown in the corresponding three-dimensional (3D) image in **Figure 2-11**(d). MoS_2 ripples with larger wavelength and height are also detected

in **Figures 2-11**(c) and (e) with the values of ~10 nm and ~150 nm, respectively. The ripple wavelengths range from 40 nm to 300 nm and the ripple heights vary from 1 nm to 25 nm. As one of 2D atomic crystals with outstanding mechanical strength, MoS_2 can be largely bent or folded, which is useful for the applications of flexible electronics. We can therefore expect that local uniaxial strain in the rippled MoS_2 nanostructures could provide a new route to engineer the physical properties in MoS_2 ripples. However, ripples in TMD layers are rarely observed or studied experimentally. Detailed atomic structure of this surface ripple between perfect stacking orders has not been investigated. It is not known about the relationship between the morphology of the ripples in the bilayers and the corresponding lattice registration. One more unsolved issue is how these ripples behave under high temperature and prolonged beam irradiation.

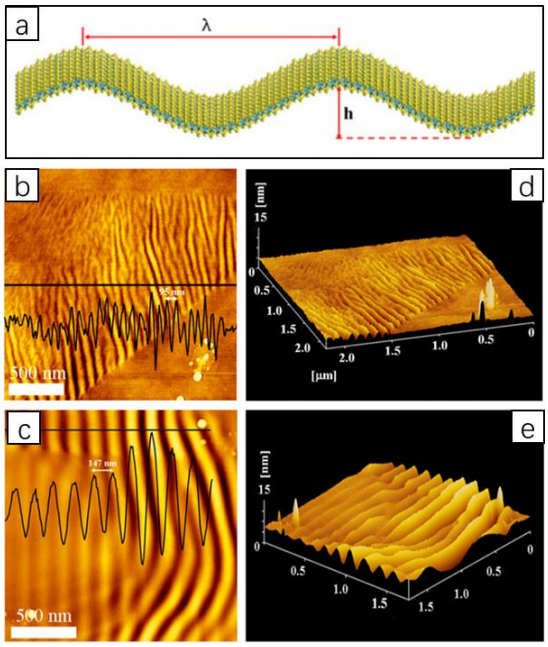

Figure 2-11 Ripples in MoS_2 monolayer. (a) A schematic model of MoS_2 ripple structure. (b-c) AFM images of MoS_2 ripple structures with different wavelengths and wave heights. (d-e) Corresponding 3D image. Reprinted with permission from ref. 165 ©Copyright 2013, IOP Publishing Ltd.

2.4 Conclusion

Studies have been done and added building blocks in the field of 2D materials. Top-down and bottom-up fabrication methods have been invented and improved to achieve layered materials with high quality and large scale. New members have been continuously introduced to the 2D materials family and more are expected to be fabricated and investigated in lab, and finally, in industry.

TMDs are stacked through weak interlayer van der Waals interactions. Compared to their more intensively studies monolayer forms, their bilayer structures offer an extra layer degree of freedom, which introduces performance enhancements. The stacking sequence is one of the key attributes of layered materials. Although the crystal structure of each layer

is identical, the properties of few-layer crystals are sensitively dependent on the stacking sequence due to different interlayer interactions. Therefore, the understanding and controlling of TMD bilayer stacking is significant when considering their future device applications. Defect engineering has long been applied in the TMD monolayer system. The defective structures of layered materials not only provide a fertile ground for the exploration of fundamental science, but also broaden the potential applications of 2D materials in various fields. With the development of modern imaging technologies, including AC-TEM and STEM, direct observation of the configurations and dynamics of the defects have been realized. Intensive studies on the structures and behaviors of these defects in the bilayer system is necessary for altering the stacking sequences and realizing the few-layer TMD based device application.

2.5 References

(1) Novoselov, K.S.; Geim, A.K., Morozov, S.V., Jiang, D., Zhang, Y., Dubonos, S.V., Grigorieva, I.V. and Firsov, A.A. Electric Field Effect in Atomically Thin Carbon Films. *Science*. **2004**, 306, 666-669.

(2) Novoselov, K.S.; Jiang, D.; Schedin, F.; Booth, T.J.; Khotkevich, V.V.; Morozov, S.V. and Geim, A.K. Two-dimensional Atomic Crystals. *Proceedings of the National Academy of Sciences*. **2005**, 102, 10451-10453.

(3) Song, L.; Ci, L.; Lu, H.; Sorokin, P.B.; Jin, C.; Ni, J.; Kvashnin, A.G.; Kvashnin, D.G.; Lou, J.; Yakobson, B.I. and Ajayan, P.M. Large Scale Growth and Characterization of Atomic Hexagonal Boron Nitride Layers. *Nano letters*. **2010**, 10, 3209-3215.

(4) Shi, Y.; Hamsen, C.; Jia, X.; Kim, K.K.; Reina, A.; Hofmann, M.; Hsu, A.L.; Zhang, K.; Li, H.; Juang, Z.Y. and Dresselhaus, M.S., Synthesis of Few-layer Hexagonal Boron Nitride Thin Film by Chemical Vapor Deposition. *Nano letters*. **2010**, 10, 4134-4139.

(5) Lee, K.H.; Shin, H.J.; Lee, J.; Lee, I.Y.; Kim, G.H.; Choi, J.Y. and Kim, S.W. Large-scale Synthesis of High-quality Hexagonal Boron Nitride Nanosheets for Large-area Graphene Electronics. *Nano letters*. **2012**, 714-718.

(6) Zhang, Y.; Tan, Y.W.; Stormer, H.L. and Kim, P. Experimental Observation of the Quantum Hall Effect and Berry's Phase in Graphene. *Nature*. **2012**, 438, 201.

(7) Decker, R.; Wang, Y.; Brar, V.W.; Regan, W.; Tsai, H.Z.; Wu, Q.; Gannett, W.; Zettl, A. and Crommie, M.F. Local Electronic Properties of Graphene on a BN Substrate via Scanning Tunneling Microscopy. *Nano letters*. **2011**, 11, 2291-2295.

(8) Zeng, H.; Zhi, C.; Zhang, Z.; Wei, X.; Wang, X.; Guo, W.; Bando, Y. and Golberg, D. "White Graphenes": Boron Nitride Nanoribbons via Boron Nitride Nanotube Unwrapping. *Nano letters.* **2010**, 10, 5049-5055.

(9) Radisavljevic, B.; Radenovic, A.; Brivio, J.; Giacometti, V. and Kis, A. Single-layer MoS_2 Transistors. *Nature nanotechnology*. **2011**, 147.

(10) Wang, Q.H.; Kalantar-Zadeh, K.; Kis, A.; Coleman, J.N. and Strano, M.S. Electronics and Optoelectronics of Two-dimensional Transition Metal Dichalcogenides. *Nature nanotechnology.* **2012,** 699.

(11) Balendhran, S.; Walia, S.; Nili, H.; Ou, J.Z.; Zhuiykov, S.; Kaner, R.B.; Sriram, S.; Bhaskaran, M. and Kalantar‐zadeh, K. Two-dimensional Molybdenum Trioxide and Dichalcogenides. *Advanced Functional Materials*. **2013**, 23, 3952-3970.

(12) Geim, A.K. and Novoselov, K.S. The Rise of Graphene. *In Nanoscience and Technology: A Collection of Reviews from Nature Journals*, **2010,** 11-19.

(13) Liu, H.; Liu, Y. and Zhu, D. Chemical Doping of Graphene. *Journal of Materials Chemistry*. **2011**, 21, 3335-3345.

(14) Zanella, I.; Guerini, S.; Fagan, S.B.; Mendes Filho, J. and Souza Filho, A.G. Chemical Doping-induced Gap Opening and Spin Polarization in Graphene. *Physical Review B*. **2008**, 77, 073404.

(15) Bai, J.; Zhong, X.; Jiang, S.; Huang, Y. and Duan, X. Graphene Nanomesh. *Nature nanotechnology*. **2010**, 5, 190.

(16) Kim, M.; Safron, N.S.; Han, E.; Arnold, M.S. and Gopalan, P. Fabrication and Characterization of Large-area, Semiconducting Nanoperforated Graphene Materials. *Nano letters*. **2010**, 10, 1125-1131

(17) Liu, X.; Zhang, Z. and Guo, W. Universal Rule on Chirality‐Dependent Bandgaps in Graphene Antidot Lattices. *Small*. **2013**, 9, 1405-1410.

(18) Pedersen, T.G.; Flindt, C.; Pedersen, J.; Mortensen, N.A.; Jauho, A.P. and Pedersen, K. Graphene Antidot Lattices: Designed Defects and Spin Qubits. *Physical Review Letters*. **2008**, 100, 136804.

(19) Han, M.Y.; Özyilmaz, B.; Zhang, Y. and Kim, P. Energy Band-gap Engineering of Graphene Nanoribbons. *Physical Review Letters*. **2007**, 98, 206805.

(20) Son, Y.W.; Cohen, M.L. and Louie, S.G. Energy Gaps in Graphene *Nanoribbons. Physical Review Letters.* **2006**, 97, 216803.

(21) Kubota, Y.; Watanabe, K.; Tsuda, O. and Taniguchi, T. Deep Ultraviolet Light-Emitting Hexagonal Boron Nitride Synthesized at Atmospheric Pressure. *Science*. **2007**, 317, 932-934.

(22) Dean, C.R.; Young, A.F.; Meric, I.; Lee, C.; Wang, L.; Sorgenfrei, S. and Watanabe, K. Boron Nitride Substrates for High-Quality Graphene Electronics. *Nat. Nanotechnol*. **2010**, 5, 722-726.

(23) Radisavljevic, B.; Radenovic, A.; Brivio, J.; Giacometti, V. and Kis, A. Single-layer MoS_2 Transistors. *Nature Nanotechnology*. **2010**, 6, 147.

(24) Lopez-Sanchez, O.; Lembke, D.; Kayci, M.; Radenovic, A. and Kis, A. Ultrasensitive Photodetectors Based on Monolayer MoS_2. *Nature nanotechnology*. **2013**, 8, 497.

(25) Bertolazzi, S.; Krasnozhon, D. and Kis, A. Nonvolatile Memory Cells Based on MoS_2/Graphene Heterostructures. *ACS nano*. **2013**, 7, 3246-3252.

(26) Chhowalla, M.; Shin, H.S.; Eda, G.; Li, L.J.; Loh, K.P. and Zhang, H. The Chemistry of Two-dimensional Layered Transition Metal Dichalcogenide Nanosheets. *Nature chemistry*. **2013**, 5, 263.

(27) Han, S.A.; Bhatia, R. and Kim, S.W. Synthesis, Properties and Potential Applications of Two-dimensional Transition Metal Dichalcogenides. *Nano Convergence*. **2015**, 2, 17.

(28) Huang, X.; Yin, Z.; Wu, S.; Qi, X.; He, Q.; Zhang, Q.; Yan, Q.; Boey, F. and Zhang, H. Graphene-based Materials: Synthesis, Characterization, Properties, and Applications. *Small.* **2011,** 7, 1876-1902.

(29) Yoon, Y.; Ganapathi, K. and Salahuddin, S. How Good Can Monolayer MoS_2 Transistors Be? *Nano letters*. **2007**, 11, 3768-3773.

(30) Zhang, Y.; Ye, J.; Matsuhashi, Y. and Iwasa, Y. Ambipolar MoS_2 Thin Flake Transistors. *Nano letters*, **2012**, 12, 1136-1140.

(31) Kim, S.; Konar, A.; Hwang, W.S.; Lee, J.H.; Lee, J.; Yang, J.; Jung, C.; Kim, H.; Yoo, J.B.; Choi, J.Y. and Jin, Y.W. High-mobility and Low-power Thin-film Transistors Vased on Multilayer MoS_2 Crystals. *Nature Communications*. **2011**, 3,

1011.

(32) Wang, H.; Yu, L.; Lee, Y.H.; Shi, Y.; Hsu, A.; Chin, M.L.; Li, L.J.; Dubey, M.; Kong, J. and Palacios, T. Integrated Circuits Based on Bilayer MoS_2 Transistors. *Nano letters*. **2016**, 12, 4674-4680.

(33) Lee, H.S.; Min, S.W.; Chang, Y.G.; Park, M.K.; Nam, T.; Kim, H.; Kim, J.H.; Ryu, S. and Im, S. MoS_2 Nanosheet Phototransistors with Thickness-modulated Optical Energy Gap. *Nano Letters.* **2012**, 12, 3695-3700.

(34) Frey, G.L.; Reynolds, K.J.; Friend, R.H.; Cohen, H. and Feldman, Y. Solution-processed Anodes from Layer-structure Materials for High-efficiency Polymer Light-emitting Diodes. *Journal of the American Chemical Society*. **2003**, 125, 5998-6007.

(35) Zeng, Z.; Yin, Z.; Huang, X.; Li, H.; He, Q.; Lu, G.; Boey, F. and Zhang, H. Single‐Layer Semiconducting Nanosheets: High‐yield preparation and device fabrication. *Angewandte Chemie International Edition*. **2011**, 50, 11093-11097.

(36) He, Q.; Wu, S.; Yin, Z. and Zhang, H. Graphene-based Electronic Sensors. *Chemical Science*. **2011**, 3, 1764-1772.

(37) Wu, S.; Zeng, Z.; He, Q.; Wang, Z.; Wang, S.J.; Du, Y.; Yin, Z.; Sun, X.; Chen, W. and Zhang, H. Electrochemically Reduced Single-layer MoS_2 Nanosheets: Characterization, Properties, and Sensing Applications. *Small.* **2012**, 8, 2264-2270.

(38) Whittingham, M.S. Lithium Batteries and Cathode Materials. *Chemical Reviews.* **2004**, 104, 4271-4302.

(39) Palacin, M.R. Recent Advances in Rechargeable Battery Materials: A Chemist's Perspective. *Chemical Society Reviews*. **2009**, 38, 2565-2575.

(40) Xiao, J.; Choi, D.; Cosimbescu, L.; Koech, P.; Liu, J. and Lemmon, J.P. Exfoliated MoS_2 Nanocomposite as An Anode Material for Lithium Ion Batteries. *Chemistry of Materials*. **2010**, 22, 4522-4524.

(41) Soon, J.M. and Loh, K.P. Electrochemical Double-layer Capacitance of MoS_2 Nanowall Films. *Electrochemical and Solid-State Letters*. **2007,** 10, 250-254.

(42) Mak, K.F.; Lee, C.; Hone, J.; Shan, J. and Heinz, T.F. Atomically Thin MoS_2: A New Direct-gap Semiconductor. *Physical review letters.* **2010,** 105, 136805.

(43) Radisavljevic, B.; Radenovic, A. and Brivio, J. Giacometti and A. Kis. *Nat. Nanotechnol*. **2011**, 6, 147-150.

(44) Yin, Z.; Li, H.; Li, H.; Jiang, L.; Shi, Y.; Sun, Y.; Lu, G.; Zhang, Q.; Chen, X. and

Zhang, H. Single-layer MoS_2 Phototransistors. *ACS nano.* **2011**, 6, 74-80.

(45) Zeng, Z.; Yin, Z.; Huang, X.; Li, H.; He, Q.; Lu, G.; Boey, F. and Zhang, H. Single‐Layer Semiconducting Nanosheets: High‐yield Preparation and Device Fabrication. *Angewandte Chemie International Edition*. **2011**, 50, 11093-11097.

(46) Wang, Q.H.; Kalantar-Zadeh, K.; Kis, A.; Coleman, J.N. and Strano, M.S. Electronics and Optoelectronics of Two-dimensional Transition Metal Dichalcogenides. *Nature nanotechnology*. **2012,** 7, 699.

(47) Mak, K.F.; He, K.; Shan, J. and Heinz, T.F. Control of Valley Polarization in Monolayer MoS_2 by Optical Helicity. *Nature nanotechnology.* **2012,** 7, 494.

(48) Li, G.; Zhang, D.; Qiao, Q.; Yu, Y.; Peterson, D.; Zafar, A.; Kumar, R.; Curtarolo, S.; Hunte, F.; Shannon, S. and Zhu, Y. All the Catalytic Active Sites of MoS_2 for Hydrogen Evolution. *Journal of the American Chemical Society*. **2016,** 138, 16632-16638.

(49) Ye, G.; Gong, Y.; Lin, J.; Li, B.; He, Y.; Pantelides, S.T.; Zhou, W.; Vajtai, R. and Ajayan, P.M. Defects Engineered Monolayer MoS_2 for Improved Hydrogen Evolution Reaction. *Nano Letters.* **2016**, 16, 1097-1103.

(50) Li, H.; Tsai, C.; Koh, A.L.; Cai, L.; Contryman, A.W.; Fragapane, A.H.; Zhao, J.; Han, H.S.; Manoharan, H.C.; Abild-Pedersen, F. and Nørskov, J.K. Activating and Optimizing MoS_2 Basal Planes for Hydrogen Evolution through the Formation of Strained Sulfur Vacancies. *Nature materials*. **2016**, 15, 48.

(51) Yin, Y.; Han, J.; Zhang, Y.; Zhang, X.; Xu, P.; Yuan, Q.; Samad, L.; Wang, X.; Wang, Y.; Zhang, Z. and Zhang, P. Contributions of Phase, Sulfur Vacancies, and Edges to the Hydrogen Evolution Reaction Catalytic Activity of Porous Molybdenum Disulfide Nanosheets. *Journal of the American Chemical Society.* **2016,** 138, 7965-7972.

(52) Novoselov, K.S.; Jiang, D.; Schedin, F.; Booth, T.J.; Khotkevich, V.V.; Morozov, S.V. and Geim, A.K. Two-dimensional Atomic Crystals. *Proceedings of the National Academy of Sciences*. **2005,** 102, 10451-10453.

(53) Late, D.J. Temperature Dependent Phonon Shifts in Single-layer WS_2. *ACS Applied Materials & Interfaces*. **2014**, 6, 1158-1163.

(54) Pacile, D.; Meyer, J.C.; Girit, Ç.Ö. and Zettl, A. The Two-dimensional Phase of Boron Nitride: Few-atomic-layer Sheets and Suspended Membranes. *Applied Physics Letters.* **2008**, 92, 133107.

(55) Coleman, J.N.; Lotya, M.; O'Neill, A.; Bergin, S.D.; King, P.J.; Khan, U.;Young, K.; Gaucher, A.; De, S.; Smith, R.J. and Shvets, I.V. Two-dimensional Nanosheets

Produced by Liquid Exfoliation of Layered Materials. *Science*. **2011**, 331, 568-571.

(56) Joensen, P.; Frindt, R.F. and Morrison, S.R. Single-layer MoS_2. *Materials Research Bulletin*. **1986**, 21, 457-461.

(57) Dines, M.B. Lithium Intercalation via N-butyllithium of The Layered Transition Metal Dichalcogenides. *Materials Research Bulletin.* **1979**, 10, 287-291.

(58) Benavente, E.; Santa Ana, M.A.; Mendizábal, F. and González, G. Intercalation Chemistry of Molybdenum Disulfide. *Coordination Chemistry Reviews*. **2002,** 224, 87-109.

(59) Ramakrishna Matte, H.S.S.; Gomathi, A.; Manna, A.K.; Late, D.J.; Datta, R.; Pati, S.K. and Rao, C.N.R. MoS_2 and WS_2 Analogues of Graphene. *Angewandte Chemie International Edition.* **2010,** 49, 4059-4062.

(60) Kim, K.K.; Hsu, A.; Jia, X.; Kim, S.M.; Shi, Y.; Hofmann, M.; Nezich, D., Rodriguez-Nieva, J.F.; Dresselhaus, M.;Palacios, T. and Kong, J. Synthesis of Monolayer Hexagonal Boron Nitride on Cu foil Using Chemical Vapor Deposition. *Nano letters*. **2011**, 12, 161-166.

(61) Ling, X.; Lee, Y.H.; Lin, Y.; Fang, W.; Yu, L.; Dresselhaus, M.S. and Kong, J. Role of The Seeding Promoter in MoS_2 Growth by Chemical Vapor Deposition. *Nano letters.* **2013**, 14, 464-472.

(62) Lee, Y.H.; Zhang, X.Q.; Zhang, W.; Chang, M.T.; Lin, C.T.; Chang, K.D.; Yu, Y.C.; Wang, J.T.W.; Chang, C.S.; Li, L.J. and Lin, T.W. Synthesis of Large-area MoS_2 Atomic Layers with Chemical Vapor Deposition. *Advanced Materials.* **2012,** 24, 2320-2325.

(63) Nayak, P.K.; Lin, F.C.; Yeh, C.H.; Huang, J.S. and Chiu, P.W. Robust Room Temperature Valley Polarization in Monolayer and Bilayer WS_2. *Nanoscale.* **2016,** 8, 6035-6042.

(64) Shaw, J.C.; Zhou, H.; Chen, Y.; Weiss, N.O.; Liu, Y.; Huang, Y. and Duan, X. Chemical Vapor Deposition Growth of Monolayer $MoSe_2$ Nanosheets. *Nano Research.* **2014**, 7, 511-517.

(65) Wang, S.; Pacios, M.; Bhaskaran, H. and Warner, J.H. Substrate Control for Large Area Continuous Films of Monolayer MoS_2 by Atmospheric Pressure Chemical Vapor Deposition. *Nanotechnology*. **2016,** 27, 085604.

(66) Sheng, Y.; Tan, H.; Wang, X. and Warner, J.H. Hydrogen Addition for Centimeter-Sized Monolayer Tungsten Disulfide Continuous Films by Ambient Pressure

Chemical Vapor Deposition. *Chemistry of Materials*. **2017**, 29, 4904-4911.

(67) Rong, Y.; Fan, Y.; Koh, A.L.; Robertson, A.W.; He, K.; Wang, S.; Tan, H.; Sinclair, R. and Warner, J.H. Controlling Sulfur Precursor Addition for Large Single Crystal Domains of WS_2. *Nanoscale*. **2014,** 6, 12096-12103.

(68) Brito, J.L.; Ilija, M. and Hernández, P. Thermal and Reductive Decomposition of Ammonium Thiomolybdates. *Thermochimica Acta.* **1995**, 256, 325-338.

(69) Kong, Y.C. Synthesis of MoS_2 and $MoSe_2$ Films with Vertically Aligned Layers. *Nano letters*. **2013**, 3, 1341-1347.

(70) Han, G.H.; Kybert, N.J.; Naylor, C.H.; Lee, B.S.; Ping, J.; Park, J.H.; Kang, J.; Lee, S.Y.; Lee, Y.H.; Agarwal, R. and Johnson, A.C. Seeded Growth of Highly Crystalline Molybdenum Disulphide Monolayers at Controlled Locations. *Nature Communications*. **2015**, 6, 6128.

(71) Song, J.G.; Park, J.; Lee, W.; Choi, T.; Jung, H.; Lee, C.W.; Hwang, S.H.; Myoung, J.M.; Jung, J.H.; Kim, S.H. and Lansalot-Matras, C. Layer-controlled, Wafer-scale, and Conformal Synthesis of Tungsten Disulfide Nanosheets using Atomic Layer Deposition. *ACS nano*. **2013,** 7, 11333-11340.

(72) You, J.; Hossain, M.D. and Luo, Z. Synthesis of 2D Transition Metal Dichalcogenides by Chemical Vapor Deposition with Controlled Layer Number and Morphology. *Nano Convergence*. **2018**, 5, 26.

(73) Wu, S.; Huang, C.; Aivazian, G.; Ross, J.S.; Cobden, D.H. and Xu, X. Vapor-solid Growth of High Optical Quality MoS_2 Monolayers with Near-unity Valley Polarization. *ACS Nano*. **2013**, 7, 2768-2772.

(74) Ji, Q.; Zhang, Y.; Zhang, Y. and Liu, Z. Chemical Vapour Deposition of Group-VIB Metal Dichalcogenide Monolayers: Engineered Substrates from Amorphous to Single Crystalline. *Chemical Society Reviews*. **2016**, 44, 2587-2602.

(75) Eda, G.; Fujita, T.; Yamaguchi, H.; Voiry, D.; Chen, M. and Chhowalla, M. Coherent Atomic and Electronic Heterostructures of Single-layer MoS_2. *ACS Nano.* **2012,** 6, 7311-7317.

(76) Tan, Y.; Luo, F.; Zhu, M.; Xu, X.; Ye, Y.; Li, B.; Wang, G.; Luo, W.; Zheng, X.; Wu, N. and Yu, Y. Controllable 2H-to-1T' Phase Transition in Few-layer $MoTe_2$. *Nanoscale*. **2018,** 10, 19964-19971.

(77) Ataca, C.; Sahin, H.; Akturk, E. and Ciraci, S. Mechanical and Electronic Properties

of MoS_2 Nanoribbons and Their Defects. *The Journal of Physical Chemistry C.* **2012,** 115, 3934-3941.

(78) Bollinger, M.V.; Jacobsen, K.W. and Nørskov, J.K. Atomic and Electronic Structure of MoS_2 Nanoparticles. *Physical Review B*. **2003**, 67, 085410.

(79) Ding, Y.; Wang, Y.; Ni, J.; Shi, L.; Shi, S. and Tang, W. First Principles Study of Structural, Vibrational and Electronic Properties of Graphene-like MX_2 (M= Mo, Nb, W, Ta; X= S, Se, Te) Monolayers. *Physica B: Condensed Matter.* **2011**, 406, 2254-2260.

(80) Lebegue, S. and Eriksson, O. Electronic Structure of Two-dimensional Crystals from ab Initio Theory. *Physical Review B.* **2009**, 79, 115409.

(81) Kuc, A.; Zibouche, N. and Heine, T. Influence of Quantum Confinement on the Electronic Structure of The Transition Metal Sulfide TS_2. *Physical Review B.* **2011,** 83, 245213.

(82) Wang, Q.H.; Kalantar-Zadeh, K.; Kis, A.; Coleman, J.N. and Strano, M.S. Electronics and Optoelectronics of Two-dimensional Transition Metal Dichalcogenides. *Nature nanotechnology.* **2012**, 7, 699.

(83) Ma, Y.; Dai, Y.; Guo, M.; Niu, C.; Lu, J. and Huang, B. Electronic and Magnetic Properties of Perfect, Vacancy-doped, and Nonmetal adsorbed $MoSe_2$, $MoTe_2$ and WS_2 monolayers. *Physical Chemistry Chemical Physics*. **2011**, 13, 15546-15553.

(84) Wypych, F. and Schöllhorn, R. 1T-MoS_2, A New Metallic Modification of Molybdenum Disulfide. *Journal of the Chemical Society*. **1992**, 19, 1386-1388.

(85) Splendiani, A.; Sun, L.; Zhang, Y.; Li, T.; Kim, J.; Chim, C.Y.; Galli, G. and Wang, F. Emerging Photoluminescence in Monolayer MoS_2. *Nano Letters*. **2011**, 10, 1271-1275.

(86) Mak, K.F.; Lee, C.; Hone, J.; Shan, J. and Heinz, T.F. Atomically Thin MoS_2: A New Direct-gap Semiconductor. *Physical Review Letters.* **2011**, 105, 136805.

(87) Gutiérrez, H.R.; Perea-López, N.; Elías, A.L.; Berkdemir, A.; Wang, B.; Lv, R.; López-Urías, F.; Crespi, V.H.; Terrones, H. and Terrones, M. Extraordinary Room-temperature Photoluminescence in Triangular WS_2 Monolayers. *Nano Letters*. **2012,** 13, 3447-3454.

(88) Wang, Q.H.; Kalantar-Zadeh, K.; Kis, A.; Coleman, J.N. and Strano, M.S. Electronics and Optoelectronics of Two-dimensional Transition Metal

Dichalcogenides. Nature nanotechnology. 2012, 7, 699.

(89) Zhao, W.; Ghorannevis, Z.; Chu, L.; Toh, M.; Kloc, C.; Tan, P.H. and Eda, G. Evolution of Electronic Structure in Atomically Thin Sheets of WS_2 and WSe_2. *ACS nano.* **2012**, 7, 791-797.

(90) Coehoorn, R.; Haas, C.; Dijkstra, J.; Flipse, C.J.F.; De Groot, R.A. and Wold, A. Electronic Structure of $MoSe_2$, MoS_2, and WSe_2 Band-structure Calculations and Photoelectron Spectroscopy. *Physical Review B.* **1987,** 35, 6195.

(91) Evans, B.L. and Young, P.A. Optical Absorption and Dispersion in Molybdenum Disulphide. *Mathematical and Physical Sciences*. **1965**, 284, 402-422.

(92) Coehoorn, R., Haas, C. and De Groot, R.A. Electronic Structure of $MoSe_2$, MoS_2, and WSe_2. Nature of The Optical Band Gaps. *Physical Review B*. **1987**, 35, 6203.

(93) Yun, W.S.; Han, S.W.; Hong, S.C.; Kim, I.G. and Lee, J.D. Thickness and Strain Effects on Electronic Structures of Transition Metal Dichalcogenides: 2H-MX_2 Semiconductors (M= Mo, W; X= S, Se, Te). *Physical Review B*. **2012**, 85, 033305.

(94) Conley, H.J.; Wang, B.; Ziegler, J.I.; Haglund Jr, R.F.; Pantelides, S.T. and Bolotin, K.I. Bandgap Engineering of Strained Monolayer and Bilayer MoS_2. *Nano Letters.* **2013**, 13, 3626-3630.

(95) Xie, L.M. Two-dimensional Transition Metal Dichalcogenide Alloys: Preparation, Characterization and Applications. *Nanoscale*. **2015**, 7,18392-18401.

(96) Manzeli, S.; Allain, A.; Ghadimi, A. and Kis, A. Piezoresistivity and Strain-induced Band Gap Tuning in Atomically Thin MoS_2. *Nano Letters*. **2015**, 15, 5330-5335.

(97) Feng, J.; Qian, X.; Huang, C.W. and Li, J. Strain-engineered Artificial Atom as A Broad-spectrum Solar Energy Funnel. *Nature Photonics*. **2012,** 6, 866.

(98) Ganatra, R. and Zhang, Q. Few-layer MoS_2: A Promising Layered Semiconductor. *ACS nano*. **2014**, 8, 4074-4099.

(99) Li, H.; Zhang, Q.; Yap, C.C.R.; Tay, B.K.; Edwin, T.H.T.; Olivier, A. and Baillargeat, D. From Bulk to Monolayer MoS_2: Evolution of Raman Scattering. *Advanced Functional Materials.* **2012**, 22, 1385-1390.

(100) Bertolazzi, S.; Brivio, J. and Kis, A. Stretching and Breaking of Ultrathin MoS_2. *ACS nano.* **2011,** 5, 9703-9709.

(101) Castellanos‐Gomez, A.; Poot, M.; Steele, G.A.; Van Der Zant, H.S.; Agraït, N. and Rubio‐Bollinger, G. Elastic Properties of Freely Suspended MoS_2 Nanosheets. *Advanced Materials.* **2012**, 24, 772-775.

(102) Pu, J.; Yomogida, Y.; Liu, K.K.; Li, L.J.; Iwasa, Y. and Takenobu, T. Highly Flexible MoS_2 Thin-film Transistors with Ion Gel Dielectrics. *Nano Letters.* **2012**, 12, 4013-4017.

(103) Li, T. Ideal Strength and Phonon Instability in Single-layer MoS_2. *Physical Review B.* **2012**, 85, 235407.

(104) Yan, A.; Chen, W.; Ophus, C.; Ciston, J.; Lin, Y.; Persson, K. and Zettl, A. Identifying Different Stacking Sequences in Few-layer CVD-grown MoS_2 by Low-Energy Atomic-resolution Scanning Transmission Electron Microscopy. *Physical Review B.* **2016**, 93, 041420.

(105) Yuan, H.; Liu, Z.; Xu, G.; Zhou, B; Wu, S.; Dumcenco, D.; Yan, K.; Zhang, Y.; Mo, S.K.; Dudin, P. and Kandyba, V. Evolution of The Valley Position in Bulk Transition-metal Chalcogenides and Their Monolayer Limit. *Nano letters.* **2016,** 16, 4738-4745.

(106) He, J.; Hummer, K. and Franchini, C. Stacking Effects on The Electronic and Optical Properties of Bilayer Transition Metal Dichalcogenides MoS_2, $MoSe_2$, WS_2, and WSe_2. *Physical Review B.* **2014**, 89, 075409.

(107) Ataca, C.; Topsakal, M.; Akturk, E. and Ciraci, S.J.T.J. A Comparative Study of Lattice Dynamics of Three-and Two-dimensional MoS_2. *The Journal of Physical Chemistry C.* **2011,** 115, 16354-16361.

(108) López-Suárez, M.; Neri, I. and Rurali, R. Band Gap Engineering of MoS_2 upon Compression. *Journal of Applied Physics*. **2016**, 119, 165105.

(109) He, J.; Hummer, K. and Franchini, C. Stacking Effects on The Electronic and Optical Properties of Bilayer Transition Metal Dichalcogenides MoS_2, $MoSe_2$, WS_2, and WSe_2. *Physical Review B.* **2014**, 89, 075409.

(110) Splendiani, A.; Sun, L.; Zhang, Y.; Li, T.; Kim, J.; Chim, C.Y.; Galli, G. and Wang, F. Emerging Photoluminescence in Monolayer MoS_2. *Nano letters.* **2010**, 10, 1271-1275.

(111) Li, H.; Zhang, Q.; Yap, C.C.R.; Tay, B.K.; Edwin, T.H.T.; Olivier, A. and Baillargeat, D. From Bulk to Monolayer MoS_2: Evolution of Raman Scattering.

Advanced Functional Materials. **2012,** 22, 1385-1390. .

(112) Yu, Y.; Huang, S.Y.; Li, Y.; Steinmann, S.N.; Yang, W. and Cao, L. Layer-Dependent Electrocatalysis of MoS_2 for Hydrogen Evolution. *Nano letters.* **2014**, 14, 553-558.

(113) Bao, W.; Cai, X.; Kim, D.; Sridhara, K. and Fuhrer, M.S. High Mobility Ambipolar MoS_2 Field-effect Transistors: Substrate and Dielectric Effects. *Applied Physics Letters*. **2013**, 102, 042104.

(114) Lee, G.H.; Yu, Y.J.; Cui, X.; Petrone, N.; Lee, C.H.; Choi, M.S.; Lee, D.Y.; Lee, C.; Yoo, W.J.; Watanabe, K. and Taniguchi, T. Flexible and Transparent MoS_2 Field-Effect Transistors on Hexagonal Boron Nitride-graphene Heterostructures. *ACS nano*. **2013,** 7, 7931-7936.

(115) Liu, Y.J.; Hao, L.Z.; Gao, W.; Liu, Y.M.; Li, G.X.; Xue, Q.Z.; Guo, W.Y.; Yu, L.Q.; Wu, Z.P.; Liu, X.H. and Zeng, H.Z. Growth and Humidity-dependent Electrical Properties of Bulk-like MoS_2 Thin Films on Si. *RSC Advances*. **2015,** 5, 74329-74335.

(116) Yu, N.; Wang, L.; Li, M.; Sun, X.; Hou, T. and Li, Y. Molybdenum Disulfide as A Highly Efficient Adsorbent for Non-polar Gases. *Physical Chemistry Chemical Physics*. 2012, 17, 11700-11704.

(117) Ramasubramaniam, A.; Naveh, D. and Towe, E. Tunable Band Gaps in Bilayer Transition-metal Dichalcogenides. *Physical Review B.* **2011,** 84, 205325.

(118) Liu, Q.; Li, L.; Li, Y.; Gao, Z.; Chen, Z. and Lu, J. Tuning Electronic Structure of Bilayer MoS_2 by Vertical Electric Field: A First-principles Investigation. *The Journal of Physical Chemistry C*. **2012**, 116, 21556-21562.

(119) Gatensby, R.; McEvoy, N.; Lee, K.; Hallam, T.; Berner, N.C.; Rezvani, E.; Winters, S., O'Brien, M. and Duesberg, G.S. Controlled Synthesis of Transition Metal Dichalcogenide Thin Films for Electronic Applications. *Applied Surface Science.* **2014**, 297, 139-146.

(120) Late, D.J.;Huang, Y.K.; iu, B.;Acharya, J.; Shirodkar, S.N.; Luo, J.; Yan, A.; Charles, D.; Waghmare, U.V.; Dravid, V.P. and Rao, C.N.R. *ACS Nano*, **2014**, 7, 4879.

(121) Chu, T.; Ilatikhameneh, H.; Klimeck, G.; Rahman, R. and Chen, Z. Electrically Tunable Bandgaps in Bilayer MoS_2. *Nano letters*. **2015**, 15, 8000-8007.

(122) Shinde, S.M.; Dhakal, K.P.; Chen, X.; Yun, W.S.; Lee, J.; Kim, H. and Ahn, J.H.

Stacking-controllable Interlayer Coupling and Symmetric Configuration of Multilayered MoS_2. *NPG Asia Materials.* ***2018***, 10, 468.

(123) Lee, J.U. and Cheong, H. Resonance Raman Effects in Transition Metal Dichalcogenides. *Journal of Raman Spectroscopy*. **2018,** 49, 66-75.

(124) Froehlicher, G.; Lorchat, E.; Zill, O.; Romeo, M. and Berciaud, S. Rigid-layer Raman-active Modes in N-layer Transition Metal Dichalcogenides: Interlayer Force Constants and Hyperspectral Raman Imaging. *Journal of Raman Spectroscopy*. **2018**, 49, 91-99.

(125) Zhang, S.; Zhang, N.; Zhao, Y.; Cheng, T.; Li, X.; Feng, R.; Xu, H.; Liu, Z.; Zhang, J. and Tong, L. Spotting the Differences in Two-dimensional Materials–The Raman Scattering Perspective. *Chemical Society Reviews*. **2018**, 47, 217-3240.

(126) Lee, J.U.; Kim, K.; Han, S.; Ryu, G.H.; Lee, Z. and Cheong, H. Raman Signatures of Polytypism in Molybdenum Disulfide. *ACS nano*. **2016,** 10, 1948-1953.

(127) He, J.; Hummer, K. and Franchini, C. Stacking Effects on The Electronic and Optical Properties of Bilayer Transition Metal Dichalcogenides MoS_2, $MoSe_2$, WS_2, and WSe_2. *Physical Review B.* **2014,** 89, 075409.

(128) Yan, J.; Xia, J.; Wang, X.; Liu, L.; Kuo, J.L.; Tay, B.K.; Chen, S.; Zhou, W.; Liu, Z. and Shen, Z.X. Stacking-dependent Interlayer Coupling in Trilayer MoS_2 with Broken Inversion Symmetry. *Nano letters*. **2018**, 15, 8155-8161.

(129) Liu, K.; Zhang, L.; Cao, T.; Jin, C.; Qiu, D.; Zhou, Q.; Zettl, A.; Yang, P.; Louie, S.G. and Wang, F. Evolution of Interlayer Coupling in Twisted Molybdenum Disulfide Bilayers. *Nature communications*. **2014,** 5, 4966.

(130) Yacoby, A. Graphene: Tri and Tri Again. *Nature Physics*. **2011,** 7, 925.

(131) Li, H.; Wu, J.B.; Ran, F.; Lin, M.L.; Liu, X.L.; Zhao, Y.; Lu, X.; Xiong, Q.; Zhang, J.; Huang, W. and Zhang, H. Interfacial Interactions in van der Waals Heterostructures of MoS_2 and Graphene. *ACS nano*. **2017**, 11, 11714-11723.

(132) Zhou, S.; Wang, S.; Li, H.; Xu, W.; Gong, C.; Grossman, J.C. and Warner, J.H. Atomic Structure and Dynamics of Defects in 2D MoS_2 Bilayers. *ACS Omega*. **2017**, 2, 3315-3324.

(133) Singh, E.; Kim, K.S.; Yeom, G.Y. and Nalwa, H.S. Atomically Thin-layered Molybdenum Disulfide (MoS_2) for Bulk-heterojunction Solar Cells. *ACS Applied Materials & Interfaces*. **2017**, 9, 3223-3245.

(134) Kim, K.; Lee, J.U.; Nam, D. and Cheong, H. Davydov Splitting and Excitonic Resonance Effects in Raman Spectra of Few-layer $MoSe_2$. *ACS nano.* **2016**, 10, 8113-8120.

(135) Singh, R. and Tripathi, S. Structural and Optical Properties of Few-layer MoS_2 Thin Films Grown on Various Substrates using RF Sputtering Process. *Journal of Materials Science: Materials in Electronics.* **2016**, 30, 7665-7680.

(136) Van Baren, J.; Ye, G.; Yan, J.A.; Ye, Z.; Rezaie, P.; Yu, P.; Liu, Z.; He, R. and Lui, C.H. Stacking-dependent Interlayer Phonons in 3R and 2H MoS_2. *2D Materials*. **2019,** 6, 025022.

(137) Tongay, S.; Zhou, J.; Ataca, C.; Lo, K.; Matthews, T.S.; Li, J.; Grossman, J.C. and Wu, J. Thermally Driven Crossover from Indirect Toward Direct Bandgap in 2D Semiconductors: $MoSe_2$ versus MoS_2. *Nano letters.* **2012**, 12, 5576-5580.

(138) He, J.; Hummer, K. and Franchini, C. Stacking Effects on the Electronic and Optical Properties of Bilayer Transition Metal Dichalcogenides MoS_2, $MoSe_2$, WS_2, and WSe_2. *Physical Review B.* **2012,** 89, 075409.

(139) Liu, K.; Zhang, L.; Cao, T.; Jin, C.; Qiu, D.; Zhou, Q.; Zettl, A.; Yang, P.; Louie, S.G. and Wang, F. Evolution of Interlayer Coupling in Twisted Molybdenum Disulfide Bilayers. *Nature communications.* **2014**, 5, 4966.

(140) Van Der Zande, A.M.; Kunstmann, J.; Chernikov, A.; Chenet, D.A.; You, Y.; Zhang, X.; Huang, P.Y.; Berkelbach, T.C.; Wang, L.; Zhang, F. and Hybertsen, M.S. Tailoring the Electronic Structure in Bilayer Molybdenum Disulfide via Interlayer Twist. *Nano letters.* 2**014**, 14, 3869-3875.

(141) R. Suzuki. Nat. *Nanotechnol.* **2014**, 9, 611.

(142) Yan, A.; Chen, W.; Ophus, C.; Ciston, J.; Lin, Y.; Persson, K. and Zettl, A. Identifying Different Stacking Sequences in Few-layer CVD-grown MoS_2 by Low-energy Atomic-resolution Scanning Transmission Electron Microscopy. *Physical Review B.* **2016**, 93, 041420.

(143) Lee, J.U.; Kim, K.; Han, S.; Ryu, G.H.; Lee, Z. and Cheong, H. Raman Signatures of Polytypism in Molybdenum Disulfide. *ACS nano.* **2016**, 10, 1948-1953.

(144) Levita, G.; Cavaleiro, A.; Molinari, E.; Polcar, T. and Righi, M.C. Sliding Properties of MoS_2 Layers: Load and Interlayer Orientation Effects. *The Journal of Physical Chemistry C.* **2014**, 118, 13809-13816.

(145) Liu, K.; Zhang, L.; Cao, T.; Jin, C.; Qiu, D.; Zhou, Q.; Zettl, A.; Yang, P.; Louie, S.G. and Wang, F. Evolution of Interlayer Coupling in Twisted Molybdenum Disulfide Bilayers. *Nature communications.* **2014**, 5, 4966.

(146) Hashimoto, A.; Suenaga, K.; Gloter, A.; Urita, K. and Iijima, S. Direct Evidence for Atomic Defects in Graphene Layers. *Nature.* **2014**, 430, 870.

(147) Terrones, H.; Lv, R.; Terrones, M. and Dresselhaus, M.S. The Role of Defects and Doping in 2D Graphene Sheets and 1D Nanoribbons. *Reports on Progress in Physics.* **2014**, 75, 062501.

(148) Zou, X. and Yakobson, B.I. An Open Canvas 2D Materials with Defects, Disorder, and Functionality. *Accounts of chemical research*. **2014**, 48, 73-80.

(149) Banhart, F.; Kotakoski, J. and Krasheninnikov, A.V. Structural Defects in Graphene. *ACS nano*. **2010**, 5, 26-41.

(150) Neto, A.C.; Guinea, F.; Peres, N.M.; Novoselov, K.S. and Geim, A.K. The Electronic Properties of Graphene. *Reviews of modern physics*. **2019**, 81, 109.

(151) Lin, Z.; Carvalho, B.R.; Kahn, E.; Lv, R.; Rao, R.; Terrones, H.; Pimenta, M.A. and Terrones, M. Defect engineering of Two-dimensional Transition Metal Dichalcogenides. *2D Materials.* **2016,** 3, 022002.

(152) Santosh, K.C.; Longo, R.C.; Addou, R.; Wallace, R.M. and Cho, K. Impact of Intrinsic Atomic Defects on The Electronic Structure of MoS_2 Monolayers. *Nanotechnology.* **2014,** 25, 375703.

(153) Feng, L.P.; Su, J. and Liu, Z.T. Effect of Vacancies in Monolayer MoS_2 on Electronic Properties of Mo-MoS_2 Contacts. *RSC Advances*. **2015**, 5, 20538-20544.

(154) Robertson, A.W.; Lin, Y.C.; Wang, S.; Sawada, H.; Allen, C.S.; Chen, Q.; Lee, S.; Lee, G.D.; Lee, J.; Han, S. and Yoon, E. Atomic Structure and Spectroscopy of Single Metal (Cr, V) Substitutional Dopants in Monolayer MoS_2. *ACS nano*. **2016,** 10, 10227-10236.

(155) Li, H.; Wang, S.; Sawada, H.; Han, G.G.; Samuels, T.; Allen, C.S.; Kirkland, A.I.; Grossman, J.C. and Warner, J.H. Atomic Structure and Dynamics of Single Platinum Atom Interactions with Monolayer MoS_2. *ACS nano.* **2017,** 3392-3403.

(156) Hong, J.; Hu, Z.; Probert, M.; Li, K.; Lv, D.; Yang, X.; Gu, L.; Mao, N.; Feng, Q.;

Xie, L. and Zhang, J. Exploring Atomic Defects in Molybdenum Disulphide Monolayers. *Nature communications.* **2015**, 6, 6293.

(157) Zhou, W.; Zou, X.; Najmaei, S.; Liu, Z.; Shi, Y.; Kong, J.; Lou, J.; Ajayan, P.M.; Yakobson, B.I. and Idrobo, J.C. Intrinsic Structural Defects in Monolayer Molybdenum Disulfide. *Nano letters*. **2013**, 13, 2615-2622.

(158) Komsa, H.P.; Kurasch, S.; Lehtinen, O.; Kaiser, U. and Krasheninnikov, A.V. From Point to Extended Defects in Two-dimensional MoS_2: Evolution of Atomic Structure under Electron Irradiation. *Physical Review B*. **2013**, 88, 035301.

(159) Wang, S.; Lee, G.D.; Lee, S.; Yoon, E. and Warner, J.H. Detailed Atomic Reconstruction of Extended Line Defects in Monolayer MoS_2. *ACS nano*. **2016**, 10, 5419-5430.

(160) Van Der Zande, A.M., Huang, P.Y. Grains and Grain Boundaries in Highly Crystalline Monolayer Molybdenum Disulphide. *Nature materials*. **2013**, 12, 554.

(161) Najmaei, S.; Liu, Z.; Zhou, W.; Zou, X.; Shi, G.; Lei, S.; Yakobson, B.I.; Idrobo, J.C.; Ajayan, P.M. and Lou, J. Vapour Phase Growth and Grain Boundary Structure of Molybdenum Disulphide Atomic Layers. *Nature materials*. **2013**, 12, 754.

(162) Liu, X.; Balla, I.; Bergeron, H. and Hersam, M.C. Point Defects and Grain Boundaries in Rotationally Commensurate MoS_2 on Epitaxial Graphene. *The Journal of Physical Chemistry C*. **2013**, 120, 20798-20805

(163) Ly, T.H.; Perello, D.J.; Zhao, J.; Deng, Q.; Kim, H.; Han, G.H.; Chae, S.H.; Jeong, H.Y. and Lee, Y.H. Misorientation-angle-dependent Electrical Transport Across Molybdenum Disulfide Grain Boundaries. *Nature communications*. **2016**, 7, 10426.

(164) Azizi, A.; Zou, X.; Ercius, P.; Zhang, Z.; Elías, A.L.; Perea-López, N.; Stone, G., Terrones, M.; Yakobson, B.I. and Alem, N. Dislocation Motion and Grain Boundary Migration in Two-dimensional Tungsten Disulphide. *Nature communications.* **2014,** 5, 4867.

(165) Luo, S.; Hao, G.; Fan, Y.; Kou, L.; He, C.; Qi, X.; Tang, C.; Li, J.; Huang, K. and Zhong, J. Formation of Ripples in Atomically Thin MoS_2 and Local Strain Engineering of Electrostatic Properties. *Nanotechnology*. **2015**, 26, 105705.

(166) Lin, J.; Pantelides, S.T. and Zhou, W. Vacancy-induced Formation and Growth of Inversion Domains in Transition-metal Dichalcogenide Monolayer. *Acs Nano.* **2015,** 9, 5189-5197.

(167) Wang, J.; Namburu, R.R.; Dubey, M. and Dongare, A.M. Origins of Ripples in CVD-grown Few-layered MoS_2 Structures under Applied Strain at Atomic Scales. *Scientific reports.* **2017**, 7, 40862.

(168) Miró, P., Ghorbani-Asl, M. and Heine, T. Spontaneous Ripple Formation in MoS_2 Monolayers: Electronic Structure and Transport effects. *Advanced Materials.* **2013**, 25, 5473-5475.

(169) Lin, Z.; Carvalho, B.R.; Kahn, E.; Lv, R.; Rao, R.; Terrones, H.; Pimenta, M.A. and Terrones, M. Defect Engineering of Two-dimensional Transition Metal Dichalcogenides. *2D Materials.* **2016**, 3, 022002.

(170) Dolui, K.; Rungger, I.; Pemmaraju, C.D. and Sanvito, S. Possible Doping Strategies for MoS_2 Monolayers: An ab Initio Study. *Physical Review B.* **2013**, 88, 075420.

(171) Cheng, Y.C.; Zhu, Z.Y.; Mi, W.B.; Guo, Z.B. and Schwingenschlögl, U. Prediction of Two-dimensional Diluted Magnetic Semiconductors: Doped Monolayer MoS_2 Systems. *Physical Review B.* **2013**, 87, 100401.

(172) Feng, N.; Mi, W.; Cheng, Y.; Guo, Z.; Schwingenschlögl, U. and Bai, H. First Principles Prediction of The Magnetic Properties of FeX_6 (X= S, C, N, O, F) Doped Monolayer MoS_2. *Scientific reports*. **2014**, 4, 3987.

(173) Mishra, R.; Zhou, W.; Pennycook, S.J.; Pantelides, S.T. and Idrobo, J.C. Long-range Ferromagnetic Ordering in Manganese-doped Two-dimensional Dichalcogenides. *Physical Review B*. **2013**, 88, 144409.

(174) Lu, S.C. and Leburton, J.P. Electronic Structures of Defects and Magnetic Impurities in MoS_2 Monolayers. *Nanoscale research letters*. **2014**, 9, 676.

(175) Naveh, D. and Ramasubramaniam, A. Mn-doped Monolayer MoS_2: An Atomically Thin Dilute Magnetic Semiconductor. *In APS Meeting Abstracts.* **2014**.

(176) Zhang, K.; Feng, S.; Wang, J.; Azcatl, A.; Lu, N.; Addou, R.; Wang, N.; Zhou, C.; Lerach, J.; Bojan, V. and Kim, M.J. Manganese Doping of Monolayer MoS_2: The Substrate is Critical. *Nano letters.* **2015,** 15, 6586-6591.

(177) Laskar, M.R.; Nath, D.N.; Ma, L.; Lee, E.W.; Lee, C.H.; Kent, T.; Yang, Z.; Mishra, R.; Roldan, M.A.; Idrobo, J.C. and Pantelides, S.T. P-type Doping of MoS_2 Thin Films using Nb. *Applied Physics Letters*. **2014,** 104, 092104.

(178) Suh, J.; Park, T.E.; Lin, D.Y.; Fu, D.; Park, J.; Jung, H.J.; Chen, Y.; Ko, C.; Jang, C.; Sun, Y. and Sinclair, R. Doping Against the Native Propensity of MoS_2:

Degenerate Hole Doping by Cation Substitution. *Nano letters*. **2014**, 14, 6976-6982.

(179) Wang, S.Y.; Ko, T.S.; Huang, C.C. and Huang, Y.S. Optical and Electrical Properties of MoS_2 and Fe-doped MoS_2. *Japanese Journal of Applied Physics*. **2014**, 53, 04EH07.

(180) Lin, Y.C.; Dumcenco, D.O.; Komsa, H.P.; Niimi, Y.; Krasheninnikov, A.V.; Huang, Y.S. and Suenaga, K. Properties of Individual Dopant Atoms in Single-layer MoS_2: Atomic Structure, Migration, and Enhanced Reactivity. *Advanced materials*. **2014,** 26, 2857-2861..

(181) Li, B.; Huang, L.; Zhong, M.; Huo, N.; Li, Y.; Yang, S.; Fan, C.; Yang, J.; Hu, W.; Wei, Z. and Li, J.. Synthesis and Transport Properties of Large-scale alloy $Co_{0.16}Mo_{0.84}S_2$ Bilayer Nanosheets. *ACS nano*. **2015**, 9, 1257-1262.

(182) Komsa, H.P.; Kotakoski, J.; Kurasch, S.; Lehtinen, O.; Kaiser, U. and Krasheninnikov, A.V. Two-dimensional Transition Metal Dichalcogenides under Electron Irradiation: Defect Production and Doping. *Physical review letters*. **2012,** 109, 035503.

(183) Ataca, C. and Ciraci, S. Functionalization of Single-layer MoS_2 Honeycomb Structures. *The Journal of Physical Chemistry C*. **2011**, 115, 13303-13311.

(184) Fitzgerald, E.A. Dislocations in Strained-layer Epitaxy: Theory, Experiment, and Aapplications. *Materials science reports*. **1991**, 7, 87-142.

(185) Herbut, I.F.; Juričić, V. and Vafek, O. Coulomb Interaction, Ripples, and The Minimal Conductivity of Graphene. *Physical review letters.* **2018,** 100, 046403.

(186) Park, C.H.; Son, Y.W.; Yang, L.; Cohen, M.L. and Louie, S.G. Electron Beam Supercollimation in Graphene Superlattices. *Nano letters.* **2008**, 8, 2920-2924.

(187) Isacsson, A.; Jonsson, L.M.; Kinaret, J.M. and Jonson, M. Electronic Superlattices in Corrugated Graphene. *Physical Review B.* **2008,** 77, 035423.

(188) Brey, L. and Palacios, J.J. Exchange-induced Charge Inhomogeneities in Rippled Neutral Graphene. *Physical Review B.* **2008**, 77, 041403.

(189) Guinea, F.,; Horovitz, B. and Le Doussal, P. Gauge Field Induced by Ripples in Graphene. *Physical Review B.* **2008**, 77(20), p.205421.

(190) De Parga, A.V.; Calleja, F.; Borca, B.M.C.G.; Passeggi Jr, M.C.G.; Hinarejos, J.J.;

Guinea, F. and Miranda, R. Periodically Rippled Graphene: Growth and Spatially Resolved Electronic Structure. *Physical review letters*. **2008**, 100, 056807.

(191) Lee, C.; Wei, X.; Kysar, J.W. and Hone, J. Measurement of the Elastic Properties and Intrinsic Strength of Monolayer Graphene. *Science*. **2008**, 321, 385-388.

(192) Morozov, S.V.; Novoselov, K.S.; Katsnelson, M.I.; Schedin, F; Elias, D.C.; Jaszczak, J.A. and Geim, A.K. Giant Intrinsic Carrier Mobilities in Graphene and Its Bilayer. *Physical review letters.* **2008,** 100, 016602.

(193) Deng, S. and Berry, V. Wrinkled, Rippled and Crumpled Graphene: An Overview of Formation Mechanism, Electronic Properties, and Applications. *Materials Today*. **2016**, 19, 197-212.

(194) Jiang, J.W. The Buckling of Single-layer MoS_2 under Uniaxial Compression. *Nanotechnology*. **2016**, 25, 355402.

(195) Jiang, J.W. The Strain Rate Effect on The Buckling of Single-layer MoS_2. *Scientific reports*. **2015**, 5, 7814.

Chapter 3

Methodology

3.1 Introduction

In this chapter, I aim to introduce the basic experimental techniques and analytical methodologies employed in the project. It ranges from synthesizing the few-layered TMDs via controlling the CVD procedure, transferring the as-prepared sample for optical, SEM and TEM observation to processing and analyzing the acquired images. Details of the experiments and analysis are covered in this chapter for the repeatability of my work.

3.2 CVD Synthesis and Transfer of TMDs

3.2.1 Substrate Preparation

The substrates used to grow MoS_2 and WS_2 monolayers, SiO_2(300 nm)/Si(2 cm× 2 cm×0.5 mm, University Wafer), were sonicated for 10-15 min in acetone and isopropanol solutions successively.

3.2.2 CVD Synthesis of Few-layered WS_2 and MoS_2

The monolayer and few-layer MoS_2 domains were grown by hydrogen-free APCVD with the precursors of molybdenum trioxide (MoO_3, powder, ≥99.5%, Sigma-Aldrich) and sulfur (S, powder, ≥99.5%, Sigma-Aldrich).[1] P-doped silicon (Si) coated with a 300 nm thick oxide layer (amorphous SiO_2) was used as the substrate. Double-walled quartz tubes were employed for the CVD synthesis to avoid cross-reaction between the precursors. As

shown in **Figure 3-1**, two separate furnaces were utilized for individual temperature control. The MoO_3 (15 mg) loaded in the inner tube (0.6 inch diameter) was placed in the central zone of the low-temperature furnace, and the S (600 mg) in the outer tube (1 in. diameter) was placed 1.7 cm from the left open end of the high-temperature furnace. The substrate was located at the center of low-temperature furnace. The growth system was first flushed with 500 sccm argon (Ar) for 30 min to drive off the oxygen. Then, the furnaces were ramped to ~180 and ~200 °C, so as to create a Sulfur-rich environment. Next, furnace 2 was heated up to 800 °C, and meanwhile, the temperature of MoO_3 was increased to 300 °C. Once the target temperature was reached, MoS_2 began to nucleate with the 150 sccm Ar flow. This stage lasts for 20 min, after which the flow rate was reduced to 50 sccm for a 25 min growth. The temperature of S was increased slowly from 180 to 200 °C since then to maintain the concentration of S vapor at a nearly constant level. The growth time could be extended to 15 min to obtain bilayers, with the second-layer islands located on top of the large-area monolayer. To attain high uniformity and large domain size, we designed a follow-up procedure that enabled atom migrations, where the MoO_3 temperature was reduced to 270 °C and the gas flow rate was dropped to 5 sccm for a lower precursor feedstock, with a quenched substrate temperature of 700 °C to decrease the sublimation of MoS_2 species formed on the substrates. The time for obtaining a large domain size was optimized to be 15 min. Finally, the synthesis ended up with cooling fast.

A similar strategy was adopted to produce few-layered WS_2. The monolayer WS_2 domains were grown by hydrogen-free chemical vapor deposition in atmospheric pressure with the reactants of tungsten trioxide (WO_3, powder, 99.9%, Sigma-Aldrich) and sulfur (S, powder, ≥99.5%, Sigma-Aldrich). To avoid solid-phase reactions between the two precursors, 200

mg WO_3 was first placed in a smaller quartz tube, which was then mounted into a larger quartz tube with 400 mg S preloaded. While loading the precursors and the substrate, the S and WO_3 were put at the centers of the low- and high-temperature furnaces, respectively, and a 300 nm SiO_2/Si chip was positioned 9.5 cm downstream of the WO_3. Argon was introduced with a flow rate of 250 sccm to transport the precursor vapors onto the substrate surface. Two furnaces were used for independent temperature control. The S reached its target temperature of 180 °C 10 min before WO_3 was finally heated to 1070 °C (ramp rate: ≈30 °C min^{-1} for sulfur and ≈40 °C min^{-1} for WO_3). The reaction then lasted for 5 min, after which the sample was rapidly cooled down to room temperature. Similar with the MoS_2 bilayer synthesis, we extended the growth time to 10 min to obtain WS_2 bilayers

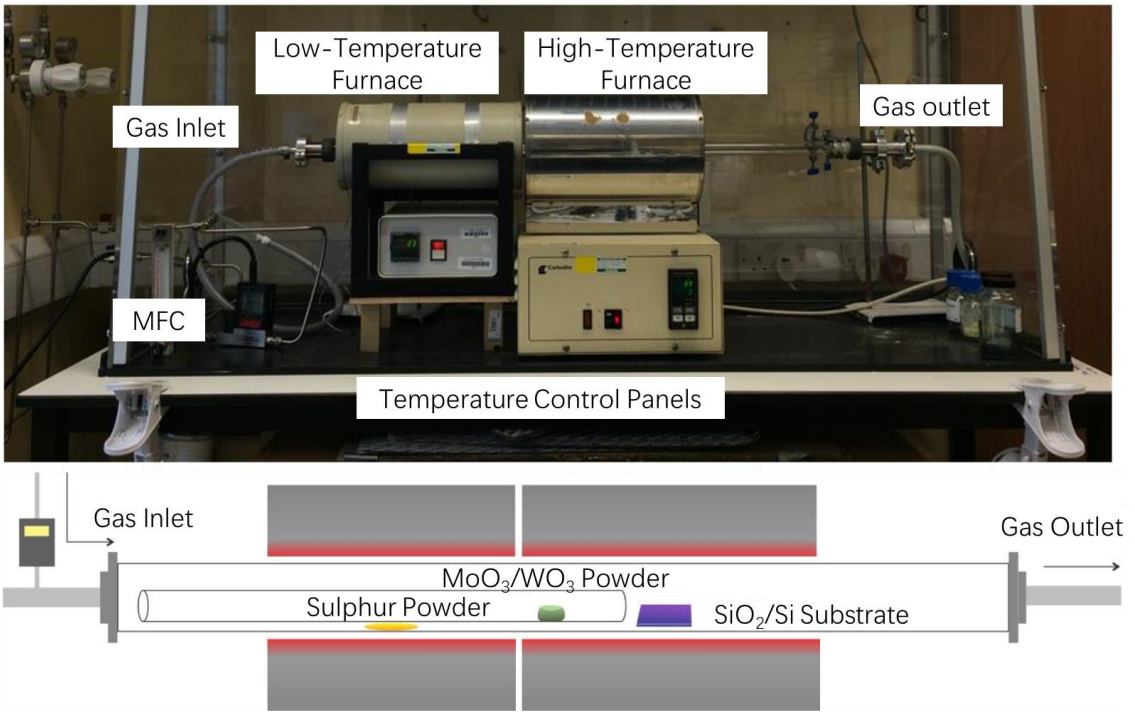

Figure 3-1 Photograph and schematic diagram showing the CVD synthesis of monolayer and few-layer MoS_2 and WS_2.

3.2.3 Transfer of Few-layered WS_2 and MoS_2

The as-grown few-layer MoS_2 and WS_2 on the SiO_2/Si substrate can be transferred onto an arbitrary substrate, such as Si_3N_4 TEM grids, for further characterizations using a polymer-assisted method. Its surface was first spin-coated with a thin film of poly-methyl-methacrylate (PMMA, 8% wt. in the anisole, 495 molecular weight) as a supportive scaffold. The rotation speed of the main spin-coating stage was programmed to 4500 rpm (round per minute) for 50 seconds with an initialization stage and an ending stage, both having a slow spin speed of 500 rpm for 5 seconds. Therefore, the deposited PMMA droplets can first wet the surface well at a low spin speed stage and then be spread into a uniform thin film at a high spin speed stage with the droplets being spun off the edges and the solvent being evaporated. After this, the sample was heated at 180 °C in the air on a hot plate for 90 seconds to remove the residual solvent thoroughly and strengthen the interlayer contact between MoS_2 and the PMMA layer. Subsequently, the PMMA/MoS_2/SiO_2/Si specimen was floated on a 1 mol/L potassium hydroxide (KOH, Sigma-Aldrich reagent grade 90%) solution, so that the PMMA/MoS_2 layer can detach from the substrate after SiO_2 being etched away. It is worth noting that, since the PMMA also covered the edges of the SiO_2/Si substrate when it was spread by the centrifugal force, all the edges of the SiO_2/Si substrate were rubbed by a diamond file before floating the sample on a KOH solution. This is to remove the coated PMMA layer on edges such that the SiO_2 can be exposed to contact directly with the KOH solution. After the PMMA/MoS_2 film peeled off, it was then transferred to the deionized water for several times to wash off any residual contamination from the etching process. The rinsed PMMA/MoS_2 film was then scooped up by a holey Si_3N_4 TEM grid (Agar Scientific AG21580) or other substrates,

air-dried for overnight and baked at 180 °C for 15 minutes to ensure a strong interface contact between MoS_2 monolayers and the new substrate. Finally, the PMMA scaffold was removed by submerging the new sample in the acetone solution for 8 hours.

3.3 Optical Microscopy and Scanning Electron Microscopy

Optical microscopy (OM) is useful for characterisation of large TMD domains, and particularly, is featured with unique layer-dependent optical contrast. Two OM set-ups were employed in my DPhil projects, namely the Mitutoyo objective lens with a 50× magnification attached to the CMOS camera (DCC1645C Thorlabs high-resolution 1280×1024 CMOS camera with a color sensor), and the one implemented into the Raman system. The former one is capable of providing optical microscopic images with good contrast and resolution of the prepared MoS_2 on SiO_2/Si substrate. Hence it was used to preliminarily examine the CVD-grown MoS_2 in terms of the uniformity in layer thickness, the domain size, and the nucleation density, as well as the vertically stacked heterostructures as shown in **Figure 3-2**(a). The latter one is inferior regarding the optical contrast and resolution, but it sufficed for recognizing the bilayer region with regard to the monolayer MoS_2 components that required Raman and PL measurements.

Scanning electron microscopy (SEM) is a powerful tool to characterize material's surface topography. This stems from its image generation mechanism, where the contrast originates from the secondary electrons (SEs) excited by the incident beam on the sample surface and only those SEs generated within a few nanometers of the surface can escape. In this project, Hitachi S-4300 field emission scanning electron microscope was operated to characterize micrometer-scale features of the as-grown monolayer and bilayer MoS_2,

including the nucleation density, domain size and shape, layer number and film continuity. All specimens were on SiO_2/Si substrates. The SEM sample was mounted onto the sample stub firmly using carbon sticky pads, which can diminish unwanted charge-up. The accelerating voltage was set to be 3 kV coupled with a beam current of 10 μA. The choice of such a low accelerating voltage is for gaining clearer surface structures with less electron charging and irradiation damage to samples. A SEM image of a sample with both monolayer islands and secondary layers is shown in **Figure 3-2**(b).

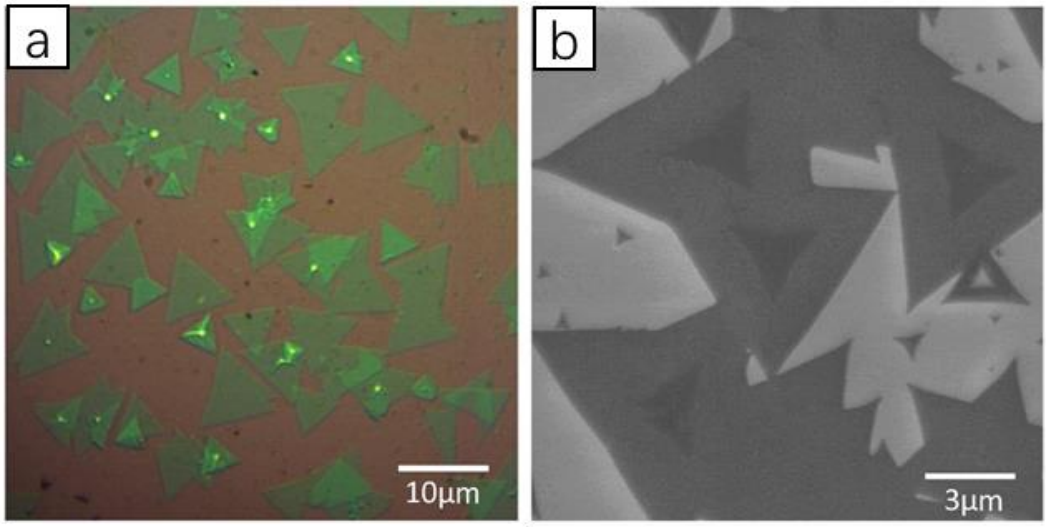

Figure 3-2 Observation of monolayer and few-layer MoS_2 samples using (a) Optical microscopy and (b) Scanning electron microscopy in SE mode.

3.4. Transmission Electron Microscopy

3.4.1. Aberration-Corrected Transmission Electron Microscopy

TEMs have long been applied for the characterization of lattice deformation in crystals. Since 1956, 100 kV TEM has been used in the observation of dislocation movements in aluminum. With the improvement in mechanical and electronic stabilities and the

correction of aberrations, the spatial resolution of 0.3nm has been achieved in 70s. Recently, monochromators have been developed to minimize the chromatic aberration and spherical aberration has been further reduced. The most state-of-art high-resolution transmission electron microscopy (HR-TEM) has leaped forward to angstrom scale resolution well below 78pm. A TEM system with two basic operations is shown in **Figure 3-3.**[2]

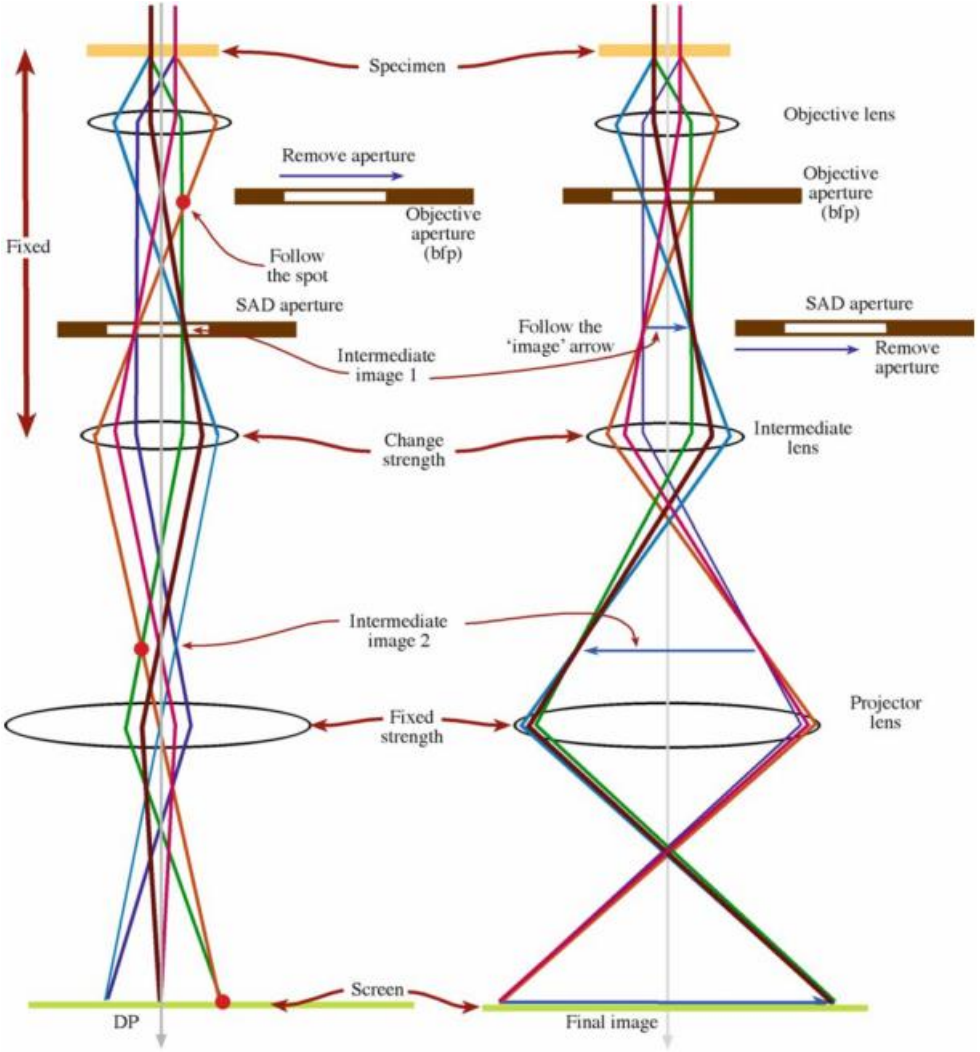

Figure 3-3 Two basic operations of the TEM imaging system involve diffraction mode: projecting the DP onto the viewing screen and image mode: projecting the image onto the screen. In each case the intermediate lens selects either the BFP or the image plane of the objective lens as its object. Reprinted with permission from ref. 2 ©Copyright 2009, Springer US.

The theoretical resolution of the electron lens and ultimately of the TEM is customarily defined in terms of the diffraction limit. However, the practical resolution is severely limited by spherical aberration, chromatic aberration and astigmatism. Spherical aberration is a feature of all round lenses that causes image blurring and most influences the resolution. This defect happens when the lens field acts differently on the rays depending on their off-axis angle. For our aberrated electromagnetic lenses, the further off axis the electron is, the more strongly it is over-bent back the axis. As a result, a point object is imaged as a disk of finite size which limits our ability to magnify details because the detail is degraded by imaging process. According to **Figure 3-4**, the way that a corrector compensates for Cs in a magnetic lens is in effect to create a diverging, for example "concave" lens which spread out the off-axis beams such that they re-converge to a point rather than a disk in the Gaussian image plane.[2] In practice, this correction can be achieved by a highly complex, computer-controlled set of quadrupoles and hexapoles or octupoles. After spherical aberration correction, all rays are more or less brought to a common focus which results in a sharper image. Therefore, it is possible to determine not just how individual atoms are brought together to form a bulk solid, but also help to distinguish atoms of differing chemical identity.

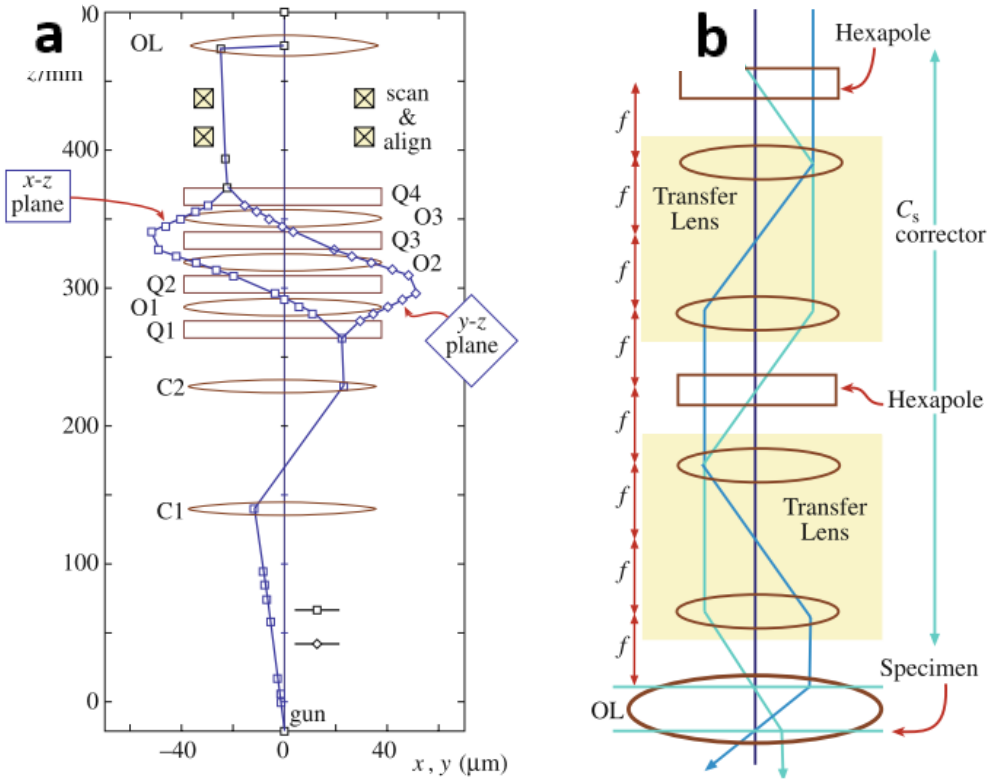

Figure 3-4 Ray diagrams showing how the two different commercial systems use (a) multiple quadrupole (Q) and octupole (O) lenses (Nion) or (b) hexapole and other transfer lenses (CEOS) to correct for Cs. Reprinted with permission from ref. 2 ©Copyright 2009, Springer US.

In my research, the aberration-corrected transmission electron microscopy (AC-TEM) was conducted using Oxford's JEOL JEM-2200MCO field emission gun TEM (OJ2200 MCO) under an accelerating voltage of 80 kV. [3] The microscope is remotely controlled, thus ensuring an extremely stable environment for image acquisition. The base pressure in the specimen chamber is ~10^{-4} Pa. The aberration correctors consisting of pairs of hexapoles are designed by CEOS, which are capable of correcting aberrations up to the third order as shown in **Figure 3-5**(a). [2] The spherical aberration (C_S) is corrected by running a Zemlin tableau on a thin amorphous area within a predefined range for the beam tilt angle at a magnification of ~500K. A series of diffractograms corresponding to different beam tilt angles are automatically recorded, which are used to correct C_s based on the wave

aberration function by the software. After each run, a phase plate was shown and the values for aberrations were listed, which was the guidance for the corrections that should further be made (**Figure 3-5**(b and c)). The correction completed when all the values were within the range of the targeted values (**Figure 3-5**(d)). After Cs being adjusted (either to 0 or to a deliberate finite small value), the resolution of the ACTEM system can reach ~1.2 Å. Images were recorded using a Gatan Ultrascan 4k×4k CCD camera with 1-2 s acquisition time, 2 pixel binning. The electron dose used for imaging was ~10^5 e^-/nm^2. Exposing TEM samples in the air induces the amorphous contamination accumulated on the surface of monolayer MoS_2, which blocks the direct observation of its pristine atomic configuration under TEM. Therefore, a dry-clean method was employed one day before the TEM characterization where samples were buried in the activated carbon powder and baked at ~200 °C in the air for ~ 60 min to remove adsorbates thoroughly.

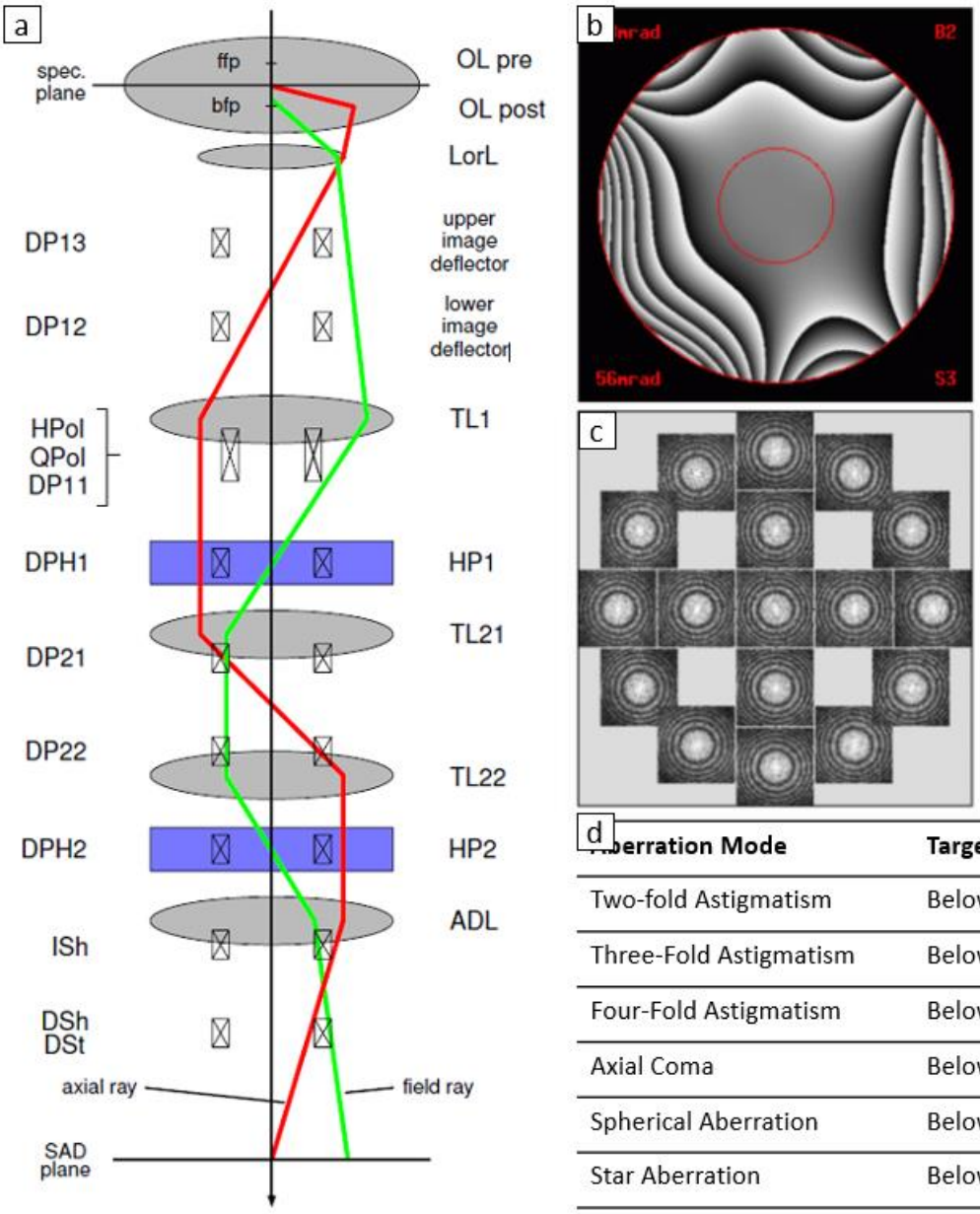

d

Aberration Mode	Target Value
Two-fold Astigmatism	Below 1nm
Three-Fold Astigmatism	Below 50nm
Four-Fold Astigmatism	Below 500nm
Axial Coma	Below 30nm
Spherical Aberration	Below 500nm
Star Aberration	Below 500nm

Figure 3-5 The electron optical elements of the CEOS and Zemlin tableau taken with an outer tilt angle of 23 mrad. (a) The corrector is mounted in the column between the objective lens and projective. Reprinted with permission from ref. 2 ©Copyright 2009, Springer US. (b) Phase plate and (c) diffractograms. (d) The target values of aberrations.

3.4.2. Scanning Transmission Electron Microscopy with *in-situ* Heating Holder

STEM is a specific type of TEM, which uses focused electron beam raster-scanning over the specimen. This makes STEM suitable for Z-contrast annular dark field (ADF) imaging, a more straightforward approach than TEM to image 2D materials composed of more than one element, including TMDs and h-BN, as one can directly distinguish the different elements only based on the contrasts. The first STEM was developed by von Ardenne in Berlin in 1938. However, the development of the technology ceased until 1970s, when Crewe and his colleagues built a field emission electron source for STEM and visualised single heavy atoms on a thin carbon film. By the early 1990s, better than 2Å resolution was achieved based on the development of STEM technology, indicating the possibility of direct imaging of atomic structures in some materials systems. The electron probe is able to be focused to sub-angstrom diameter with the combination of an aberration corrector, which boosted the resolution of STEM. In 2000, Dellby et al. presented 1.23 Å resolution in high-angle annular dark field (HAADF) images at 100 kV. A more advanced AC-STEM was then developed with 0.5 Å information limit. For the application of STEM on 2D materials atomic structural study, numerous publications can be found in recent years with single-atom sensitivity.

In my research, room temperature ADF-STEM was performed using an aberration corrected JEOL ARM300CF STEM equipped with a JEOL ETA corrector operated at an accelerating voltage of 60 kV located in the electron Physical Sciences Imaging Centre (ePSIC) at Diamond Light Source. [4] The convergence semi-angle used was 24.6 mrad with a camera length of 20 cm, corresponding to an annular recording range of 39–156 mrad at the detector plane. The electron probe diameter was focused to ~72 pm with a dwell time

ranging from 10–20 µs per pixel for imaging. The beam current was measured as 23 pA. ADF-STEM imaging at high temperatures up to 1100°C was performed using a commercially available *in-situ* heating holder from DENS Solutions (SH30-4M-FS). The resistance of the platinum coil in the heating chip (DENS Solutions DENS-C-30) is monitored in a four-point configuration, and the temperature is calculated using the Callendar-Van Dusen equation (with calibration constants provided by the manufacturer). Slits were produced into the Si_3N_4 membranes focused ion beam milling before transferring the bilayer samples onto the heating chip. The detailed structures of the heating chip and heating holder are shown in **Figure 3-6**.

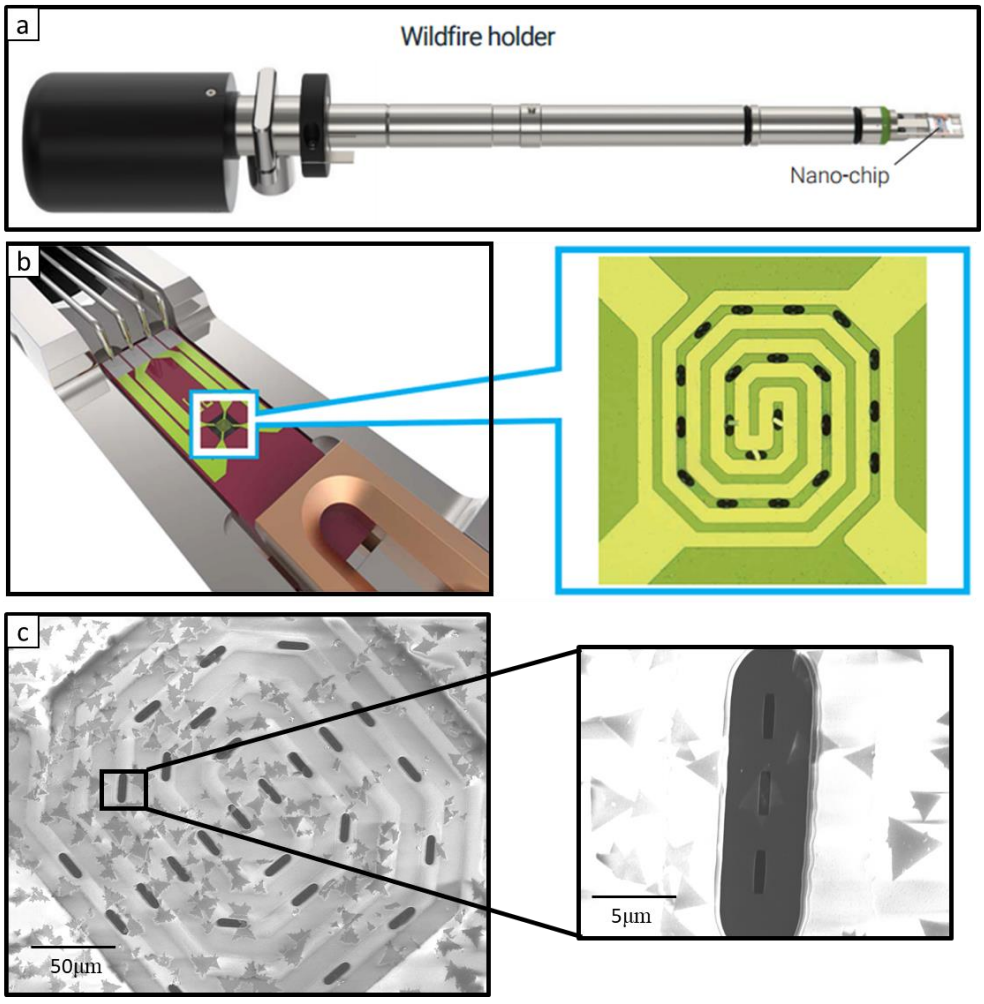

Figure 3-6 The detailed structures of an *in-situ* heating holder and heating chip. (a) a photograph of the heating holder. (b) Schematics of the heating chip. Reprinted with permission from ©Copyright DENSsolution. (c) Different magnification SEM images of the heating chip and slits manufactured by FIB.

3.5 References

(1) Wang, S.; Pacios, M.; Bhaskaran, H.; Warner, J. H. Substrate Control for Large Area Continuous Films of Monolayer MoS_2 by Atmospheric Pressure Chemical Vapor Deposition. *Nanotechnology* **2016**, 27, 85604.

(2) David, B. W.; Barry, C.; Warner, J. H. Transmission Electron Microscopy. *Springer* **2009**, 153.

(3) Mukai, M.; Kim, J. S.; Omoto, K.; Sawada, H.; Kimura, A.; Ikeda, A.; Zhou, J.; Kaneyama, T.; Young, N. P.; Warner, J. H.; et al. The Development of a 200kV Monochromated Field Emission Electron Source. *Ultramicroscopy* **2014**, 140, 37–43.

(4) Hosokawa, F.; Sawada, H.; Kondo, Y.; Takayanagi, K.; Suenaga, K. Development of Cs and Cc Correctors for Transmission Electron Microscopy. J. *Electron Microsc. (Tokyo).* **2013**, 62, 23–41.

Chapter 4

Vacancies and Line Defects in MoS_2 Bilayers

4.1 Introduction

Transition metal dichalcogenides (TMDs), such as MoS_2 and WS_2, are direct band gap semiconductors in their monolayer form, and indirect in bulk[1-4]. They offer band gaps in the red visible spectrum and semiconducting properties that expand the application of 2D materials beyond what graphene alone can achieve[5-7]. The presence of defects in TMDs influences the photoluminescence spectra, electronic transport behavior and photosensing capabilities[8-12]. Understanding the structure of defects is important for developing an accurate picture of their impact on properties. Aberration corrected transmission electron microscopy (AC-TEM) is one of the leading approaches to study the atomic structure of defects in 2D materials[13].

With the availability of monolayer TMDs, detailed atomic level studies of vacancies in MoS_2 and other S and Se based TMDs have been performed[14-24]. However, no detailed studies of the structure and dynamics of defects in bilayer TMDs have been reported. MoS_2 or WS_2 bilayers have two natural stacking forms: 3R and 2H stacking with 2H dominating due to energetic preference[25-26]. Most of recent work has been focused on 2H stacking structure and related optical properties [27] and few have been done on 3R stacked MoS_2 due to its relative rarity[28].

Upon 80 kV electron beam irradiation of MoS_2 and WS_2, the S vacancies are created and are also mobilized, resulting in point defects combining into line defects[14, 29-32]. The line

defects in MoS_2 can extend in length and also in width. As the length of a 1SVL defect increases, large lattice compression occurs to accommodate the loss of S atoms and change in charge density around the Mo atoms. This also causes large out of plane distortion to the monolayer sheet, similar to the buckling in graphene monolayers caused by dislocations[33]. The ability for monolayer sheets to buckle when defects are introduced plays an important role in strain relief [34]. Recent work showed that heating graphene to high temperatures causes the substrate it was attached to expand and produce tension on graphene[35]. This in turn caused partial dislocations to occur because single dislocation cores are only stable when accompanied by out of plane buckling. The ability for a 2D material to accommodate buckling and defects is expected to be different as more layers are added, due to the interlayer van der Waals forces. Unique interlayer interactions have been previously seen in bilayer graphene with very small mismatch angles between the layers causing local regions of commensurate and incommensurate stacking[36]. Recent work showed that as the width of line vacancies in MoS_2 increases, the rows of S vacancies lines are staggered from top to bottom to enable stable bond restructuring[12]. The reconstructed bonds have different unit cell structure, and this will cause changes in the local van der Waals interactions with the second layer in bilayer 2D systems. Furthermore, the compression associated with the multiple stacked line vacancies in MoS_2 will cause local shifts in atomic positions extending out from the defect region and this will give rise to competition between in-plane compression around defects, and interlayer van der Waals forces and associated 2H and 3R stacking phases.

In this study, MoS_2 samples are grown on Si substrates with 300nm oxide layer using methods based on our prior work[12]. Samples of MoS_2 are predominantly monolayer, but

sometimes small bilayer domains are found. We study the structure and dynamics of defects in bilayer MoS_2 from the point defects to aggregated clusters. Both 2H and 3R stacked bilayers are examined due to their presence in the chemical vapour deposition grown samples. Density functional theory (DFT) calculations are used to provide accurate model structures for multislice image simulations to compare to the experimental phase contrast AC-TEM images.

4.2 Results and Discussion

4.2.1 Monolayer-Bilayer Interfaces in 2H and 3R Stacked MoS_2 Bilayers

From the as-grown sample in **Figure 4-1**(a), monolayer and few-layer MoS_2 coexist and are distinguished by optical contrast. Photoluminescence (PL) spectra in **Figure 4-1**(b) are obtained from monolayer and bilayer regions marked by red and black in the inset, respectively, further indicating the coexistence of monolayers and multilayers in our MoS_2 sample. The SEM image in **Figure 4-1**(c) demonstrates nucleation of another MoS_2 layer on top of the monolayer triangles. Low magnification TEM image indicates clear boundaries between monolayer and bilayer regions which matches the optical microscope result (**Figure 4-1**(d)).

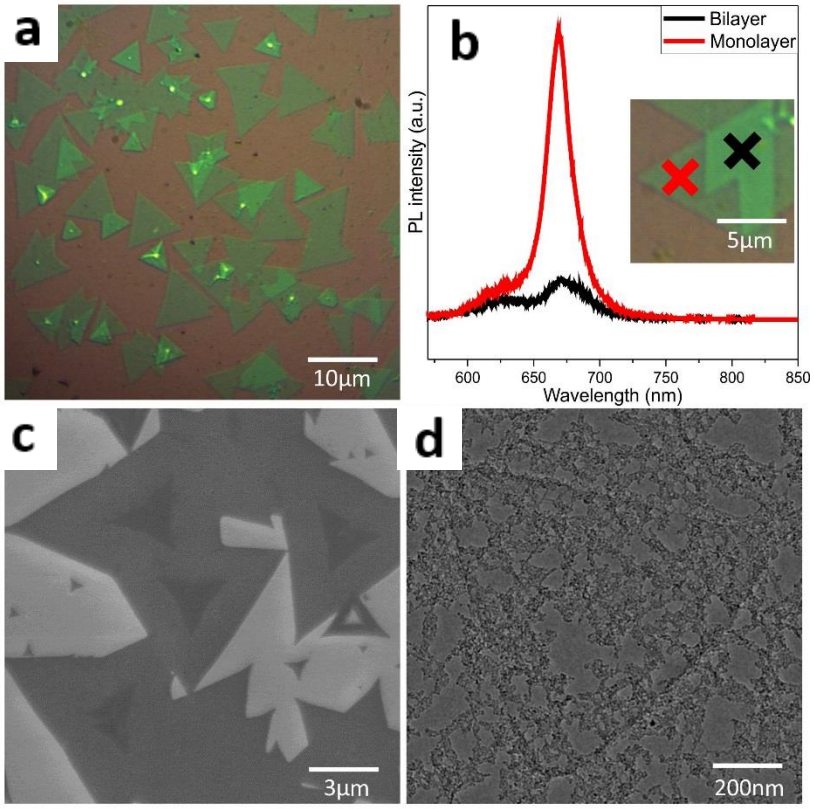

Figure 4-1. Optical images of a CVD growth of typical MoS_2 triangles on (a) SiO_2/Si (300 nm) substrate and (b) Photoluminescence spectra from monolayer and bilayer regions. (c) SEM image in SE mode of triangular multilayers grown on top of monolayer MoS_2. (d) Low magnification TEM image showing an isolated triangular crystal on top of monolayer MoS_2.

Two types of mono-bilayer step-edges were found in the AC-TEM images, **Figure 4-2**(a) and (c), corresponding to 2H and 3R stacking respectively. The 2H stacked bilayer region shows the expected AA' ordering, while the 3R bilayer shows the AB stacking leading to a more complex contrast pattern than the AA'. Multislice image simulations based on the atomic models (**Figures 4-2**(e-h)) match the experimental ones, confirming the two stacking structures, with the line profiles of the experimental and simulated images compared in **Figures 4-2**(i) and (j). AC-TEM images were processed by an 8 pixel Gaussian blur, followed by a "find edge" filter, then another 8 pixel Gaussian blur, and then using an "orange hot"-colored LUT, and finally, the contrast and brightness were

adjusted. To match the AC-TEM image, the simulation was performed using 1.6nm twofold astigmatism and 300 nm second-order coma (180°). The brightness and contrast of the simulated images were adjusted according to the intensity of the known columns in the experimental images

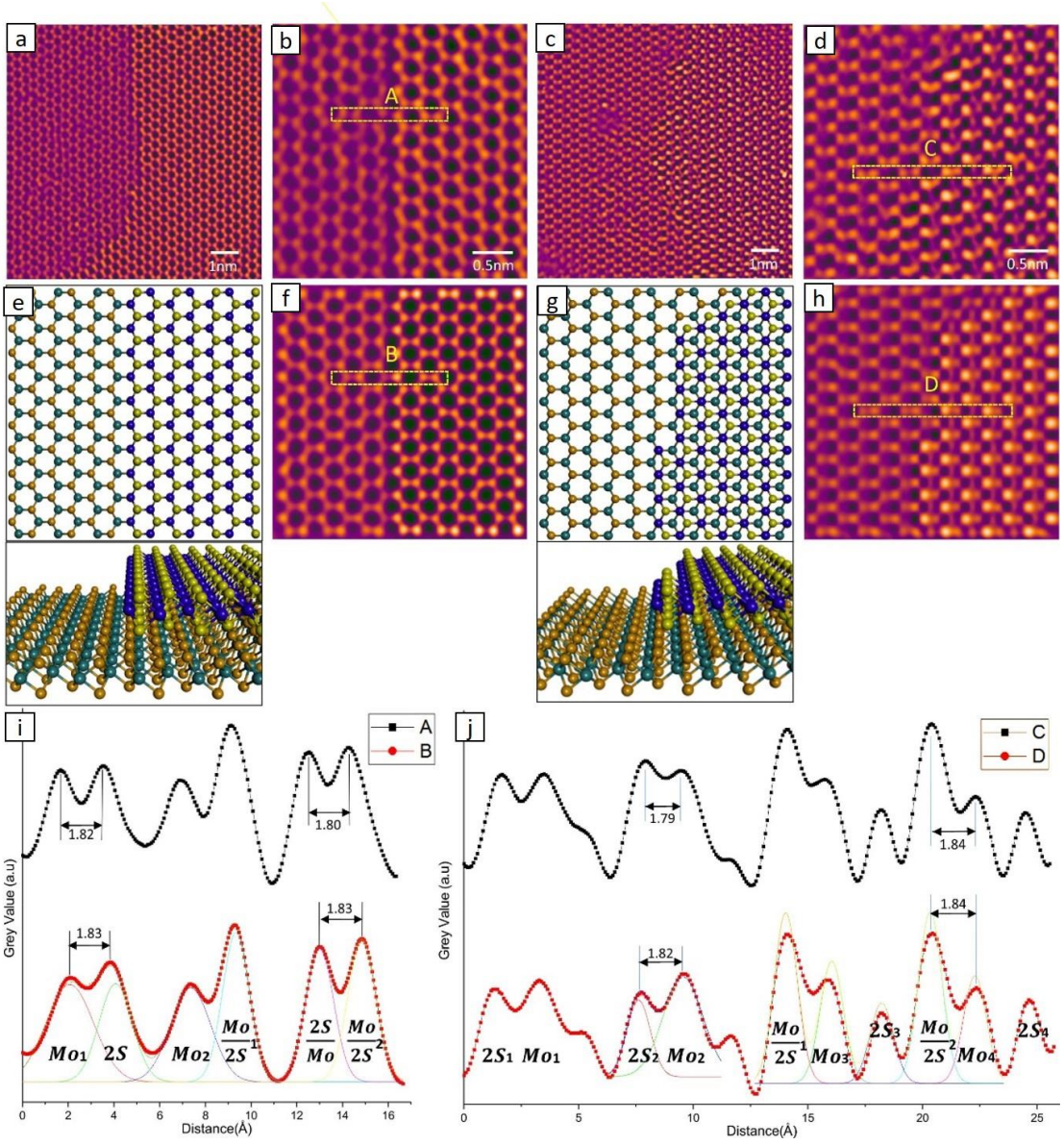

Figure 4-2 AC-TEM images of the MoS_2 monolayer-bilayer step edge for (a, b) 2H stacking and (c, d) 3R stacking. Atomic models from top and 3D view and corresponding multislice image

simulations for (e, f) 2H stacking and (g, h) 3R stacking. (i) Boxed line profiles of the step edge in (b) and (f). (j) Boxed line profiles of the step edge in (d) and (h).

4.2.2 Sulfur Vacancies in 2H Stacked MoS_2 Bilayers

We examine the presence of S vacancies in 2H stacked bilayer MoS_2, **Figure 4-3**. Electron beam irradiation at 80kV is known to introduce sulfur vacancies in MoS_2[13]. **Figure 4-3**(a) shows a typical AC-TEM image of 2H stacked bilayer, with visible weaker contrast spots marked by the white and red arrows. The magnified images in **Figure 4-3**(b) and (c) show two different levels of reduced contrast associated with single S vacancies (SVs) and double S vacancies (DVs) in the same column. Atomic models of 1SV (grey) and 1DV (red) from the DFT calculations are respectively shown in **Figure 4-3**(d) and (e) from both top (colored ball) and 3D views (colored cross). Corresponding multislice image simulations (**Figure 4-3**(f) and (g)) and the line profile analysis (**Figure 4-3**(h-i)) show good similarity with the experimental images, confirming SVs and DVs in 2H stacked bilayer MoS_2.

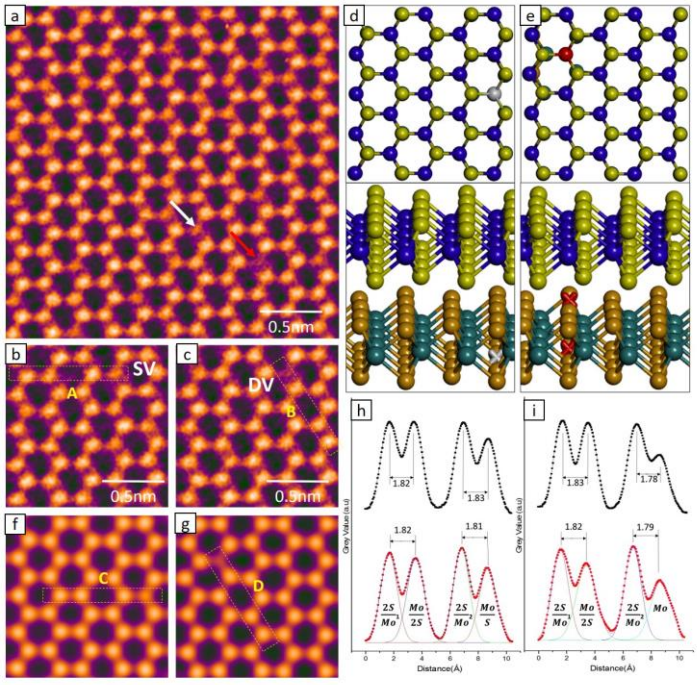

Figure 4-3 (a) AC-TEM image of single and double S vacancies in 2H stacked bilayer MoS_2 marked by white and red arrows, respectively. Zoomed in HRTEM image indicating (b) Single S vacancy and (c) Double S vacancy. (f, g) Multislice image simulations based on the DFT calculated atomic models with (d) one missing S atom and (e) two missing S atoms in the Mo-S-S column, respectively. The color key is SV=grey, DV=red. (h) Boxed line profiles at SV shown in (b) and (f). (i) Boxed line profiles at DV shown in (c) and (g).

4.2.3 Line Defects in 2H Stacked MoS_2 Bilayers

Under prolonged electron beam irradiation, SVs and DVs in 2H bilayer MoS_2 increase in density and start to aggregate into extended line defects as shown in **Figure 4-4**(a). The line defects in 2H bilayer MoS_2 can exist in variable lengths along the zig-zag directions and also gain width along the armchair direction, **Figure 4-4**(b-e). The magnified AC-TEM image in **Figure 4-4**(b) shows a 1SVL with length of 7SVs. The corresponding DFT-calculated model from top and 3D views (**Figure 4-4**(f)) shows negligible in-plane or out-of-plane lattice distortion triggered by losing seven S atoms in the bottom layer, which

differs from the prior studies of 1SVLs in monolayer MoS_2[13]. Two types of 2SVL are observed, **Figure 4-4**(c) and (d), with different S reconstruction. Two corresponding DFT-calculated models are evaluated (**Figure 4-4**(g) and (h)). Type A has 2SVL within only one MoS_2 layer with alternate staggering across top and bottom S sites. Based on previous report[12], the staggering configuration of two vacancy lines in the bottom layer are energetically preferred. Type B has one 1SVL in bottom and the other in the top MoS_2 layer to give an overall 2SVL defect spread across the two layers. The vacancy lines can exist in either plane of each layer. DFT calculations indicate that no obvious out-of-plane distortion occurs in either type A or B 2SVLs in the 2H bilayer, which is different to the 2SVL in monolayer MoS_2. The observation of a type B 2SVL also indicates the coexistence of S vacancies in both bottom and top layers in the 2H stacked MoS_2 bilayer. In **Figure 4-4**(e), a 3SVL is presented, showing similar structure as A-2SVL. The atomic model relaxed using DFT calculations (**Figure 4-4**(i)) shows staggered arrangement of SVLs in the bottom layer.

To quantify the lattice distortion introduced by each SVL in 2H bilayer MoS_2, Figure **4-4**(n), we measured the boxed line profiles across (Mo/2S)-$(2S/Mo)_1$-(Mo/S)-$(2S/Mo)_2$ columns as marked by green dashed rectangles for 1SVL (A), A-2SVL (B and C), B-2SVL (D and E) and 3SVL (F and G). The distance between each column is determined by fitting Gaussian curves, and plotted for A-G in **Figure 4-4**(o-q). For 1SVL, the $(2S/Mo)_1$-(Mo/S), (Mo/S)-$(2S/Mo)_2$ and (2S/Mo)1-$(2S/Mo)_2$ distances are 3.52, 1.83 and 5.38 Å, respectively. The negligible shrinkage compared with the column distances in pristine 2H bilayer MoS_2 confirms minimal compression in the system when losing seven S atoms in a layer. Line profiles along direction B and C, the left side SVL in A-2SVL, show no $(2S/Mo)_1$-(Mo/S)

distance change, but a slight drop in (Mo/S)-$(2S/Mo)_2$ and (2S/Mo)1-$(2S/Mo)_2$ distances. However, for the right side SVL, the $(2S/Mo)_1$-(Mo/S) and $(2S/Mo)_1$-$(2S/Mo)_2$ distance shrinks to 3.04 and 4.90 Å with small increase in the $(2S/Mo)_1$-(Mo/S) distance. These changes indicate greater compression is introduced between the two staggered SVLs. For the right side SVL, the $(2S/Mo)_1$-(Mo/S) distance increment indicating tension is caused by the displacement of S atoms in (Mo/S) towards (2S/Mo) column. The direction D and E in B-2SVL both show compression along the armchair direction. Compared with the A-2SVL, no tension exists in the defective regions and the contraction is relatively smaller, indicating the configuration having one sulfur vacancy line in each layer introduces less strain into the bilayer system. The staggered 3SVL has expansion in (Mo/S)-$(2S/Mo)_2$ distance and shrinkage in $(2S/Mo)_1$-$(2S/Mo)_2$ distance as expected.

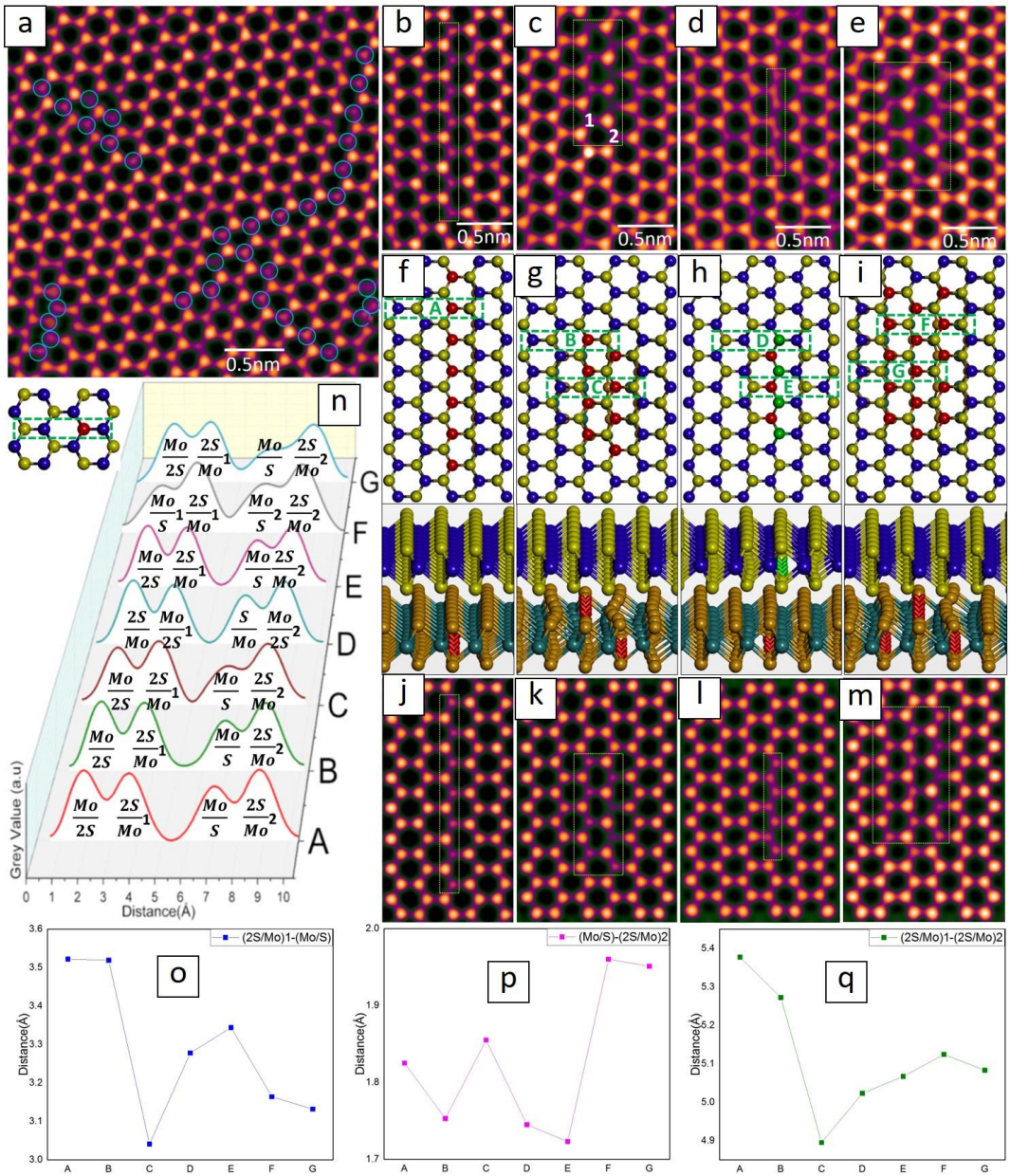

Figure 4-4 (a) AC-TEM image showing the aggregation of S vacancies into extended line defects along zigzag direction with different length and width. HRTEM images showing (b) 1SVL, (c) type A-2SVL, (d) type B-2SVL and (e) 3SVL with defective region in yellow dashed rectangle and (f-i) corresponding DFT-calculated atomic models. The S vacancies are marked by red in bottom and green in top layer (colored balls in top view and colored crosses in 3D view). (j-m) Multislice image simulations based on f, g, h and i, respectively. (n) Boxed line profiles taken along green dashed rectangles marked as A-G. Scattered line graphs displaying the distance between (o) $(2S/Mo)_1$ and (Mo/S), (p) (Mo/S) and $(2S/Mo)_2$ as well as (q) $(2S/Mo)_1$ and $(2S/Mo)_2$.

4.2.4 Differences Between Line Defects in MoS_2 Monolayers and Bilayers

Figure 4-5(a) shows multislice image simulation of 2H stacked bilayer MoS_2 with infinite long 1SVL running through the bottom layer based on the DFT-calculated atomic model in **Figure 4-5**(b). As discussed before, the introduction of 1SVL introduces negligible out-of-plane and in-plane lattice distortion. To compare the difference between the SVLs in monolayer and bilayer system, as shown in **Figure 4-5**(d), layer B is DFT-calculated model for monolayer MoS_2 with 1SVL running through, another pristine MoS_2 monolayer is manually placed on top to create similar 2H stacking configuration, taking the circled column as the alignment point. The corresponding multislice image simulation in **Figure 4-5**(c) shows considerable lattice distortion on the right hand of the 1SVL, resulting from the mismatch from two layers. Layer A and B are then extracted and stacked as shown in **Figure 4-5**(e), the column circled by black is chosen as the alignment point. From the side view, large discrepancy in the out-of-plane distortion between layer A and B can be distinguished. To quantify the lattice mismatch in the system, 2D displacement maps from x-, y- and z-axis are constructed in **Figure 4-5**(f-h), respectively. The reference point is circled in white. The displacement maps show significant compression with increased magnitude in the x direction. However, the lattice mismatch in the y direction is uniformly distributed and relatively small. The displacement map in the Z-axis shows centrosymmetric configuration with most significant Z-direction distortion in the defective site and lowest in the reference point, further confirming large out-of-plane distortion difference between the two layers.

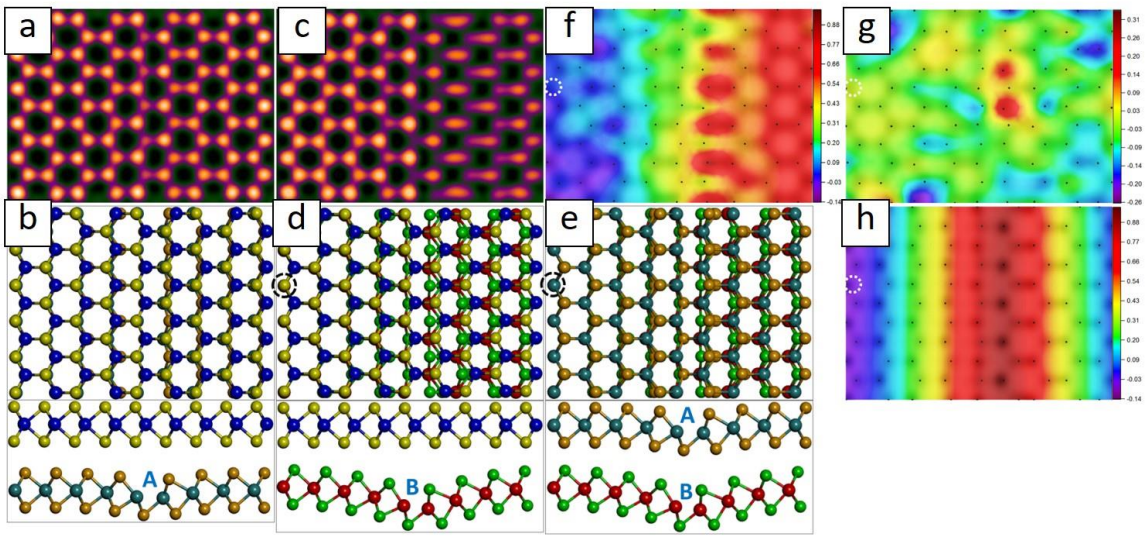

Figure 4-5 Multislice image simulations of (a) bilayer MoS_2 with 1SVL in layer A and (c) one pristine monolayer on top of one defective layer B and (b, d) corresponding DFT-calculated atomic models. (e) Atomic model of 'bilayer' composed by layer A and B. Two-dimensional displacement maps along (f) x, (g) y and (z) direction, respectively, which are laid on top of simulated image based on e. Alignment points are marked with black circle in image simulations and reference points are marked with white circles in displacement maps.

We further measure the bond length of Mo-S in the defective site (shown in **Figure** 4-6). For monolayer with 1SVL (**Figure 4-6**(a)), the Mo-S bond length along the defective site ranges from 2.333 to 2.579 Å, implying that the maximum increase or shrinkage of bond length compared to pristine crystal (2.420 Å) is 6.6%, which is 3.7% for the defective layer from bilayer as shown in **Figure 4-6**(b). This proves less in-plane compression introduced by 1SVL in bilayer system. Furthermore, the significant mismatch mainly derives from the out-out-plane lattice distortion. Compared to the value of 2.41 in pristine MoS_2, the maximum bond length deviation for layer A and B is respectively 3.7% and 6.6%, indicating that the compression in x direction also mainly comes from the out-of-plane distortion. Therefore, SVLs in monolayer system introduces slightly larger in-plane lattice deformation than those in bilayer counterparts. However, the main discrepancy between

the defective layer in mono and bilayer is the out-of-plane distortion. The considerable buckling introduced by SVLs in the monolayer MoS_2 becomes insignificant in bilayer system, mainly compensated by the interlayer van der Waals force.

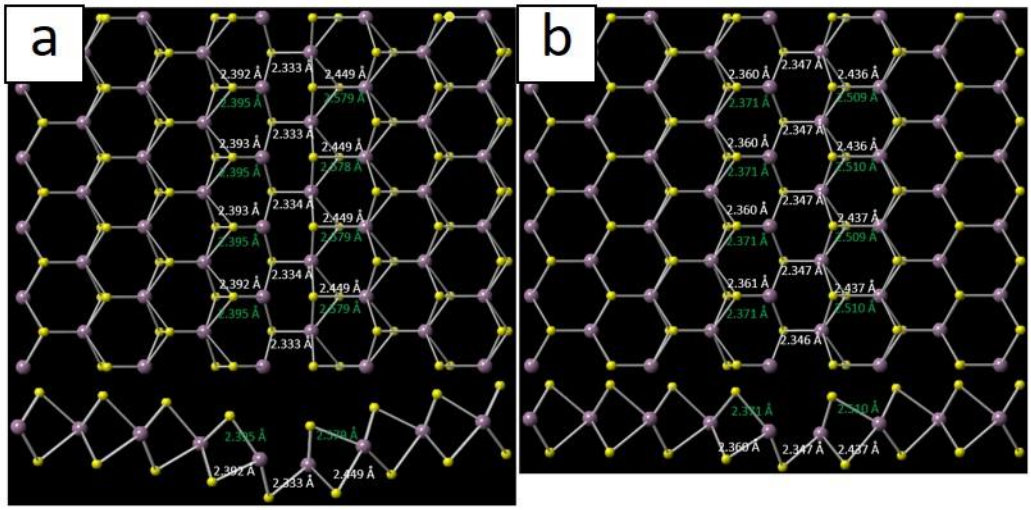

Figure 4-6 DFT-calculated models with 1SVL from both top and side view of (a) monolayer and (b) defective layer from 2H stacked bilayer MoS_2. Bond length is marked as white and green for Mo-S (bottom plane) and Mo-S (top plane), respectively. Standard Mo-S distance bond length is 2.420Å.

4.2.5 Dynamics of Sulfur Vacancies in 2H Stacked MoS_2 Bilayers

Sequential AC-TEM images in **Figure 4-7**(a) show dynamics of sulfur vacancies in 2H stacked bilayer MoS_2 during 89s of electron beam irradiation. A different false color LUT is applied to highlight every single S vacancies in each frame (**Figure 4-7**(b)). In **Figure 4-7**(c), grey scale image with red dots indicating SVs shows that during the first 25s, the 3SVL gains length in the B-zigzag direction. Vacancies initially aggregate along the A-zigzag direction from 25s to 43s. For the latter 46s, large number of vacancies along B-zigzag direction are quenched and the SVL transforms to 3SVL along the A-zigzag direction. In the first 43s, newly ejected S atoms adjacent to the 3SVL are introduced under

electron beam irradiation. In the next 46s, vacancies along B-zigzag direction get quenched by free S atoms or migrate to A-zigzag direction.

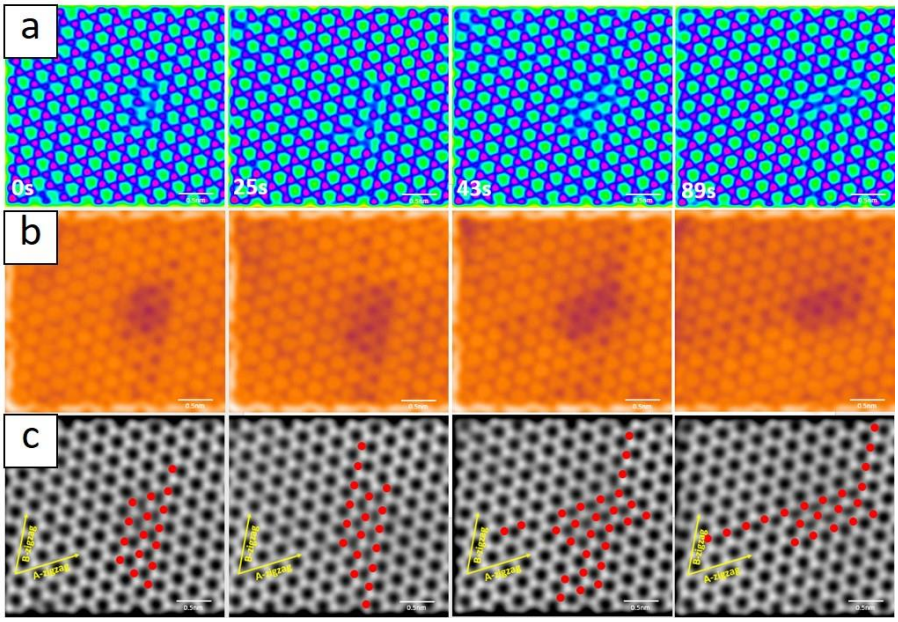

Figure 4-7 (a) Series of processed AC-TEM images showing the evolution of S vacancies in 2H bilayer MoS_2 over 89s (false color LUT used to highlight vacancies). (b) S vacancies highlighted as darker spots using different false color LUT. (c) Grey scale image showing vacancy migration and a 3SVL rotation from B-zigzag to A-zigzag direction (S vacancies marked as red dots).

4.2.6 Sulfur Vacancies in 3R Stacked MoS_2 Bilayers

The image frames shown from **Figure 4-8**(a-e) display the HRTEM image frames of 3R stacking bilayer MoS_2 under different focusing conditions, with three columns (2S/Mo), (Mo) and (2S) showing varying contrast. Multislice image simulations of 3R bilayer MoS_2 ranging from **Figure 4-8**(f-j) are conducted using defocus spread of 5nm and various defocus values to match the experimental results. For comparison, the simulated images of 2H bilayer MoS_2 (**Figure 4-8**(k-o)) are conducted using the same defocus values. This provides additional evidence of the 3R stacking sequence existing in our sample.

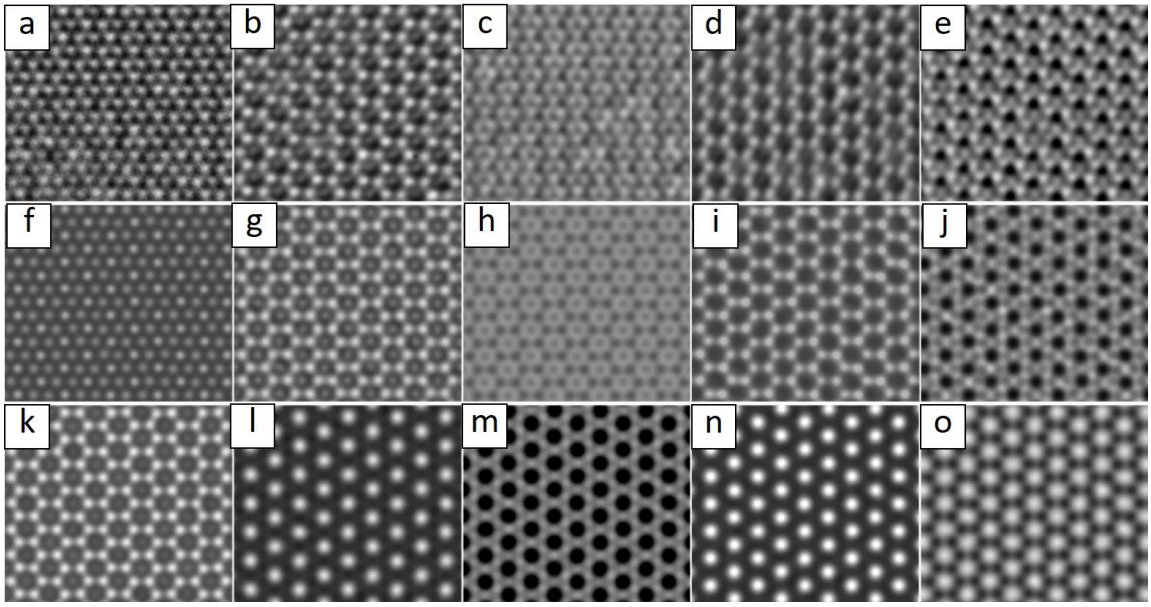

Figure 4-8 (a-e) HRTEM image showing unique contrast changes of 3R stacked bilayer MoS_2 under various focusing circumstances. Multislice image simulations under defocus value of -2, 7, -9, 10 and 4nm, respectively, for (f-j) 3R and (k-o) 2H stacked bilayer MoS_2. The defocus spread used is 5nm.

Monolayer-3R stacked bilayer interface has also been observed in our study (**Figure 4-9**). **Figure 4-9**(a) shows a typical AC-TEM image of 3R stacked bilayer MoS_2, in which a large number of bright spots (marked by white and purple arrows) and blurred regions (marked by green and red arrows) are observed. Magnified AC-TEM images in **Figure 4-9**(b-e) indicate single S vacancies SV_1, SV_2 and double S vacancies DV_1 and DV_2 as blurred regions, bright spots, heavily blurred regions and brighter spots, respectively. The existence of 3R stacked bilayer MoS_2 is confirmed by imaging the structure under different defocus values, leading to contrast pattern variations that the 2H structure cannot exhibit. The corresponding multislice image simulations under different defocus values match the experimental results. Atomic models relaxed by DFT, **Figure 4-9**(f-i), and their corresponding multislice image simulations, **Figure 4-9**(j-m) indicate that the blurriness is due to losing one (SV_1) or two (DV_1) S atoms in a 2S/Mo column and the bright contrast

is due to losing one (SV_2) or two (DV_2) S atoms in a 2S column. Intensity line profiles along the yellow arrows in both simulated and experimental images are taken covering the defective site. For both single S vacancies (SV_1 and SV_2), the Mo-Mo column distance remains close to that in pristine 3R bilayer MoS_2 (5.4 Å), implying nearly no compression is introduced to the bilayer by losing one S atom. In contrast, a column distance shrinkage of ~5% is observed for both DV_1 and DV_2, indicating small contraction caused by losing both S atoms in 2S or Mo/2S columns. These results are consistent with the SV/DV in 2H bilayer MoS_2. Further confirmation of the existence of SV/DVs in 3R stacked bilayer MoS_2 is obtained by measuring the peak intensity ratio at multiple defective sites as shown in **Figure 4-9**(n-q).

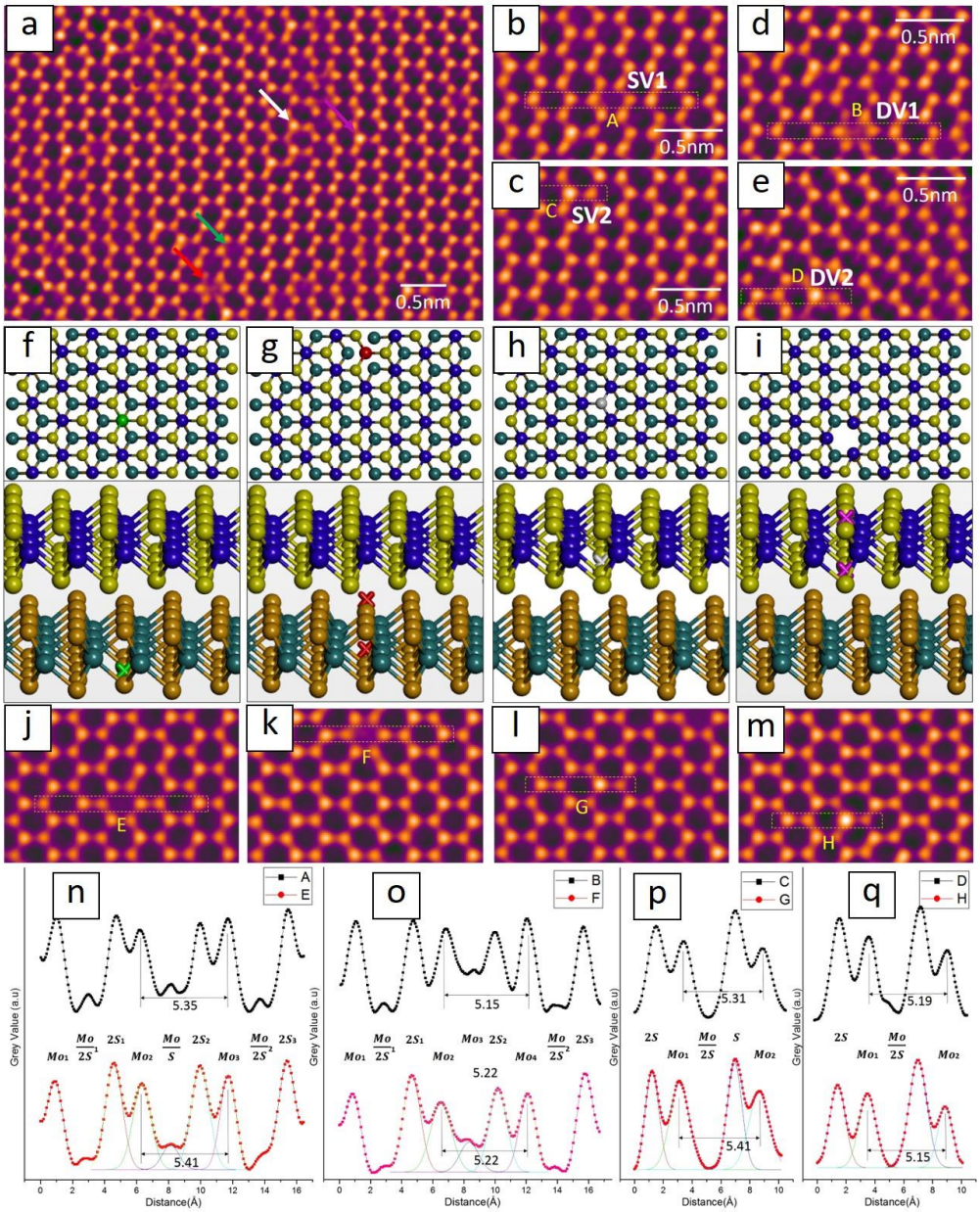

Figure 4-9 (a) AC-TEM image showing the distribution of S vacancies in 3R stacked bilayer MoS_2. The color key is SV_1=green, DV_1=red, SV_2=grey, DV_2=purple. Zoomed in HRTEM image indicating (b) SV_1, (c) SV_2, (d) DV_1 and (e) DV_2. (j, k, l, m) Multislice image simulations based on the DFT calculated atomic models of 3R stacked MoS_2 bilayer with (f) one missing S atom and (g) two missing S atoms in the Mo-S-S column, (h) one missing S atom and (i) two missing S atoms in the S-S column, respectively. Vacancies are marked as colored balls in top view and crosses in 3D view. (n-q) Boxed line profiles taken along yellow dashed rectangles marked as A-H.

4.2.7 Dynamics of Sulfur Vacancies in 3R Stacked MoS_2 Bilayers

Processed AC-TEM images in **Figure 4-10**(a) and (b) respectively highlight SV_2/DV_2 and SV_1/DV_1 as bright spots and dark regions. Bright SVs in bilayer 3R-stacked MoS_2 were processed by fast Fourier transform (FFT) band pass (100-1 pixels) and then a Gaussian blur of 12 pixels, followed by contrast adjustment. Dark S vacancies were processed by an FFT band pass filter (100-1 pixels), then a Gaussian blur of 8 pixels, followed by a find edge filter, and then another 6-pixel Gaussian blur, and then, the contrast was adjusted. **Figure 4-10**(c) demonstrates the evolution of SV_2/DV_2 (green) and SV_1/DV_1 (red) under electron beam irradiation. The number of each SV is calculated as a function of time as displayed in the histogram (**Figure 4-10** (d)) and the plot (**Figure 4-10** (e)). Throughout the frames, the ratio of SV_1/DV_1 to SV_2/DV_2 increases from 2.5:1 to 4.9:1, indicating the dominance of SV_1/DV_1. Therefore, for 3R stacked bilayer MoS_2, under 80kV irradiation, the S atoms in the 2S columns are more stable and less likely to be sputtered compared to those in the Mo/2S columns. Over 71s, the SV_2/DV_2 number drops slightly, whereas the density of SV_1/DV_1 increases especially in the last 37s. Hence, the most newly produced SV_1/DV_1 are derived from the prolonged irradiation. However, vacancy migration also happens from SV_2/DV_2 to SV_1/DV_1, implying vacancy migration between layers in 3R bilayer MoS_2.

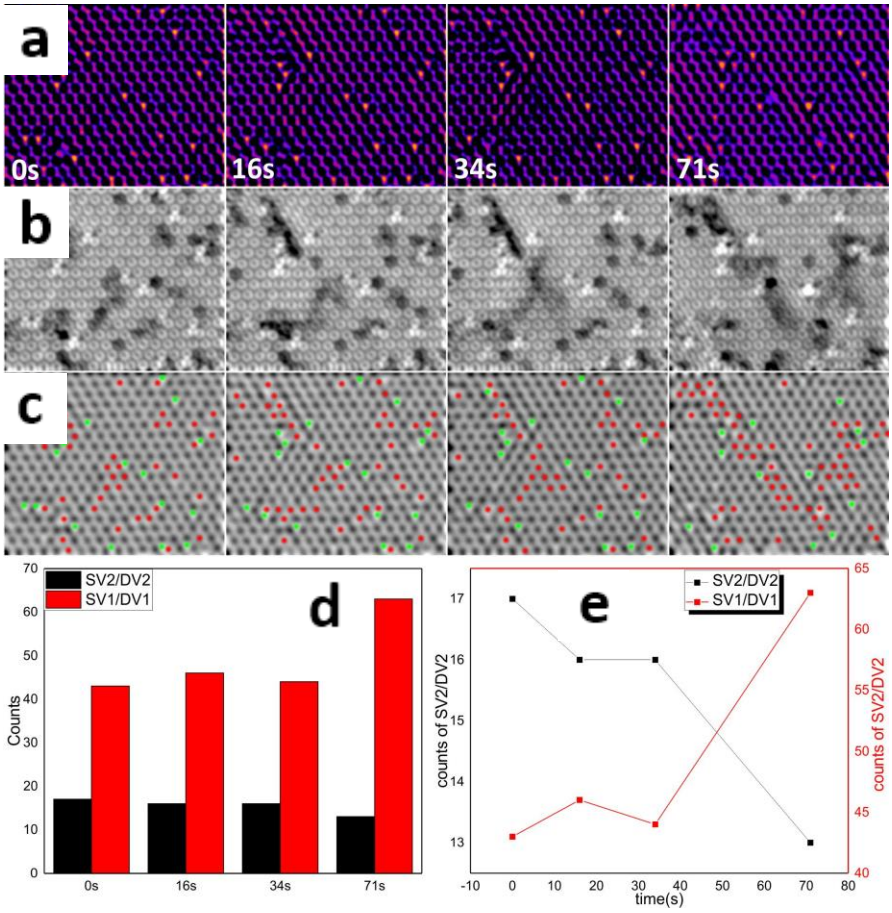

Figure 4-10 Processed AC-TEM images showing the evolution of (a) SV_2/DV_2 as bright spots and (b) SV_1/DV_1 as dimmed regions over 71s. Bright SVs in bilayer 3R-stacked MoS_2 were processed by fast Fourier transform (FFT) band pass (100-1 pixels) and then a Gaussian blur of 12 pixels, followed by contrast adjustment. Dark S vacancies were processed by an FFT band pass filter (100-1 pixels), then a Gaussian blur of 8 pixels, followed by a find edge filter, and then another 6-pixel Gaussian blur, and then, the contrast was adjusted. (c) Distribution of SV_1/DV_1 and SV_2/DV_2 marked as red and green spots, respectively. (d) Histogram and (e) trend lines representing the number change of SV_1/DV_1 and SV_2/DV_2 as a function of time.

4.3 Conclusion

AC-TEM imaging is conducted under accelerating voltage of 80kV, allowing production and aggregation of vacancies as well as atomic level resolution of defective regions in bilayer MoS_2. DFT-calculated models prove the different production and migration

mechanisms between sulfur vacancies in monolayer and bilayer system. The combination of DFT calculation and displacement maps reveal that the main discrepancy between defective monolayer and bilayer system is the out-of-plane lattice distortion. The ability for the bilayer sheet to accommodate the buckling and compression caused by line defects can be assigned to the competition between compression in one layer from the loss of S atoms and the interlayer van der Waals force.

4.4 Reference

(1) Gong, Y.; Lin, J.; Wang, X.; Shi, G.; Lei, S.; Lin, Z.; Zou, X.; Ye, G.; Vajtai, R.; Yakobson, B. I.; *et al.* Vertical and in-Plane Heterostructures from WS_2/MoS_2 Monolayers. *Nat. Mater.* **2014**, *13*, 1135–1142.

(2) Plechinger, G.; Nagler, P.; Kraus, J.; Paradiso, N.; Strunk, C.; Schüller, C. and Korn, T. Identification of excitons, trions and biexcitons in single-layer WS_2. *physica status solidi (RRL)-Rapid Research Letters*. **2015**, *9*, 457-461.

(3) Withers, F.; Bointon, T. H.; Hudson, D. C.; Craciun, M. F.; Russo, S. Electron Transport of WS_2 Transistors in a Hexagonal Boron Nitride Dielectric Environment. *Sci. Rep.* **2014**, *4*, 4967.

(4) Sorkin, V.; Pan, H.; Shi, H.; Quek, S. Y.; Zhang, Y. W. Nanoscale Transition Metal Dichalcogenides: Structures, Properties, and Applications. *Crit. Rev. Solid State Mater. Sci.* **2014**, *39*, 319–367.

(5) Komsa, H.-P.; Kotakoski, J.; Kurasch, S.; Lehtinen, O.; Kaiser, U.; Krasheninnikov, A. V. Two-Dimensional Transition Metal Dichalcogenides under Electron Irradiation: Defect Production and Doping. *Phys. Rev. Lett.* **2012**, *109*, 1–5.

(6) Wang, Q. H.; Kalantar-Zadeh, K.; Kis, A.; Coleman, J. N.; Strano, M. S. Electronics and Optoelectronics of Two-Dimensional Transition Metal Dichalcogenides. *Nat. Nanotechnol.* **2012**, *7*, 699–712.

(7) Ma, Y.; Dai, Y.; Guo, M.; Niu, C.; Lu, J.; Huang, B. Electronic and Magnetic Properties of Perfect, Vacancy-Doped, and Nonmetal Adsorbed $MoSe_2$, $MoTe_2$ and WS_2 Monolayers. *Phys. Chem. Chem. Phys.* **2011**, *13*, 15546–15553.

(8) K C, S.; Longo, R. C.; Addou, R.; Wallace, R. M.; Cho, K. Impact of Intrinsic Atomic Defects on the Electronic Structure of MoS_2 Monolayers. *Nanotechnology*

2014, *25*, 375703.

(9) Lin, Y.-C.; Björkman, T.; Komsa, H.-P.; Teng, P.-Y.; Yeh, C.-H.; Huang, F.-S.; Lin, K.-H.; Jadczak, J.; Huang, Y.-S.; Chiu, P.-W.; *et al.* Three-Fold Rotational Defects in Two-Dimensional Transition Metal Dichalcogenides. *Nat. Commun.* **2015**, *6*, 6736.

(10) Zhou, W.; Zou, X.; Najmaei, S.; Liu, Z.; Shi, Y.; Kong, J.; Lou, J.; Ajayan, P. M.; Yakobson, B. I.; Idrobo, J. C. Intrinsic Structural Defects in Monolayer Molybdenum Disulfide. *Nano Lett.* **2013**, *13*, 2615–2622.

(11) Han, Y.; Hu, T.; Li, R.; Zhou, J.; Dong, J. Stabilities and Electronic Properties of Monolayer MoS2 with One or Two Sulfur Line Vacancy Defects. *Phys. Chem. Chem. Phys.* **2015**, *17*, 3813–3819.

(12) Wang, S.; Lee, G.-D.; Lee, S.; Yoon, E.; Warner, J. H. Detailed Atomic Reconstruction of Extended Line Defects in Monolayer MoS_2. *ACS Nano* **2016**, *10*,5419-5430.

(13) Overview of High - Resolution TEM & Scanning TEM High - Resolution EM. *Image (Rochester, N.Y.)*.

(14) Li, H.-M.; Lee, D.-Y.; Choi, M. S.; Qu, D.; Liu, X.; Ra, C.-H.; Yoo, W. J. Metal-Semiconductor Barrier Modulation for High Photoresponse in Transition Metal Dichalcogenide Field Effect Transistors. *Scientific reports*, **2014**, *4*, 4041.

(15) Zhan, Y.; Liu, Z.; Najmaei, S.; Ajayan, P. M.; Lou, J. Large-Area Vapor-Phase Growth and Characterization of MoS2 Atomic Layers on a SiO_2 Substrate. *Small* **2012**, *8*, 966–971.

(16) Lan, C.; Li, C.; Yin, Y.; Liu, Y. Large-Area Synthesis of Monolayer WS 2 and Its Ambient-Sensitive Photo-Detecting Performance. *Nanoscale* **2015**, *7*, 5974–5980.

(17) Plechinger, G.; Schrettenbrunner, F. X.; Eroms, J.; Weiss, D.; Schüller, C.; Korn, T. Low-Temperature Photoluminescence of Oxide-Covered Single-Layer MoS_2. *Phys. Status Solidi - Rapid Res. Lett.* **2012**, *6*, 126–128.

(18) Komsa, H.-P.; Kurasch, S.; Lehtinen, O.; Kaiser, U.; Krasheninnikov, A. V. From Point to Extended Defects in Two-Dimensional MoS_2: Evolution of Atomic Structure under Electron Irradiation. *Phys. Rev. B* **2013**, *88*, 035301.

(19) Lin, J.; Cretu, O.; Zhou, W.; Suenaga, K.; Prasai, D.; Bolotin, K. I.; Cuong, N. T.; Otani, M.; Okada, S.; Lupini, A. R.; *et al.* Flexible Metallic Nanowires with Self-Adaptive Contacts to Semiconducting Transition-Metal Dichalcogenide Monolayers. *Nature nanotechnology*, **2014**, *9*, 436–442.

(20) Ji, Q.; Zhang, Y.; Gao, T.; Zhang, Y.; Ma, D.; Liu, M.; Chen, Y.; Qiao, X.; Tan, P.-

H.; Kan, M.; *et al.* Epitaxial Monolayer MoS_2 on Mica with Novel Photoluminescence. *Nano Lett.* **2013**, *13*, 3870–3877.

(21) Choi, W.; Cho, M. Y.; Konar, A.; Lee, J. H.; Cha, G. B.; Hong, S. C.; Kim, S.; Kim, J.; Jena, D.; Joo, J.; *et al.* High-Detectivity Multilayer MoS2 Phototransistors with Spectral Response from Ultraviolet to Infrared. *Advanced Materials*, **2012**, *24*, 5832–5836.

(22) He, K.; Robertson, A. W.; Fan, Y.; Allen, C. S.; Lin, Y.; Suenaga, K.; Kirkland, A. I.; Warner, J. H. Temperature Dependence of the Reconstruction of Zigzag Edges in Graphene. *ACS nano*, **2015**, *9*, 4786–4795.

(23) Kong, D.; Wang, H.; Cha, J. J.; Pasta, M.; Koski, K. J.; Yao, J.; Cui, Y. Synthesis of MoS_2 and $MoSe_2$ Films with Vertically Aligned Layers, **2013**.

(24) Lee, Y.-H.; Zhang, X.-Q.; Zhang, W.; Chang, M.-T.; Lin, C.-T.; Chang, K.-D.; Yu, Y.-C.; Wang, J. T.-W.; Chang, C.-S.; Li, L.-J.; *et al.* Synthesis of Large-Area MoS_2 Atomic Layers with Chemical Vapor Deposition. *Advanced materials (Deerfield Beach, Fla.)*, **2012**, *24*, 2320–2325.

(25) Wilson, J.; Yoffe, A.D. the transition metal dichalcogenides discussion and tnterpretation of the observed optical, electrical and structural properties. *Adv. Phys.* **1969**, 18, 193-335.

(26) He, J.; Hummer, K.; and Franchini, C. Stacking effects on the electronic and optical properties of bilayer transition metal dichalcogenides MoS 2, MoSe 2, WS 2, and WSe 2. *Physical Review B*, **2014**, 89, 075409.

(27) Lee, J.U.; Kim, K.; Han, S.; Ryu, G.H.; Lee, Z. and Cheong, H. Raman signatures of polytypism in molybdenum disulfide. *ACS nano*, **2016**, 10, 1948-1953.

(28) Suzuki, R.; Sakano, M.; Zhang, Y.J.; Akashi, R.; Morikawa, D.; Harasawa, A.; Yaji, K.; Kuroda, K.; Miyamoto, K.; Okuda, T. and Ishizaka, K. Valley-dependent spin polarization in bulk MoS2 with broken inversion symmetry. *Nature nanotechnology*, **2014**, 9, 611-617.

(29) Liu, L.; Qing, M.; Wang, Y.; Chen, S. Defects in Graphene: Generation, Healing, and Their Effects on the Properties of Graphene: A Review. *J. Mater. Sci. Technol.* **2015**, *31*, 599–606.

(30) Robertson, A. W.; Lee, G. Do; He, K.; Yoon, E.; Kirkland, A. I.; Warner, J. H. The Role of the Bridging Atom in Stabilizing Odd Numbered Graphene Vacancies. *Nano Letters*, **2014**, *14*, 3972–3980

(31) Xie, F.; Lu, H.; Xiu, X.; Chen, D.; Han, P.; Zhang, R.; Zheng, Y. Low Dark Current and Internal Gain Mechanism of GaN MSM Photodetectors Fabricated on Bulk GaN

Substrate. *Solid-State Electronics*, **2011**, *57*, 39–42.

(32) Avouris, P.; Freitag, M.; Perebeinos, V. Carbon-Nanotube Photonics and Optoelectronics. *Nat. Photonics* **2008**, *2*, 341–350.

(33) Tsoukleri, G., Parthenios, J., Papagelis, K., Jalil, R., Ferrari, A.C., Geim, A.K., Novoselov, K.S. and Galiotis, C. Subjecting a graphene monolayer to tension and compression. *small*, **2009**, *5*, 2397-2402.

(34) Lee, C., Wei, X., Kysar, J.W. and Hone, J. Measurement of the elastic properties and intrinsic strength of monolayer graphene. *Science*. **2008**, *321*, 385-388.

(35) Park, S.D., Won Lee, S., Kang, S., Bang, I.C., Kim, J.H., Shin, H.S., Lee, D.W. and Won Lee, D. Effects of nanofluids containing graphene/graphene-oxide nanosheets on critical heat flux. *Applied Physics Letters*. **2010**, *97*, 023103.

(36) Popov, A.M., Lebedeva, I.V., Knizhnik, A.A., Lozovik, Y.E. and Potapkin, B.V. Commensurate-incommensurate phase transition in bilayer graphene. *Physical Review B*. **2011**, *84*, 045404.

(37) Kresse, G.; Furthmüller, J. Efficient Iterative Schemes for *Ab Initio* Total-Energy Calculations Using a Plane-Wave Basis Set. *Phys. Rev. B* **1996**, *54*, 11169–11186.

(38) Blochl, P. E. Projector Augmented-Wave Method. *Phys. Rev. B - Condens. Matter Mater. Phys.* **1994**, *50*, 17953–17979.

(39) Perdew, J. P.; Burke, K.; Ernzerhof, M. Generalized Gradient Approximation Made Simple. *Phys. Rev. Lett.* **1996**, *77*, 3865–3868.

(40) Grimme, S. Semiempirical GGA-Type Density Functional Constructed with a Long-Range Dispersion Correction. *J. Comput. Chem.* **2006**, *27*, 1787−1799.

(41) Monkhorst, H. J.; Pack, J. D. Special Points for Brillouin-Zone Integrations. *Phys. Rev. B* **1976**, *13*, 5188–5192.

Chapter 5

Anti-phase Grain Boundaries in Overlapping MoS2 Secondary Layers

5.1 Introduction

MoS_2 is a semiconducting transition metal dichalcogenide (TMD) with a direct band gap in monolayer form, and indirect in the bulk.[1-4] It offers a band gap in the red visible spectrum and semiconducting properties that expand the applications for 2D materials beyond what graphene can achieve.[5-7] Moreover, large-area monolayer MoS_2 can be synthesized using CVD[8-11], making it a promising candidate for building atomically thin, layered electrical, optical, and photovoltaic devices.[12-16] However, in the production of large-area 2D materials, grain boundaries (GBs) are inevitably produced between randomly oriented crystal domains within a polycrystalline film.[17-19]

Conventional GBs in 3D polycrystalline and nanocrystalline solids influence their mechanical, physical and chemical properties.[20,21] The general effects of GBs on the properties of 2D materials can be assigned to GB dislocation cores, the orientation mismatch between grains and the in-plane and out-of-plane strains introduced.[22] GBs in graphene are usually formed by dislocation cores consisting of pentagon-heptagon ring pairs.[23-25] The presence of GBs can also lead to detrimental effects on some properties of graphene, including reduced electron mobility,[26-29] thermal conductivity,[30] and reduced ultimate mechanical strength.[31] Conversely, GBs in graphene can also be beneficially exploited via controlled GB engineering.[32]

Recently, GBs have been shown to play an important role in reducing the charge carrier mobility in monolayer MoS_2.[33] These extended defects can act as undesired sinks for carriers, increasing their scattering and degrading electrical performance.[34-35] Individual GBs can also strongly affect the photoluminescence of MoS_2 monolayers and alter their in-plane electrical conductivity.[36] All of these effects strongly depend on the GB tilt angles and the local doping and strain introduced by dislocation cores.[36] Therefore, atomic structure analysis of these GBs can facilitate tailoring the properties of MoS_2 via controlled defect engineering. Dislocation cores in monolayer MoS_2 vary in configuration due to the Mo-S bonding characteristics. Structures including 5-7, 4-4, 4-6, 6-8 and 4-8 rings are both theoretically predicted and have been experimentally observed,[36-41] and are dependent on the local Mo/S source concentration as well as the tilt angle.[37] Furthermore, the misorientation angle of the tilt GB ranges from 0^o to 60^o due to the 3-fold symmetry of MoS_2 lattice.[36-41]

The 60^o GBs (also denoted as antiphase boundaries), are of particular interest as they form one-dimensional metallic wires in a semiconducting MoS_2 matrix, [36-39,41,42] and act as conductive channels that have a profound influence on both transport properties and exciton behavior of the monolayers.[37,38,43] Experimental studies have shown that a single 60^o GB can enhance the in-plane electrical conductivity and substantially quench the local photoluminescence.[44] Structural studies at atomic resolution have revealed that these GBs introduce mirror symmetry between two grains, which are connected predominantly through lines of 8- and 4-membered rings.[37] Inversion domains surrounded by these 60^o GBs are formed by annealing TMD monolayers at high temperature.[39] However, the micro-nanoscale distribution of the defects in antiphase GBs and their correlation to the

propagation direction of the GB has yet to be studied in sufficient detail to gain an overall picture of their behavior. Furthermore, the nanoscale-microscale density and distribution of 4- and 8-rings associated with specific directions in the antiphase GB with atomic level detail has not been fully clarified. A few studies have described the growth mechanisms of grain boundaries in MoS_2 and graphene.[39,44-46] Studies of monolayer h-BN have shown that in polycrystalline regions two merging domains can have overlapping interface rather than atomically bonded.[47] Recent work has used ADF-STEM to study the strain maps around mirror twin grain boundaries in $MoSe_2$ bilayers with small grain boundaries and inversion domains, revealing strain relaxation within the local GB area.[48] However, the understanding of the behavior of GBs in monolayer-bilayer stacks on a larger size scale with dimensions extending to micron distances has yet to be explored in detail.

In this study, MoS_2 samples were grown on Si substrates with a 300nm oxide layer using methods previously described.[49] The samples of MoS_2 produced were predominantly monolayer, with occasional small bilayer domains on top of the larger monolayer film. We used annular dark field scanning transmission electron microscopy (ADF-STEM) to probe the atomic structure of antiphase boundaries in both MoS_2 monolayers and bilayers and have studied the 4-ring and 8-ring defects and their relationship with the meandering GB. We have also studied how an antiphase GB propagates from a monolayer to a an overlapping bilayer domain leading to modification of the 2H and 3R bilayer stacking configurations and possible growth processes for differently orientated antiphase boundaries in MoS_2 monolayers are discussed. Density functional theory (DFT) calculations have been used to provide accurate model structures for multislice image

simulations for comparison with the experimental ADF-STEM images in order to understand the impact of van der Waals forces.

5.2 Results and Discussion

5.2.1 Tilt Grain Boundaries in MoS2 Bilayers and Monolayers

Figure 5-1(a) shows a schematic illustration of how two rotated monolayer MoS_2 grains (A and B) can meet to form a tilt grain boundary, as highlighted red in the second panel. A secondary MoS_2 layer (C) nucleates on top of grain B and then continues growing to finally overlap across the top of grain A. This should lead to a GB section where one side has well defined stacking of 2H or 3R, and the other side has a Moiré pattern with the orientation mismatch corresponding to the GB tilt angle. The low magnification ADF-STEM image in **Figure 5-1**(b) shows a region where a secondary MoS_2 domain has grown across a tilt GB in the underlying monolayer. **Figure 5-1**(c) shows the ADF-STEM image of the tilt GB in the monolayer MoS_2, taken from the red boxed area in **Figure 5-1**(a), revealing a 17^o tilt angle, **Figure 5-1**(d). The bright nanoparticles in **Figure 5-1**(b) are Pt and were intentionally deposited to help locate the GB regions easily in ADF-STEM. The ADF-STEM image in **Figure 5-1**(e) shows the overlapping bilayer MoS_2 region, with the green line indicating the GB position. **Figure 5-1**(f), g shows the atomically resolved ADF-STEM images of the GB in the overlapping region, with 3R stacking at the top and Moiré pattern below. This establishes that bilayer domains can grow across GBs that already exist in monolayer MoS_2. We now focus the rest of our study to anti-phase GBs, examining overlapping bilayer regions at antiphase GBs, as well as the nanoscale structure of anti-phase GBs in monolayers.

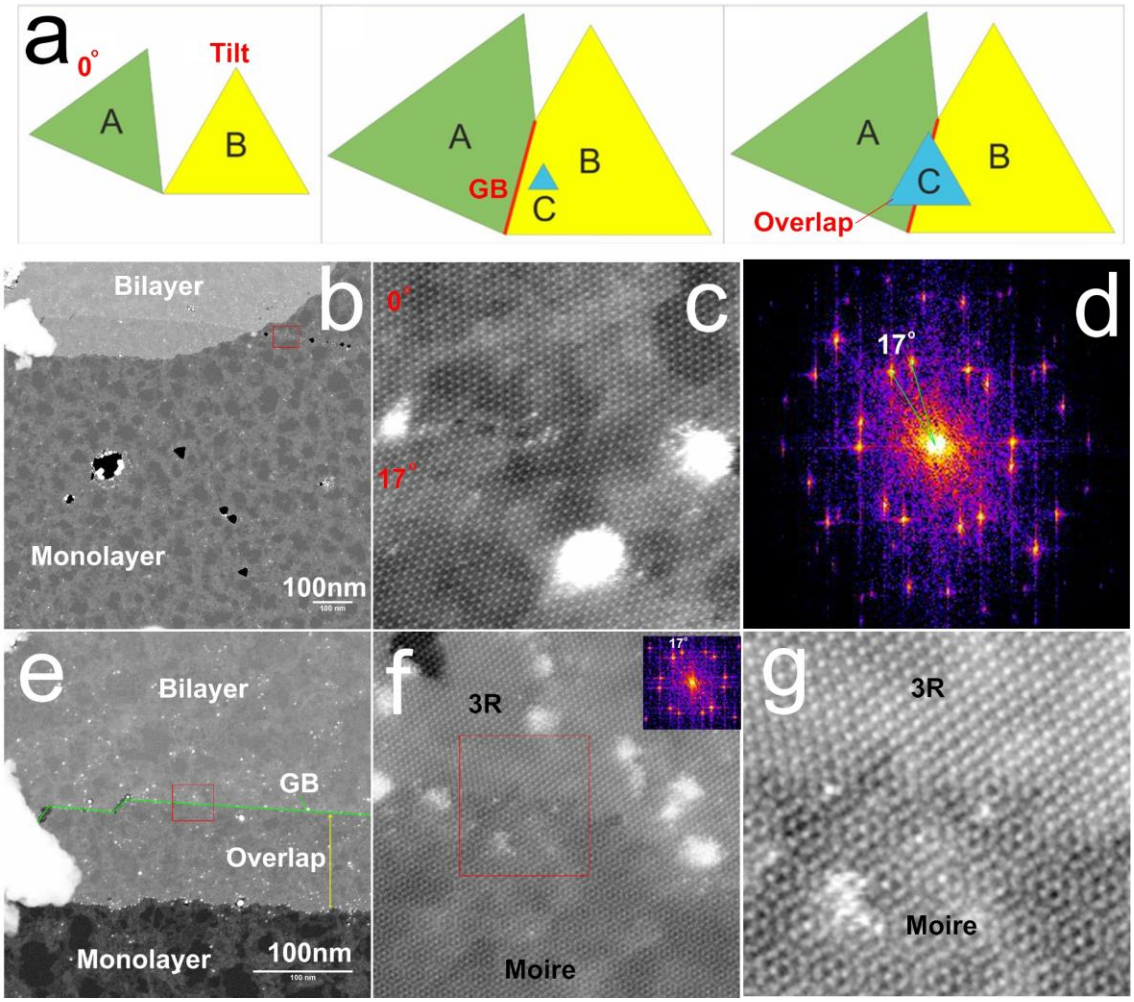

Figure 5-1 (a) Schematic illustrations showing how a secondary MoS_2 layer C grows across the GB between two rotated grains A and B, forming the overlapping bilayer GB region. (b) ADF-STEM image of a tilted GB in a monolayer MoS_2 region with an overlapping bilayer section (c) ADF-STEM image from the red boxed region in (b) showing the tilted GB (17°) in the monolayer MoS_2. (d) FFT from (c) showing the two sets of spots, giving tilt angle of ~17°. (e) ADF-STEM image showing the overlapping GB area from (b), with the GB indicated by the green line. (f) ADF-STEM image from the red box area in (e) showing the overlapping bilayer GB has 3R stacking on its nucleation side (top) and Moiré pattern on the overlapping side (bottom). Inset shows FFT of the image with 17° mismatch within the two layers comprising the Moiré pattern, correlating to the tilt angle. (g) Higher magnification ADF-STEM image from the red box area in (f).

5.2.2 Antiphase Grain Boundaries in MoS_2 Bilayers and Monolayers

The schematic in **Figure 5-2**(a), shows a secondary layer (C) growing on top of grain (B), which meets a 60^o rotated grain (A) forming a grain boundary highlighted in red. Layer (C) approaches the GB during growth (**Figure 5-2**(b)) and finally reaches and grows across the GB (**Figure 5-2**(c)). **Figure 5-2**(d) shows the atomic model of the secondary layer on top of both grain A and B corresponding to **Figure 5-2**(c) which demonstrates that the GB is an antiphase GB, which introduces a 60^o lattice rotation in the monolayer region (**Figure 5-2**(e)). The bilayer region exhibits a 2H-3R stacking sequence with the antiphase boundary at the interface between these. Hence, a stacking sequence change is predicted when the secondary layer grows across the antiphase boundary. The SEM image in **Figure 5-2**(f) shows several secondary layers grown on top of the GB (indicated by yellow dashed circles). A low magnification ADF-STEM image over a large field of view of a region is shown in **Figure 5-2**(g) and (h), showing an antiphase GB in MoS_2 that exists within the larger monolayer that also propagates through regions containing bilayers (zone C and E). The mono-bilayer interface at zone B is magnified in **Figure 5-2**(i). Pt nanoparticles were formed at the GBs during the TEM sample preparation stage to help find the GB location at lower magnification, but do not impact the results of the interlayer stacking structure presented in this work. In the bilayer region, both 2H and 3R stacking sequences are observed with the antiphase GB at the interface. Magnified images at zone A and C are displayed in **Figure 5-2**(j) and (k), respectively. **Figure 5-2**(j) shows octagonal and quadrangular configurations as the structural building blocks of the antiphase boundary in monolayer. The same dislocation cores in bilayer region lead to sharp stacking transition from 2H to 3R in **Figure 5-2**(k). Schematic in **Figure 5-2**(l) demonstrates that the 4-

member ring embedded in the bottom layer of a bilayer system has more significant in-plane contraction, contributing to perfect stacking sequences.

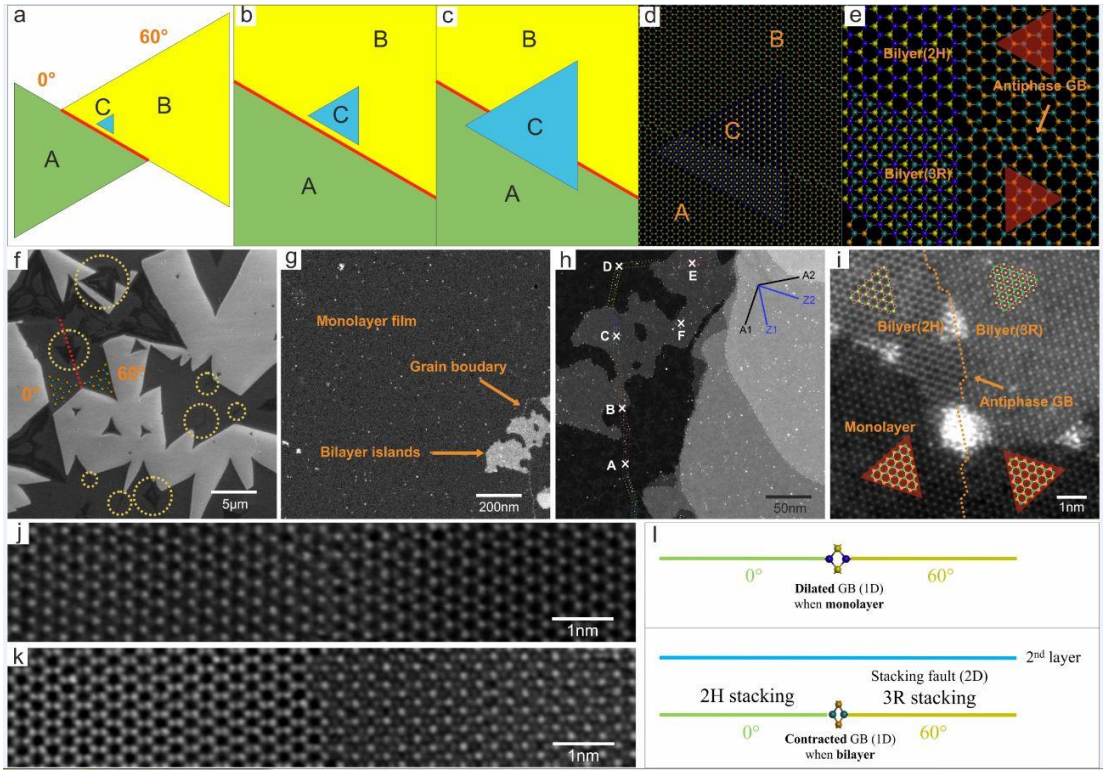

Figure 5-2 (a-c) Schematics showing a secondary MoS_2 layer C growing across the GB between two 60° rotated grains A and B. (d) Atomic model based on the schematic in c. (e) Magnified image of the model showing the antiphase GB in both monolayer and bilayer regions. (f) SEM image of several secondary layers grown on top of GBs, one of which is formed between two 60° rotated grains as indicated. (g) Low magnification ADF-STEM image of continuous monolayer MoS_2 with scattered bilayer islands suspended on holey SiN TEM grid. (h) Intermediate magnification ADF-STEM image showing the propagation of a GB through monolayer and bilayer regions. Zones along the pathway of the GB are marked as A-F. A1, A2, Z1 and Z2 represent armchair and zigzag directions. (i) ADF-STEM image of the GB in both monolayer and bilayer regions. Overlaid lattice diagrams show a 60° rotation for the monolayer grains and different stacking sequences in the bilayers. (j and k) Magnified images of zone A and C, respectively. (l) Schematics showing the contraction difference between the 4-member rings in monolayer and bilayer systems.

5.2.3 Dislocation Cores

Higher magnification ADF-STEM images of Zone A and C with the antiphase boundaries are shown in **Figure 5-3**(a) and (d), respectively. In the monolayer region, the antiphase GB introduces a mirror symmetric domain rotated by 60^{o} with respect to the original lattice and in which the Mo and S sites are swapped. The overlaid atomic structure in **Figure 5-3**(b) indicates that the antiphase domains are joined by edge-sharing 4- and 8-member rings, similar to prior reports on MoS_2 GBs.[36] For the 4-member ring structure, Mo atoms retain 6-fold coordination whereas the S atoms change from 3-fold to 4-fold coordination changing the local stoichiometry from MoS_2 to Mo_4S_6 along the antiphase GB.[36] For the bilayer system, superimposed atomic structures shown in **Figure 5-3**(e) reveal two distinct stacking sequences denoted as 2H and 3R when one layer is overlaid on the other layer including the antiphase GB. The 4-member ring retains its configuration, whereas the 8-membered core appears as 6-4-4 motif in projection due to the 3R stacking sequence on the right-hand side of the boundary. The 4-member rings in both monolayer and bilayer regions are compared in detail in **Figure 5-3**(c) and (f). The S-S and Mo-Mo (monolayer) or (Mo-2S)-(Mo-2S) and (2S-Mo)-Mo (bilayer) column distances were using boxed intensity profiles along the zigzag (A and C) and armchair (B and D) directions. Average values were obtained through multiple measurements from different regions. Due to the lattice distortion along these two directions in our experimental images, the distance measurement was normalized using the pristine MoS_2 lattice parameter as a reference. Within the 4-member ring in the monolayer, the S column distances show similar values (3.13Å vs 3.18Å), whereas a ~24% shrinkage in Mo column distances is observed in the bilayer.

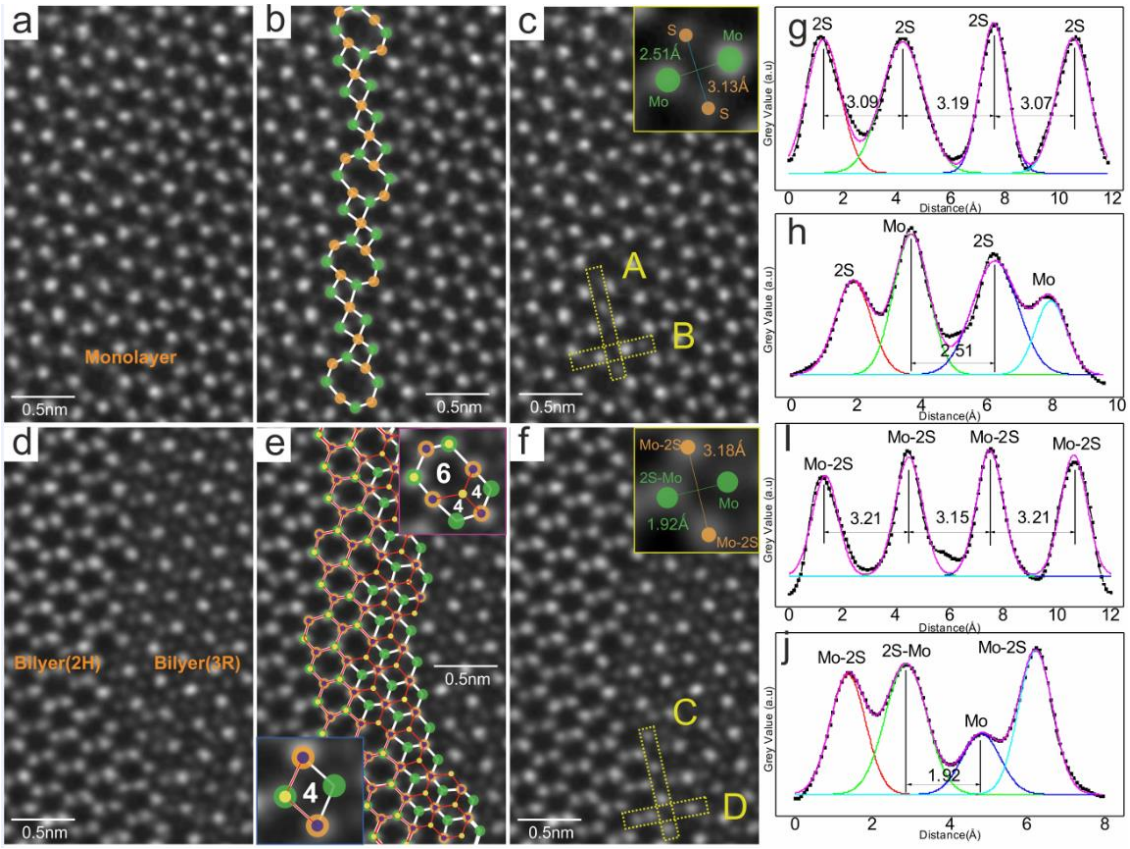

Figure 5-3 (a) ADF-STEM image of an antiphase GB in monolayer MoS_2. (b) The same region with the atomic structure overlaid. (c) The region shown in (a) with an inset showing the column distances in a 4-member ring. (d) ADF-STEM image of an antiphase GB in bilayer MoS_2. (e) The same region with the atomic structure and insets showing the dislocation core structure. The inset shows the column distances in a 4-member ring. (f) The region shown in (e) with an inset showing the column distances in a 4-member ring. (g-j) Boxed line intensity profiles taken along the directions A-D, respectively. Regions indicated by yellow boxed areas in (c) and (f). All distances are normalized by the lattice parameters of pristine MoS_2 monolayers.

To further study the reduction of the Mo-Mo distance in the 4-member rings, DFT calculations of both monolayer and bilayer MoS_2 systems were performed with a 4-4 chain along the zigzag direction as shown in **Figure 5-4**. A multislice image simulation based on the DFT relaxed model of the bilayer system is shown in **Figure 5-4**(d) and compared with our experimental image (**Figure 5-4**(c)). Boxed line intensity profiles were taken along direction 1 and 2 in both simulated and experimental images and show excellent agreement.

These results confirm that the antiphase boundary defects in the bottom layer lead to the atomically sharp transition between 2H and 3R stacking sequences. **Figure 5-4**(a) and (b) compare the antiphase GB structure in the bottom layer of a bilayer and a monolayer, respectively. Insets in **Figure 5-4**(a) and (b) show the bond lengths, indicating negligible difference in S-S column distances but a large discrepancy in Mo-Mo column distances (2.25Å for the monolayer and 1.85Å for the bilayer corresponding to a shrinkage of ~ 22%), which is similar to our experimental observations. Similar phenomena have been reported in monolayer graphene, where a ridge structure was found to separate fcc and hcp domains of a graphene/Ni(111) interface.[50] This bulging of graphene from the Ni(111) substrate facilitates matching of these two stacking sequences in a continuous film without any topological defects. In our case, this local in-plane compression perpendicular to the antiphase GB enables matching of the 2H and 3R stacking without any large out-of-plane distortion.

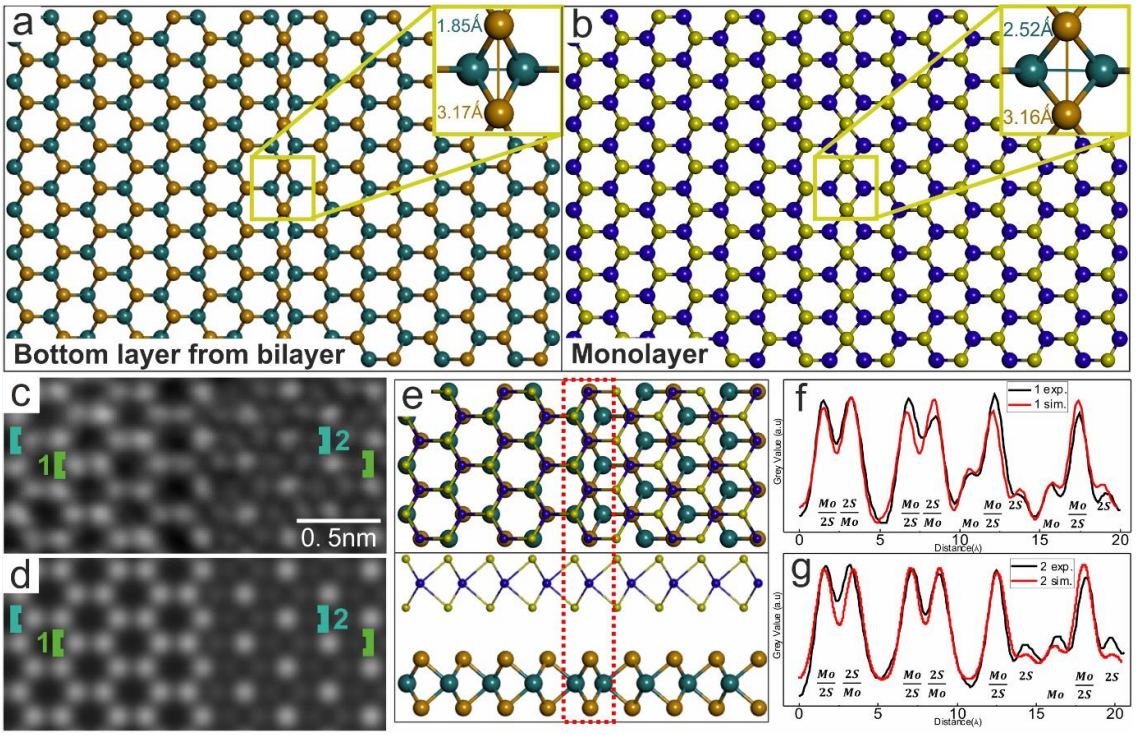

Figure 5-4 DFT-relaxed models of a monolayer antiphase GB (a) extracted from a bilayer and (b) from a pure monolayer. The insets show the column distances in the 4-member rings. (c) ADF-STEM image of a bilayer region with an atomically sharp 2H-3R stacking interface from the antiphase GB in one layer. (d) Multislice image simulation based on the atomic arrangement calculated in (e) from the DFT-relaxed model. The position of 4-member defects is highlighted in red. (f and g) Boxed intensity line profiles taken from (c) experimental and (d) simulated images along the directions marked 1 and 2, respectively. Widths of boxes are indicated by the brackets in (c) and (d).

5.2.4 Propagation Direction

Figure 5-5(a) shows a long section of the antiphase GB in a monolayer with different directions. The propagation direction of each segment is tilted from the zigzag direction by an angle θ, which ranges from 6.4° to 21.5° (as shown in **Figure 5-5**(b-e)). The defects are highlighted in each segment and their numbers are shown in **Figure 5-5**(f). The 4-member rings outnumber the 8-member rings in all segments, and the ratio (N8/N4) is as low as 0.33 for **Figure 5-5**(b) and as high as 0.51 in **Figure 5-5**(e). The ratio (N8/N4) as a function

of θ (**Figure 5-5**(g)) shows increased octagonal ring density with increasing θ. At the atomic level, 4-member rings provide GB propagation along the zigzag direction, whereas the 8-member rings provide arm-chair propagation, and the combination of these determines the arbitrary direction propagation. The ratio would equal 0 and 1 respectively if the GB propagated along the zigzag ($\theta = 0^{o}$) and the armchair direction ($\theta = 30^{o}$), respectively. Antiphase GBs act as 1D metallic wires embedded in the semiconducting MoS_2 matrix and kinks induce significant changes to the electronic behavior of a GB.[37] Alternatively, an antiphase GB has been reported to be n-doped due to the local Mo-rich environment arising from 4-member rings.[36,37] The n-doped GB shows significant PL quenching due to an increased electron density,[36] suggesting that lower PL intensity quenching could be achieved with a higher 8-member ring density.

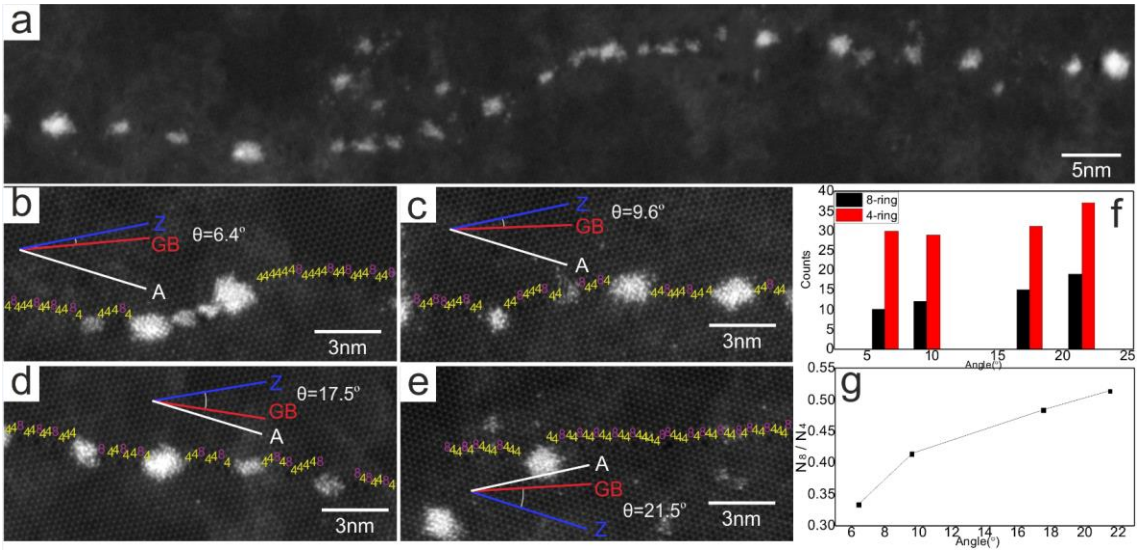

Figure 5-5 (a) ADF-STEM image of an antiphase GB in bilayer MoS_2, tracked by the Pt cluster decoration. Segments deviate from zigzag directions by an angle, θ between (b) 6.4^{o}, (c) 9.6^{o}, (d) 17.5^{o}, (e) 21.5^{o}. Specific directions (Z for zigzag, GB for propagation and A for armchair) are indicated. (f) Histogram of 4- and 8-member rings varying with θ. (g) ratio of 8-ring/4-ring in b-e as a function of θ.

5.2.5 Growth Mechanism

We now discuss a possible growth process that could lead to antiphase GBs between multiple grains. **Figure 5-6**(a) shows an SEM image of MoS_2 grains with irregular shapes. The morphological irregularity is attributed to various factors including: growth temperature, presence of impurities, local Mo/S source concentration fluctuation and substrate effects. Two groups of grains, each of which contains three grains, are of particular interest. In each group, two grains sharing a common orientation exhibit a 60^o rotation with respect to a third grain. Three grains can merge (as indicated in **Figure 5-6**) and a meandering antiphase GB forms at a certain stage of growth. These observations are consistent with the GB formation mechanism described by Huang et al.[51] Initially, a group of grains with S-terminated zigzag edges nucleate on a bare substrate (**Figure 5-6**(b)). The edges of each grain subsequently grow at uneven speeds and hence the grains show irregular morphologies (**Figure 5-6**(c)). Two grains with the same orientation then merge (**Figure 5-6**(d)) and continue to grow until they contact the 60^o rotated grain (**Figure 5-6**(e)). As shown in **Figure 5-6**(f), this mechanism gives rise to two segments of an antiphase GB with an angle of $\sim 95^o$ between the grains and a special 8-member ring at the apex that facilitates the large directional change of the antiphase GB.

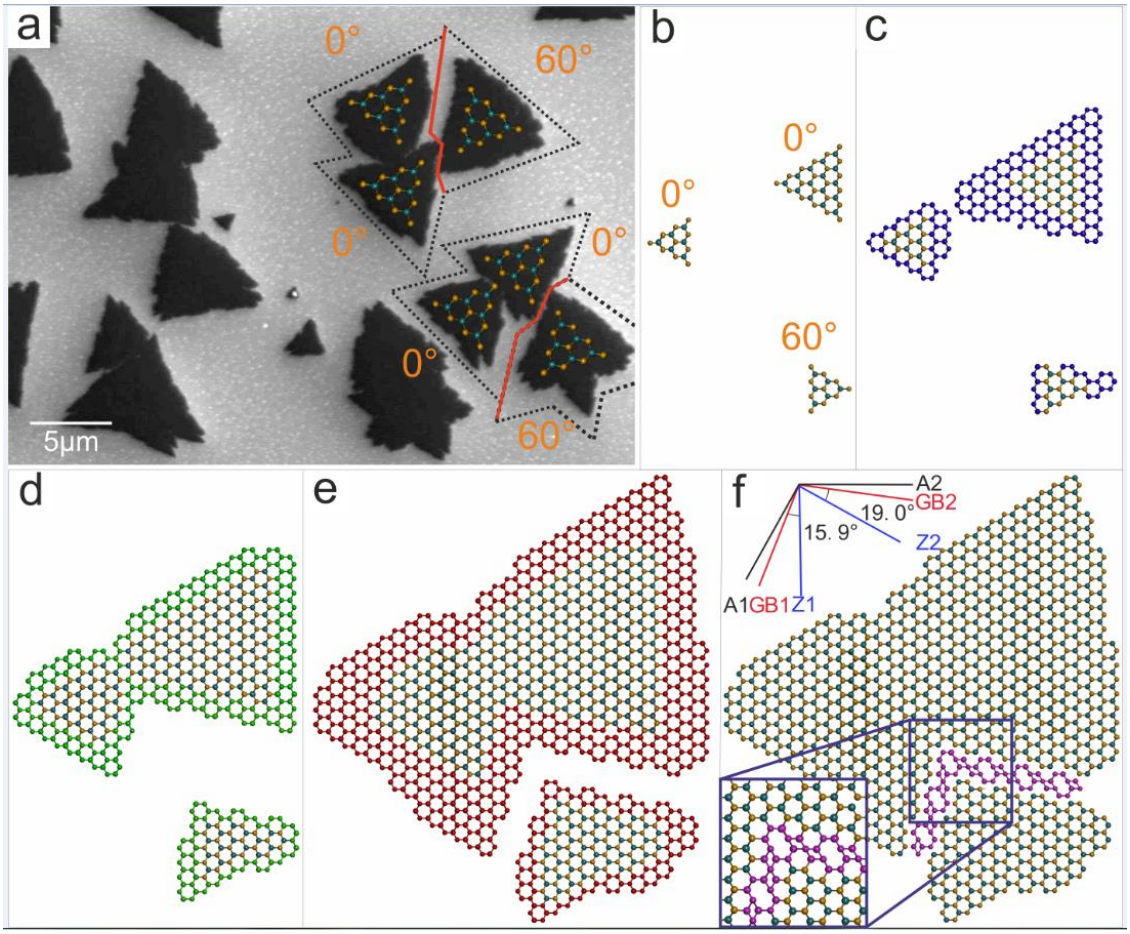

Figure 5-6 (a) SEM image in SE showing the irregular shape of MoS_2 domains grown on a Si/SiO_2 wafer by CVD. Grains are superimposed with atomic structures to indicate orientation differences. Angles shown are relative to the reference domain in each group. The meandering antiphase GBs formed by merging grains are highlighted by red. (b-f) Schematic atomic models illustrating the growth process of two antiphase GBs with a turning angle of ~95° which are connected by one 8-member ring at the apex.

5.2.6 Swap of Stacking Sequences in MoS2 Bilayers

Figure 5-7(a) shows the top side part of **Figure 5-2**. **Figure 5-7**(b) shows magnified zone D where a large directional change of the antiphase GB occurs, similar to that proposed in figure 6. At this location two antiphase GB segments (GB1 and GB2) meet with a rotation angle of ~104°. Both segments show a similar tilt angle (21.5° and 22.5°) from their

respective zigzag directions, indicating a negligible difference in the 8-member ring density. The meeting point of the antiphase GB is examined at the atomic-level in **Figure 5-7**(c) and (d), qualitatively matching the structure in **Figure 5-7**(f). **Figure 5-7**(e-g) compare the 8-member ring at the turning point to those in the other sections of the GB. Mo atoms in the alternative positions (Mo1 and Mo3 or Mo2 and Mo4) connect 4-member rings along the same zigzag directions, whereas neighboring Mo atoms (Mo1 and Mo4) at the meeting point facilitate directional switching from Z1 to Z2. **Figure 5-7**(h-j) show how the change in angle of the antiphase GB influences the same bilayer domain by examining zones C, F and E. Zone C, which is associated with GB1 direction has the 2H:3R change (**Figure 5-7**(h)), and the 3R stacking is maintained all the way to zone F (**Figure 5-7**(i)), but at zone E (associated with GB2 direction), we see a reversal of the stacking from 3R:2H (**Figure 5-7**(j)). However, **Figure 5-7**(k) shows a region at the zone G, within the bilayer where the antiphase GB has another sharp turn and this induces local 2H-3R-2H changes. The 3R section in the middle, **Figure 5-7**(k), has blurred lattice contrast, indicating poor lattice registration within the 3R stacking, which is due to the competing strain effects of the GBs in different directions.

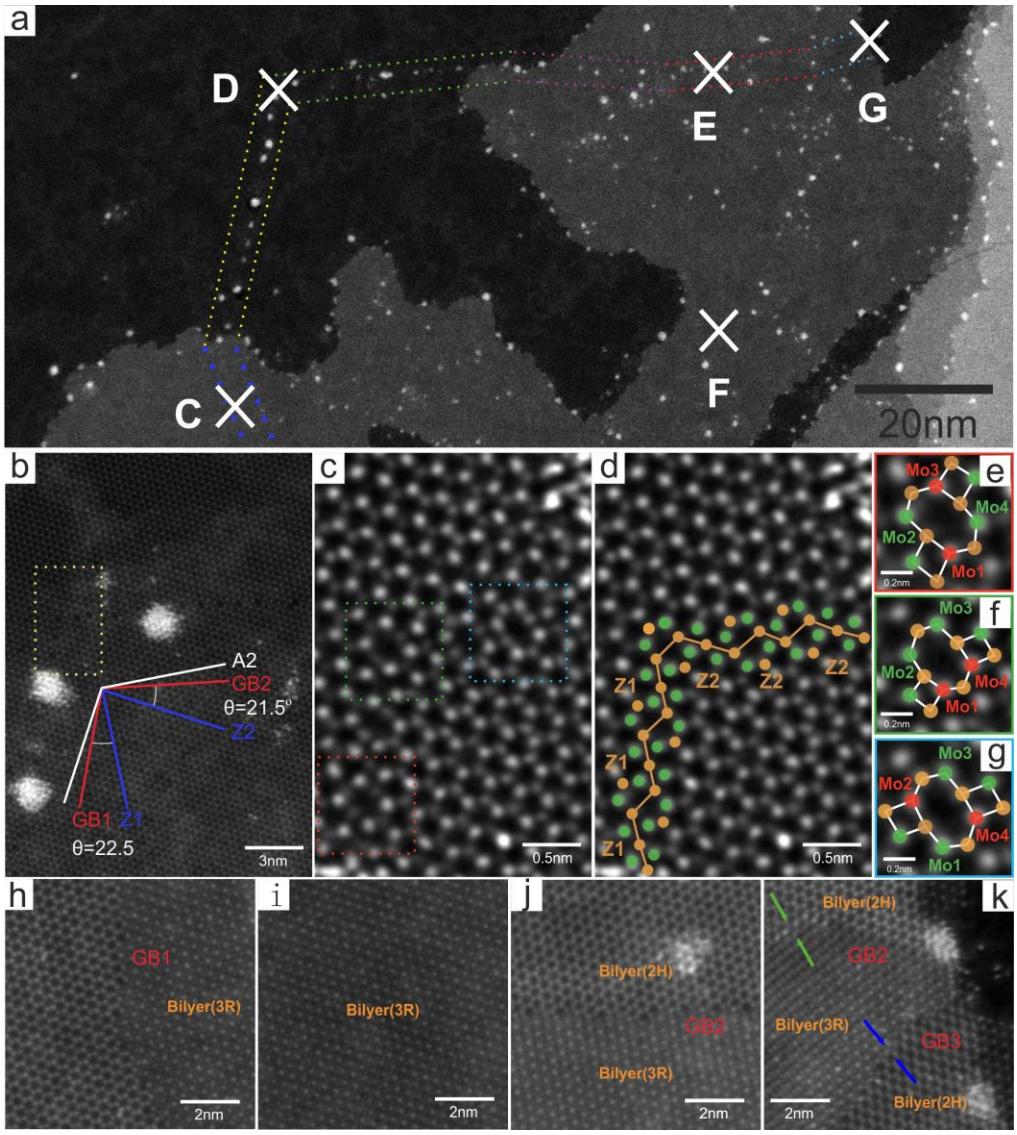

Figure 5-7 (a) Low magnification image showing the top-side part in figure 2h. (b) ADF-STEM image showing large turning angle for an antiphase GB. Armchair (A1 and A2), zigzag (Z1 and Z2) and propagation directions (GB1 and GB2) are marked in white, blue and red, respectively. (c) ADF-STEM image showing the apex of the two antiphase GB directions. (d) Schematic illustration of the pathway of the antiphase GB superimposed on the ADF-STEM image in (b). (e-g) 8-member defects that enable GB kinks, superimposed with atomic structures. Images are taken from the boxed areas in (e) the left-hand side (f) the center and (g) the right-hand side of the apex of two antiphase GBs. (h-j) ADF-STEM images showing how the large GB turning angle impacts the bilayer 2H and 3R stacking from zones C, F and E. (k) Region at the end of zone E, where the GB takes another large turn and causes local stacking changes of 2H and 3R. Contraction directions described in the text are indicated by green and blue arrows.

5.3 Conclusion

We have demonstrated that the propagation of an antiphase GB from a MoS_2 monolayer into a bilayer region causes atomically sharp stacking changes from 2H-3R, which is reversed upon a second antiphase GB crossing. Antiphase GBs within the monolayer section can propagate with arbitrary direction by the combination of 4-fold and 8-fold rings, where the ratio depends upon GB angle relative to the zig-zag lattice direction of MoS_2. Large turning angles of the antiphase GB were also observed and are mediated by a specific 8-member ring defect that has different positions of the attaching 4-member rings. Antiphase GBs in the MoS_2 bilayer region exhibit larger lattice shrinkage along the Mo-Mo direction compared to the pure monolayers which is confirmed by DFT calculations. Overall, our data show that there is an energetic competition between a perfect 2H-3R stacking interface and buckling, in which interlayer van der Waals forces cause a reduction in buckling in MoS_2 due to antiphase GBs in order to achieve atomically sharp 2H-3R stacking sequences in the bilayer. These results provide a detailed characterization of antiphase GBs in monolayer MoS_2 and will help guide the understanding of their structure-property correlation.

5.4 Reference

(1) Gong, Y.; Lin, J.; Wang, X.; Shi, G.; Lei, S.; Lin, Z.; Zou, X.; Ye, G.; Vajtai, R.; Yakobson, B. I.; *et al.* Vertical and In-plane Heterostructures from WS_2/MoS_2 Monolayers. *Nat. Mater.* **2014**, *13*, 1135-1142.

(2) Plechinger, G.; Nagler, P.; Kraus, J.; Paradiso, N.; Strunk, C.; Schüller, C. and Korn, T. Identification of Excitons, Trions and Biexcitons in Single-layer WS_2. *Physica status solidi (RRL)-Rapid Research Letters*. **2015**, *9*, 457-461.

(3) Withers, F.; Bointon, T. H.; Hudson, D. C.; Craciun, M. F.; Russo, S. Electron Transport of WS_2 Transistors in a Hexagonal Boron Nitride Dielectric Environment. *Sci. Rep.* **2014**, *4*, 4967.

(4) Sorkin, V.; Pan, H.; Shi, H.; Quek, S. Y.; Zhang, Y. W. Nanoscale Transition Metal Dichalcogenides: Structures, Properties, and Applications. *Crit. Rev. Solid State Mater. Sci.* **2014**, *39*, 319-367.

(5) Komsa, H.-P.; Kotakoski, J.; Kurasch, S.; Lehtinen, O.; Kaiser, U.; Krasheninnikov, A. V. Two-Dimensional Transition Metal Dichalcogenides under Electron Irradiation: Defect Production and Doping. *Phys. Rev. Letts.* **2012**, *109*, 1-5.

(6) Wang, Q. H.; Kalantar-Zadeh, K.; Kis, A.; Coleman, J. N.; Strano, M. S. Electronics and Optoelectronics of Two-Dimensional Transition Metal Dichalcogenides. *Nat. Nanotechnol.* **2012**, *7*, 699-712.

(7) Ma, Y.; Dai, Y.; Guo, M.; Niu, C.; Lu, J.; Huang, B. Electronic and Magnetic Properties of Perfect, Vacancy-Doped, and Nonmetal Adsorbed $MoSe_2$, $MoTe_2$ and WS_2 Monolayers. *Phys. Chem. Chem. Phys.* **2011**, *13*, 15546-15553.

(8) Lee, Y.H.; Zhang, X.Q.; Zhang, W.; Chang, M.T.; Lin, C.T.; Chang, K.D.; Yu, Y.C.; Wang, J.T.W.; Chang, C.S.; Li, L.J. and Lin, T.W. Synthesis of Large-area MoS_2 Atomic Layers with Chemical Vapor Deposition. *Advanced Materials*. **2012**, *24(17)*, 2320-2325.

(9) Zhan, Y.; Liu, Z.; Najmaei, S.; Ajayan, P. M.; Lou, J. Large-area Vapor-phase Growth and Characterization of MoS_2 Atomic Aayers on a SiO_2 Substrate. *Small.* **2012**, *8(7)*, 966-971

(10) Liu, K.K.; Zhang, W.; Lee, Y.H.; Lin, Y.C.; Chang, M.T.; Su, C.Y.; Chang, C.S.; Li, H.; Shi, Y.; Zhang, H.; Lai, C.S. Growth of Large-area and Highly Crystalline MoS_2 Thin Layers on Insulating Substrates. *Nano Letts*. **2012**, *12(3)*, 1538-1544.

(11) Shi, Y.; Zhou, W.; Lu, A.Y.; Fang, W.; Lee, Y.H.; Hsu, A.L.; Kim, S.M.; Kim, K.K.; Yang, H.Y.; Li, L.J.; J.C. Van der Waals Epitaxy of MoS_2 Layers Using Graphene as Growth Templates. *Nano Letts*. **2012**, *12(6)*, 2784-2791

(12) Radisavljevic, B.; Radenovic, A.; Brivio, J.; Giacometti, I.V.; Kis, A. Single-layer MoS_2 Transistors. *Nat. Nanotechnol*. **2011**, *6(3)*, 147-150.

(13) Dean, C.R.; Young, A.F.; Meric, I.; Lee, C.; Wang, L.; Sorgenfrei, S.; Watanabe, K.; Taniguchi, T.; Kim, P.; Shepard, K.L.; Hone, J. Boron Nitride Substrates for high-quality Graphene Electronics. *Nat. Nanotechnol*. **2010**, *5(10)*, 722-726.

(14) Britnell, L.; Gorbachev, R.V.; Jalil, R.; Belle, B.D.; Schedin, F.; Mishchenko, A.; Georgiou, T.; Katsnelson, M.I.; Eaves, L.; Morozov, S.V.; Peres, N.M.R. Field-

effect Tunneling Transistor based on Vertical Graphene Heterostructures. *Science*. **2012**, *335(6071)*, 947-950.

(15) Mak, K.F.; Lee, C.; Hone, J.; Shan, J.; Heinz, T.F. Atomically Thin MoS_2: A New Direct-gap Semiconductor. *Phys. Rev. Letts*. **2010**, *105(13)*, 136805.

(16) Yin, Z.; Li, H.; Li, H.; Jiang, L.; Shi, Y.; Sun, Y.; Lu, G.; Zhang, Q.; Chen, X.; Zhang, H. Single-Layer MoS_2 Phototransistors. *ACS Nano*. **2011**, *6(1)*, 74-80.

(17) Yu, Q.; Jauregui, L.A.; Wu, W.; Colby, R.; Tian, J.; Su, Z.; Cao, H.; Liu, Z.; Pandey, D.; Wei, D.; Chung, T.F. Control and Characterization of Individual Grains and Grain Boundaries in Graphene Grown by Chemical Vapour Deposition. *Nat. Mater.* **2011**, *10(6)*, 443-449.

(18) Wood, J.D.; Schmucker, S.W.; Lyons, A.S.; Pop, E.; Lyding, J.W. Effects of Polycrystalline Cu Substrate on Graphene Growth by Chemical Vapor Deposition. *Nano Letts*. **2011**, *11(11)*, 4547-4554.

(19) Biró, L.P; Lambin, P. Grain Boundaries in Graphene Grown by Chemical Vapor Deposition. *New J. Phys*. **2013**, *15(3)*, 035024.

(20) Hilgenkamp, H.; Mannhart, J. Grain Boundaries in High-T Superconductors. *Rev Mod. Phys*. **2002**, *74(2)*, 485.

(21) Pande, C.S.; Cooper, K.P. Nanomechanics of Hall–Petch Relationship in Nanocrystalline Materials. *Prog. Mat. Sci*. **2009**, *54(6)*, 689-706.

(22) Ovidko, I. Review on Grain Boundaries in Graphene. Curved Poly-and nanocrystalline Graphene Structures as New Carbon Allotropes. *Rev. Adv. Mater. Sci.* **2012**, *30(3)*, 201-224.

(23) Zhao, L.; Rim, K.T.; Zhou, H.; He, R.; Heinz, T.F.; Pinczuk, A.; Flynn, G.W.; Pasupathy, A.N. Influence of Copper Crystal Surface on the CVD Growth of Large Area Monolayer Graphene. *Solid State Comm.* **2011**, *151(7)*, 509-513.

(24) Malola, S.; Häkkinen, H.; Koskinen, P. Structural, Chemical, and Dynamical Trends in Graphene Grain Boundaries. *Phys. Rev. B.* **2010**, *81(16)*, 165447.

(25) Cockayne, E.; Rutter, G.M.; Guisinger, N.P.; Crain, J.N.; First, P.N.; Stroscio, J.A. Grain Boundary Loops in Graphene. *Phys. Rev. B.* **2011**, *83(19)*, 195425.

(26) Kim, K. S.; Zhao, Y.; Jang, H.; Lee, S. Y.; Kim, J. M.; Kim, K. S.; Ahn, J. H.; Kim, P.; Choi, J. Y.; Hong, B. H. Large-Scale Pattern Growth of Graphene Films for Stretchable Transparent Electrodes. *Nature* **2009**, *457*, 706-710.

(27) Reina, A.; Jia, X.; Ho, J.; Nezich, D.; Son, H.; Bulovic, V.; Dresselhaus, M. S.; Kong, J. Large Area, Few-Layer Graphene Films on Arbitrary Substrates by Chemical Vapor Deposition. *Nano Letts.* **2009**, *9*, 30-35.

(28) Li, X.; Cai, W.; An, J.; Kim, S.; Nah, J.; Yang, D.; Piner, R.; Velamakanni, A.; Jung, I.; Tutuc, E.; et al. Large-AreaSynthesis of High-Quality and Uniform Graphene Films on Copper Foils. *Science* **2009**, *324*, 1312-1314.

(29) Bae, S.; Kim, H. K.; Lee, Y.; Xu, X.; Park, J. S.; Zheng, Y.; Balakrishnan, J.; Lei, T.; Kim, H. R.; Song, Y. I.; et al. Roll-to-Roll Production of 30-Inch Graphene Films for Transparent Electrodes. *Nat. Nanotechnol*. **2010**, *5*, 574-578.

(30) Cai, W.; Moore, A. L.; Zhu, Y.; Li, X.; Chen, S.; Shi, L.; Ruoff, R. S. Thermal Transport in Suspended and Supported Monolayer Graphene Grown by Chemical Vapor Deposition. *Nano Letts.* **2010**, *10*, 1645-1651.

(31) Grantab, R.; Shenoy, V. B.; Ruoff, R. S. Anomalous Strength Characteristics of Tilt Grain Boundaries in Graphene. *Science* **2010**, *330*, 946-948.

(32) Yazyev, O. V.; Louie, S. G. Electronic Transport in Polycrystalline Graphene. *Nat. Mater*. **2010**, *9*, 806-809.

(33) Novoselov, K. S.; Jiang, D.; Schedin, F.; Booth, T. J.; Khotkevich, V. V.; Morozov, S. V.; Geim, A. K. Two-Dimensional Atomic Crystals. *Proc. Natl. Acad. Sci. U.S.A.* **2005**,*102*, 10451-10453.

(34) Enyashin, A. N.; Bar-Sadan, M.; Houben, L.; Seifert, G. Line Defects in Molybdenum Disulfide Layers. *J. Phys. Chem. C* **2013**, *117*, 10842-10848.

(35) Qiu, H.; Xu, T.; Wang, Z.; Ren, W.; Nan, H.; Ni, Z.; Chen, Q.; Yuan, S.; Miao, F.; Song, F.; et al. Hopping Transport Through Defect-Induced Localized States in Molybdenum Disulphide. *Nat. Commun.* **2013**, *4*, 2442.

(36) Van Der Zande, A.M.; Huang, P.Y.; Chenet, D.A.; Berkelbach, T.C.; You, Y.; Lee, G.H.; Heinz, T.F.; Reichman, D.R.; Muller, D.A.; Hone, J.C. Grains and Grain boundaries in Highly Crystalline Monolayer Molybdenum Disulphide. *Nat. Mater.* **2013**, *12(6)*, 554-561.

(37) Zhou, W.; Zou, X.; Najmaei, S.; Liu, Z.; Shi, Y.; Kong, J.; Lou, J.; Ajayan, P.M.; Yakobson, B.I; Idrobo, J.C. Intrinsic Structural Defects in Monolayer Molybdenum Disulfide. *Nano Letts*. **2013**, *13(6)*, 2615-2622.

(38) Zou, X.; Liu, Y.; Yakobson, B.I. Predicting Dislocations and Grain Boundaries in Two-Dimensional Metal-Disulfides from the First Principles. *Nano Letts.* **2012**, *13(1)*, 253-258.

(39) Lin, J.; Pantelides, S.T.; Zhou, W. Vacancy-Induced Formation and Growth of Inversion Domains in Transition-Metal Dichalcogenide Monolayer. *ACS Nano*. **2015**, *9(5)*, 5189-5197.

(40) Azizi, A.; Zou, X.; Ercius, P.; Zhang, Z.; Elías, A.L.; Perea-López, N.; Stone, G.; Terrones, M.; Yakobson, B.I.; Alem, N. Dislocation Motion and Grain Boundary Migration in Two-Dimensional Tungsten Disulphide. *Nat. Commun.* **2014**, *5*, 4867.

(41) Ly, T.H.; Perello, D.J.; Zhao, J.; Deng, Q.; Kim, H.; Han, G.H.; Chae, S.H.; Jeong, H.Y.; Lee, Y.H. Misorientation-Angle-Dependent *Nat. Commun.* **2016**, *7*, 10426.

(42) Liu, X.; Balla, I.; Bergeron, H.; Hersam, M.C. Point Defects and Grain Boundaries in Rotationally Commensurate MoS_2 on Epitaxial Graphene. *The J. Phys. Chem. C*. **2016,** *120(37),* 20798-20805.

(43) Najmaei, S.; Liu, Z.; Zhou, W.; Zou, X.; Shi, G.; Lei, S.; Yakobson, B. I.; Idrobo, J.-C.; Ajayan, P. M.; Lou, J. Vapour Phase Growth and Grain Boundary Structure of Molybdenum Disulphide Atomic Layers. *Nat. Mater.* **2013**, *12*, 754-759.

(44) Najmaei, S.; Amani, M.; Chin, M. L.; Liu, Z.; Birdwell, A. G.; O'Regan, T. P.; Ajayan, P. M.; Dubey, M.; Lou, J. Electrical Transport Properties of Polycrystalline Monolayer Molybdenum Disulfide. *ACS Nano* **2014**, *8*, 7930-7937.

(45) Guo, W.; Wu, B.; Li, Y.; Wang, L.; Chen, J.; Chen, B.; Zhang, Z.; Peng, L.; Wang, S.; Liu, Y. Governing Rule for Dynamic Formation of Grain Boundaries in Grown Graphene. *ACS Nano*. **2015**, *9(6)*, 5792-5798.

(46) Elibol, K.; Susi, T.; Maria, O.; Bayer, B.C.; Pennycook, T.J.; McEvoy, N.; Duesberg, G.S.; Meyer, J.C.; Kotakoski, J. Grain Boundary-Mediated Nanopores in Molybdenum Fisulfide Grown by Chemical Vapor Deposition. *Nanoscale.* **2017**, *9*, 1591-1598.

(47) Bayer, B. C.; Caneva, S.; Pennycook, T. J.; Kotakoski, J.; Mangler, C.; Hofmann, S.; Meyer, J. C.; Introducing Overlapping Grain Boundaries in Chemical Vapour Deposited Hexagonal Boron Nitride Monolayer Films, *ACS Nano*, **2017**, 11, 4521-4527

(48) Zhao, X.; Ding, Z.; Chen, J.; Dan, J.; Poh, S. M.; Fu, W.; Pennycook, S. J.; Zhou, W.; Loh, K. P.; Strain Modulation by van der Waals Coupling in Bilayer Transition Metal Dichalcogenide, *ACS Nano*, **2018**, 12, 1940-1948.

(49) Zhou, S.; Wang, S.; Li, H.; Xu, W.; Gong, C.; Grossman, J.C.; Warner, J.H. Atomic Structure and Dynamics of Defects in 2D MoS_2 Bilayers. *ACS Omega*. **2017**, *2(7)*, 3315-3324.

(50) Lahiri, J.; Lin, Y.; Bozkurt, P.; Oleynik, I.I.; Batzill, M. An Extended Defect in Graphene as a Metallic Wire. *Nat. Nanotechnol*. **2010**, *5*, 326-329.

(51) Huang, P.Y.; Ruiz-Vargas, C.S.; van der Zande, A.M.; Whitney, W.S.; Levendorf, M.P.; Kevek, J.W.; Garg, S.; Alden, J.S.; Hustedt, C.J.; Zhu, Y.; Park, J. Grains and Grain Boundaries in Single-Layer Graphene Atomic Patchwork Quilts. *Nature.* **2011**, *469(7330)*, 389-392.

(52) Hosokawa, F.; Sawada, H.; Kondo, Y.; Takayanagi, K.; Suenaga, K. Development of Cs and Cc Correctors for Transmission Electron Microscopy. Microscopy 2013, 62, 23-41.

(53) Kresse, G.; Furthmüller, J. Efficient Iterative Schemes for ab initio Total-Energy Calculations Using a Plane-Wave Basis set. Phys. Rev. B. 1996, 54, 11169-11186.

(54) Perdew, J. P.; Burke, K.; Ernzerhof, M. Generalized Gradient Approximation Made Simple. *Phys. Rev. Lett.* **1996**, *77*, 3865-3868.

(55) Blöchl, P. E. Projector Augmented-wave Method. *Phys. Rev. B.* **1994**, *50*, 17953-17979.

(56) Monkhorst, H. J.; Pack, J. D. Special Points for Brillouin-Zone Integrations. *Phys. Rev. B.* **1976**, *13*, 5188-5192.

Chapter 6

Surface Ripples in Transition Metal Dichalcogenide Bilayers

6.1 Introduction

Layered materials, such as graphite and transition metal dichalcogenides (TMDs) are stacked through weak interlayer van der Waals interactions[1]. For 2D TMDs such as WS_2 and MoS_2, their bilayer structures offer an extra layer degree of freedom, which introduces performance enhancements compared to the monolayer counterpart[2-4]. For example, few layer MoS_2 show higher carrier mobility and perform better in gas sensing[5-6]. Interaction between MoS_2 or WS_2 layers as well as the specific stacking arrangement can significantly modify their electrical, optical and vibrational properties[3,7-9]. 2H stacking and 3R stacking are two predominantly existing stacking forms[3,10]. Previous studies have shown that these differently stacked MoS_2 have distinct properties in terms of Raman and RL[11-13]. The stacking alters the band gap, which can be engineered by rotating or sliding the layers[14,15]. Therefore, the control of TMD bilayer stacking is significant when considering their future device applications[16].

In previous studies of layered materials, evidence for the coexistence of domains with different stacking orders were reported[17-20]. For example, domains with mirrored AB and AC stacking were synthesized in BLG[18]. An atomically sharp interface, which was denoted as an antiphase grain boundary, was observed in between of 2H and 3R stacked MoS_2 bilayer regions[17]. However, the AB and AC stacking boundary in graphene bilayer is not atomically sharp but instead nanometer-wide strained channels in the form of ripples[18],

which have been intensively observed and studied as a strain relaxation mechanism in graphene and TMD monolayers[21-25]. These corrugations are formed through thermal vibrations, edge instabilities, thermodynamically unstable interactions, strain, thermal contraction and pre-strained substrate-relaxation[26]. The studies of rippling in 2D materials were used to modify their electronic, mechanical, optical, surface and chemical properties of layered crystals[27-37]. For the TMD bilayers, surface ripples in MoS_2 multilayers, denoted as ripplocations, have been observed[23]. However, detailed atomic structure of this surface ripple between perfect stacking orders has not been investigated. It is not known about the relationship between the morphology of the ripples in the bilayers and the corresponding lattice registration. One more unsolved issue is how these ripples behave under high temperature and prolonged beam irradiation. As an important step to reveal the contribution of these unique transition stacking boundaries to the properties of TMD bilayers, it is necessary to visualize their morphologies, to identify and analyze their atomic structures, as well as to study their dynamics.

In this study, MoS_2 and WS_2 samples were grown on Si substrates with a 300nm oxide layer and later transferred onto an *in-situ* heating holder using methods previously described[17,38]. The samples of MoS_2 produced were predominantly monolayers, with occasional small bilayer domains on top of the larger monolayer film. Upon heating, we used annular dark field scanning transmission electron microscopy (ADF-STEM) to systematically analyze the morphology of the stacking boundaries in MoS_2 and WS_2 bilayers, from micrometer scale down to atomic level. The experimental results together with atomic models and corresponding simulations have evidenced the transition stacking boundaries as surface ripples. We also studied the reversibility of these ripples under

heating and cooling cycles and their stability under prolonged beam irradiation, providing a full view of these corrugations in TMD bilayers.

6.2 Results and Discussion

6.2.1 Morphology of Surface Ripples in bilayers

Figure 6-1(a) displays an as-grown sample of MoS_2 monolayers, with scattered secondary layers grown on top as indicated. The sample was transferred onto *in-situ* heating chips for STEM observation which contains Si_3N_4 thin film with slits cut in as shown in **Figure 6-1**(b). The slits were covered by transferred MoS_2 bilayers. A closer observation of the suspended region is displayed in **Figure 6-1**(c) and (d), showing the uniform and perfect lattice registration of two MoS_2 bilayers. The boxed regions are further zoomed in in **Figure 6-1**(e) and (f), suggesting the stacking sequences are 2H and 3R, respectively. **Figure 6-1**(g) and (h) show corresponding atomic models from both top and bottom views of 2H and 3R stacking sequences, respectively. For MoS_2 monolayers or bilayers, their flat and uniform morphologies from the macroscale view correspond to perfect stacking orders at the atomic level.

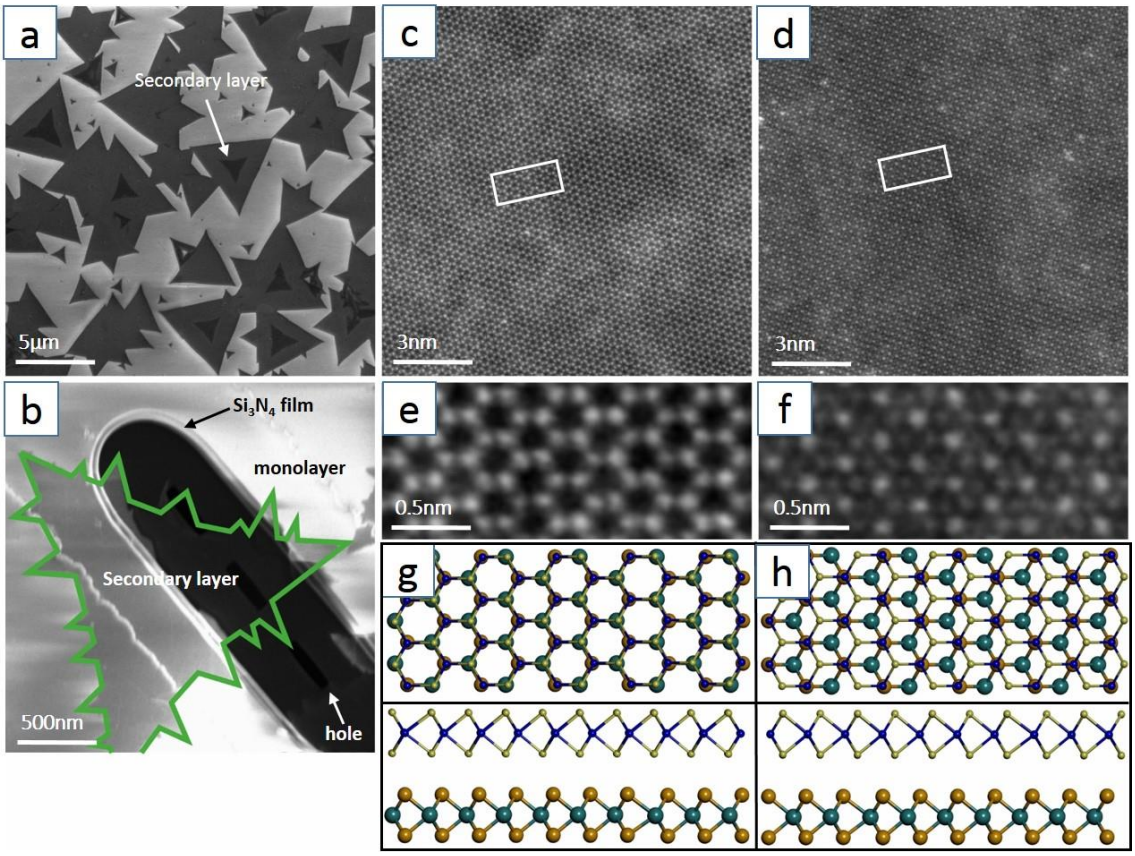

Figure 6-1 (a) SEM image in SE mode showing as-grown MoS_2 monolayers with scattered secondary layers. (b) SEM image showing a MoS_2 bilayer region transferred onto the *in-situ* heating chip with part of the secondary layer suspended on the Si_3N_4 film. (c and d) ADF-STEM images showing two uniformly stacked MoS_2 bilayer regions and corresponding zoomed in images showing (e) 2H and (f) 3R stacking sequences. Atomic models displaying the top and side views of (g) 2H and (h) 3R stacking sequences.

Figure 6-2(a) shows a WS_2 bilayer suspended on a slit in the *in-situ* heating chip. Contrast variations showed up when the sample was heated to 500°C, and the boxed region in Figure 2a is zoomed in in **Figure 6-2**(b) in false color showing the contrast variation. The green boxed area is magnified in **Figure 6-2**(d) showing the mono-bilayer step edge, which evidences that the morphology changes under heating in the bilayer region and the brighter region shows perfect 3R stacking sequence. In addition, **Figure 6-2**(c) shows that the bright region is periodically spaced by dark strips. These strips are nanometers in width and

spaced with an average distance of 25nm as shown in **Figure 6-2**(e), indicating the nanometer-wide transition regions between ordered stacking domains.

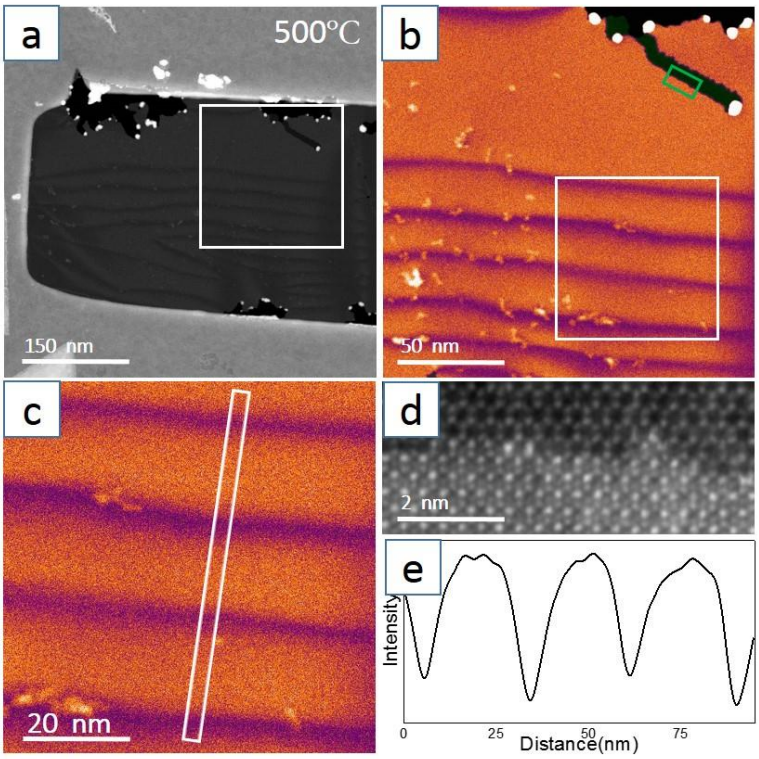

Figure 6-2 (a) Low magnification ADF-STEM image showing a WS_2 bilayer under 500°C and (b and c) corresponding magnified images showing the darker contrast stacking boundaries. (d) High magnification ADF-STEM image showing the mono-bilayer step edge in the green boxed region in b. (e) Line intensity profile taken from c across the ripples.

Figure 6-3(a) shows another MoS_2 monolayer with scattered triangular bilayers suspended on the slit of the *in-situ* heating chip. The yellow boxed area is magnified in **Figure 6-3**(b), showing the monolayer-bilayer step edge. **Figure 6-3**(c-f) displays the same area as boxed in **Figure 6-3**(a) during the *in-situ* heating. The triangular bilayers show uniform configuration under room temperature as shown in **Figure 6-3**(c). **Figure 6-3**(d) shows that upon heated to 300°C, contrast variation comes into scene in the bilayer region, indicating the formation of transition regions, which build up their volume upon heated to

600°C and 900°C as shown in **Figure 6-3**(e) and (f). However, no visible contrast change is observed in the monolayer region, implying that the transition regions form as surface ripples which only reside in the top layer.

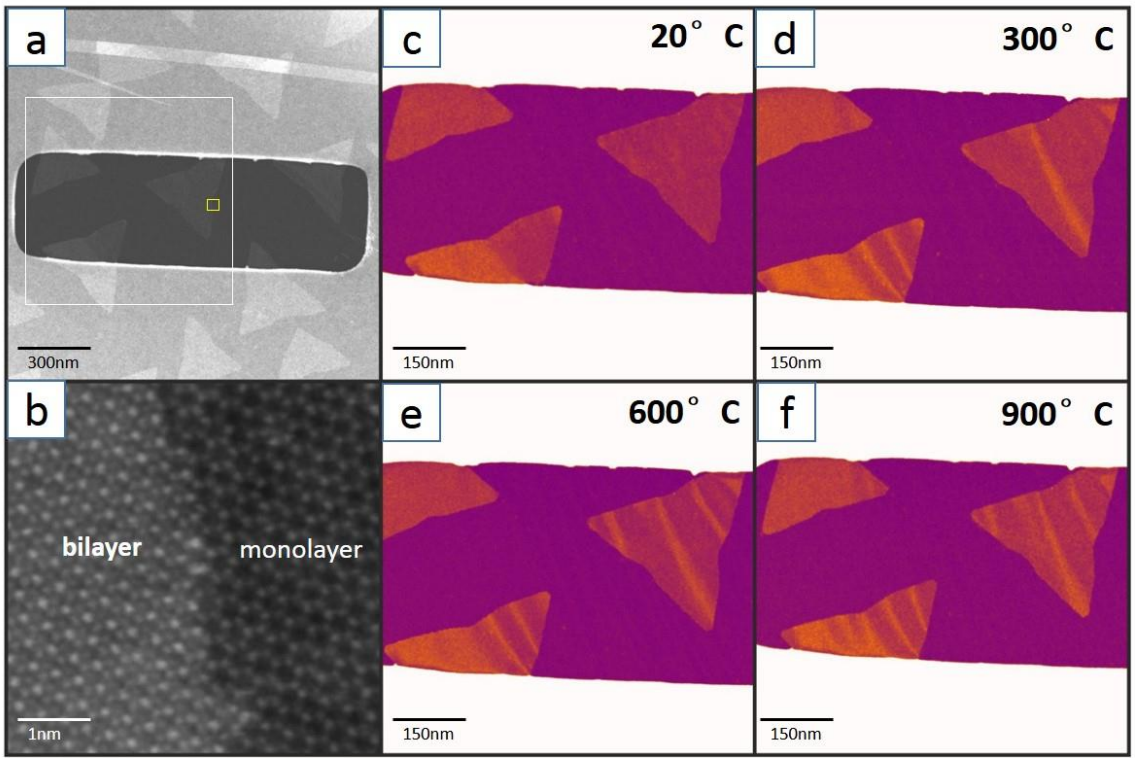

Figure 6-3 (a) Low magnification ADF-STEM image showing a monolayer MoS_2 with scatter secondary layers suspended on the heating chip, the yellow boxed region is zoomed in in (b) showing the monolayer-bilayer step edge. (c-f) The white boxed region in a showing the ripple formation under *in-situ* heating.

6.2.2 Formation Mechanism

Figure 6-4(a) displays a schematic showing a bilayer sample newly transferred onto the *in-situ* heating holder. A residual water layer was formed during the transfer process between the sample and the heating holder. During the sample baking, as the in-plane thermal expansion coefficient (TEC) of MoS_2 bilayer is higher than that of Si_3N_4 film, the sample exhibits more in-plane expansion as shown in **Figure 6-4**(b). However, due to the

lubrication effect of the water layer, no compressive strain is introduced into the bilayer system (**Figure 6-4**(c)). As the sample is cooled down to the room temperature, as indicated in **Figure 6-4**(d), tension is introduced into the bottom layer as the sample contracts more than the heating holder, resulting in the tensile strain in transferred sample.

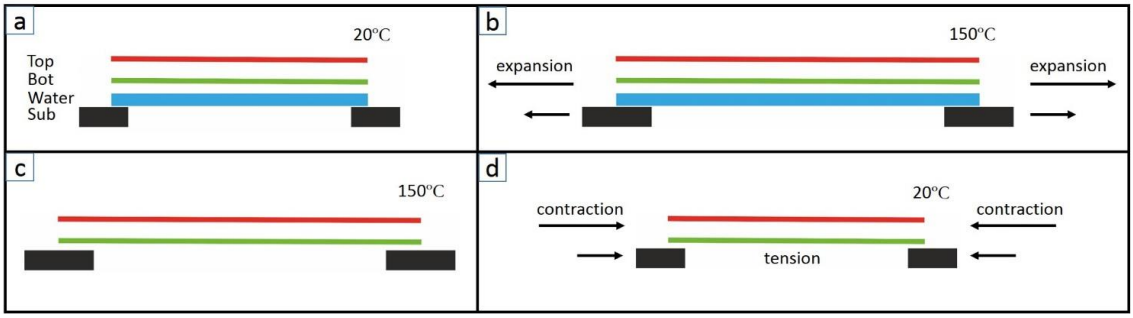

Figure 6-4 Schematics from the side view showing the formation process of residual tensile strain in the bilayer sample transferred onto the *in-situ* heating holder.

Figure 6-5(a-c) show schematics illustrating the formation of surface ripples in the bilayer materials. As explained in **Figure 6-4**, the bilayer sample transferred onto the *in-situ* heating holder has residual tensile strain in the bottom layer (**Figure 6-5**(a)). During *in-situ* heating for ADF-STEM observation, as temperature rises, tensile strain in the bottom layer is gradually released and compressive strain in the top layer builds up (**Figure 6-5**(b)), leading to the formation of surface ripples which are more energetically favorable than condensing all the atoms in the same plane (**Figure 6-5**(c)). **Figure 6-3** displays that no contrast variation was observed in the MoS_2 monolayers on the heating chip upon heating, confirming that the ripples exist only in the top layer of the bilayer system. The corresponding atomic models are shown in **Figure 6-5**(d) and (e). With no compressive strain in the top layer, the bilayer is completely flat and is perfectly stacked as 3R(a) phase, two sulfur columns are selected and circled in red as the references, the distance between

which is L_0. When compressive strain is applied in the top layer along the armchair direction, the secondary layer rises and transition stacking boundaries form. Perfect 3R(a) and 3R(b) stacking sequences are observed in Figure 4e with a transition stacking boundary region with a width of L_1(L_0-a). The relative lattice shift of a (1.82Å) introduced by the out-of-plane dislocation in the top layer over a distance of L_1 results in the stacking sequence swapping from 3R(a)-3R(a) to 3R(a)-3R(b) and a ripple in between with the width of L_0-a. In this case, the compressive strain in the top layer is calculated as $\frac{a}{L0} = \frac{a}{18a} = \frac{1}{18}$=5.6% and released due the to the ripple formation.

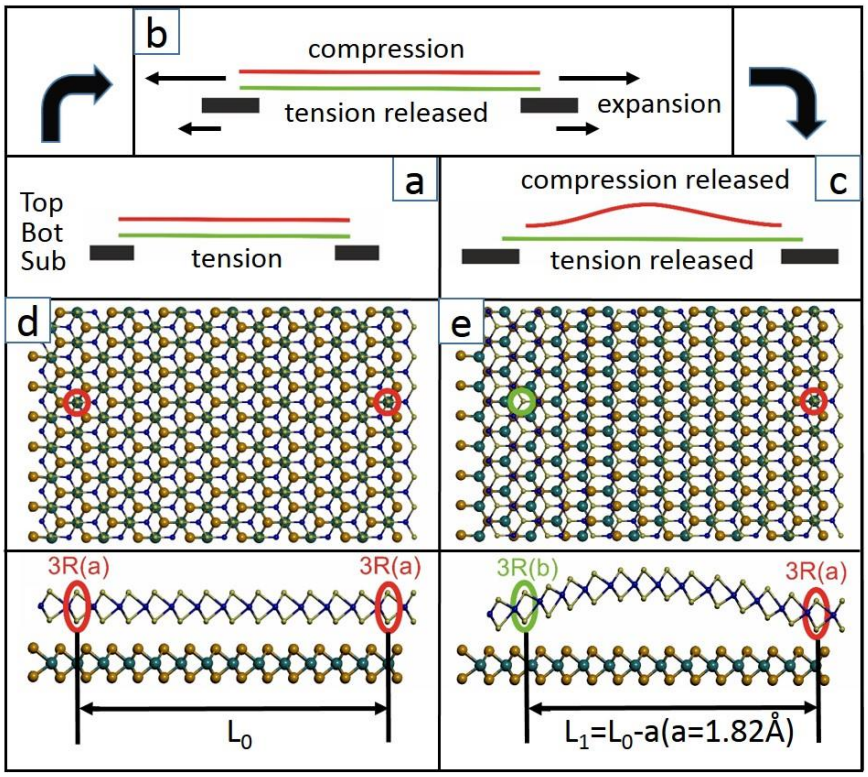

Figure 6-5 (a-c) Schematics from the side view showing the formation process of ripples under sample heating. Atomic models from both top and side views showing the stacking sequences of the bilayer system with (d) no strain (e) a ripple in the top layer.

6.2.3 Atomic Structures

In order to further visualize the detailed atomic structures of the transition stacking boundaries, a bilayer region with both transition regions and ordered stacking regions is observed under 500°C and displayed in **Figure 6-6**(a), the boxed area is taken a closer observation in **Figure 6-6**(b), indicating that the contrast difference from the macroscale view is attributed to the lattice registration difference between the 3R stacking and stacking boundaries. High magnification ADF-STEM image in **Figure 6-6**(c) is taken across the transition region, with both ends showing 3R stacking sequences. Taking the Sulfur atoms as the references, the distance between the most neighboring 3R phases is measured as 9.04nm, also indicating the width of the transition region. A reasonable atomic model of a bilayer system with a ripple in the top layer is constructed, the 3D, top and side views are shown in **Figure 6-6**(d). Corresponding ADF-STEM image simulation in Figure 5e shows similar morphology with that in **Figure 6-6**(c), with 3R phases on both ends and dot-like Moiré pattern in between. Their detailed structure configurations from both experimental and simulated results are displayed in **Figure 6-6**(f-h) and **Figure 6-6**(i-k), respectively. The distance of the stacking boundary is calculated as 9.10nm, which matches well with our experimental result, confirming that the brighter region is 3R stacked and the dark strip is transition stacking boundary with non-perfect stacking order. In such case, the applied local compressive strain in the top layer due to heating is calculated as $\frac{a}{L0} = \frac{a}{L1+a} = \frac{a}{L1+a'}$, which is 1.96% for simulation and 1.97% for the experiment.

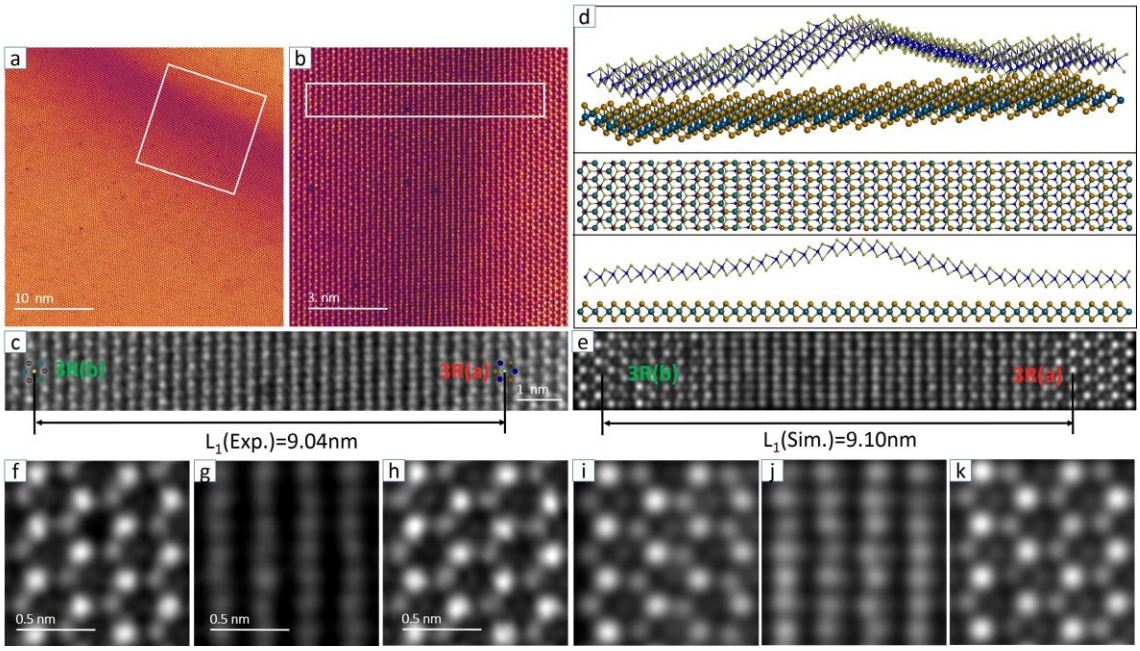

Figure 6-6 (a) Low magnification ADF-STEM image of a MoS_2 bilayer region under 500° C showing both ordered stacking domains and transition regions, the boxed area is zoomed in in (b) showing lattice registration. (c) Higher magnification ADF-STEM image taken from the boxed region in b showing 3R stacking sequences with boundaries.

Figure 6-7 and **Figure 6-8** show similar rippling morphologies and corresponding local lattice registration of more WS_2 and MoS_2 samples under different temperature *in-situ* observation. **Figure 6-7**(a) shows a MoS_2 bilayer region under 900°C *in-situ* observation. Surface ripples are distinguished by their contrast difference from the ordered stacking regions. The boxed region is zoomed in in **Figure 6-7**(b) to show the local lattice registration, indicating different stacking sequences. High magnification ADF-STEM images in **Figure 6-7**(c) is taken across the transition region, with both ends showing 3R stacking sequences. **Figure 6-7**(d-f) are taken from **Figure 6-7**(c) and magnified to show the stacking sequences.

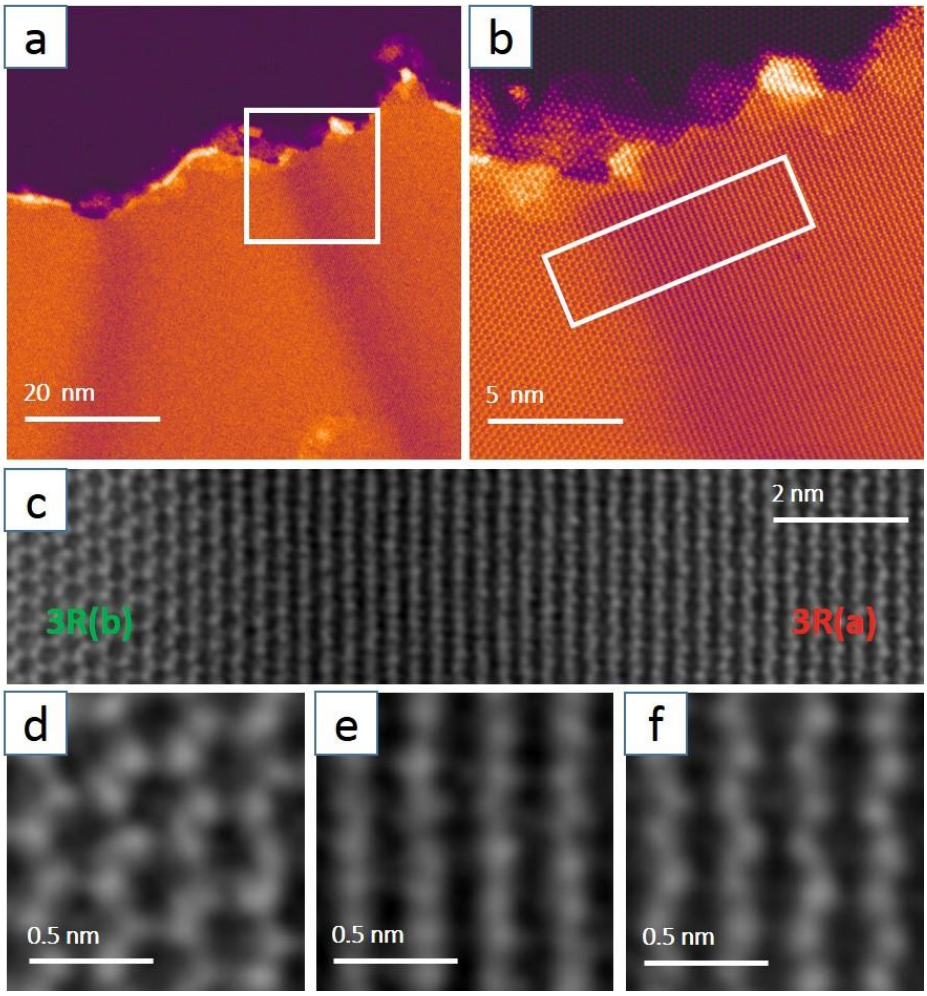

Figure 6-7 (a) Low magnification ADF-STEM image showing both ordered stacking domains and transition regions in a MoS_2 bilayer under 900°C, the boxed area is zoomed in in (b) showing lattice registration. (c) High magnification ADF-STEM image taken from the boxed region in b showing 3R stacking sequences with boundaries. (d-f) High magnification ADF-STEM image taken from c.

Figure 6-8(a) shows a WS_2 bilayer region under 500°C *in-situ* observation. Surface ripples are distinguished by their contrast difference from the ordered stacking regions. The boxed region is zoomed in in **Figure 6-8**(b) to show the local lattice registration, indicating different stacking sequences. High magnification ADF-STEM images in **Figure 6-8**(c) is taken across the transition region, with both ends showing perfect stacking sequences

which are denoted as 2H and AA stacking in this case. **Figure 6-8**(d-f) are taken from **Figure 6-8**(c) and magnified to show the stacking sequences.

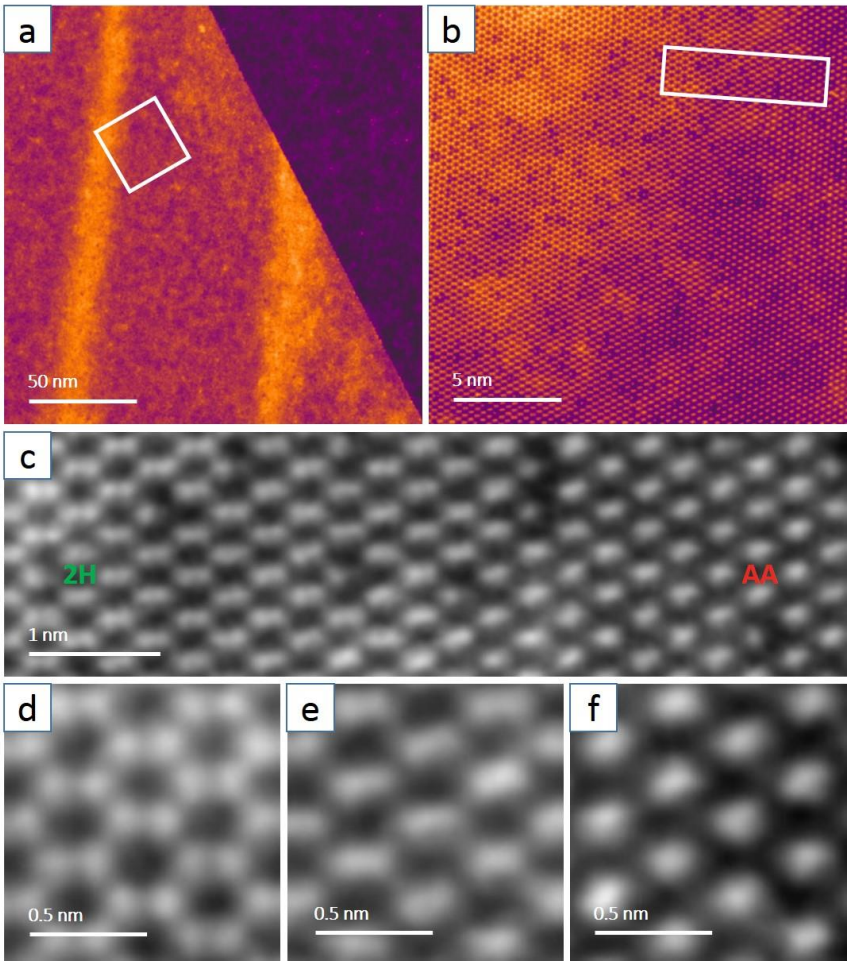

Figure 6-8 (a) Low magnification ADF-STEM image showing both ordered stacking domains and transition regions in a WS_2 bilayer under 500°C, the boxed area is zoomed in in (b) showing lattice registration. (c) High magnification ADF-STEM image taken from the boxed region in b showing 2H and AA stacking sequences with boundaries. (d-f) High magnification ADF-STEM image taken from c.

6.2.4 Dynamics upon *in-situ* Heating

We further studied the behavior of these ripples under heating and cooling cycles. As shown in **Figure 6-9**(a), a MoS_2 bilayer suspended on the *in-situ* heating chip is observed

from a nanometer scale, the step edge in the boxed area in **Figure 6-9**(b) evidences the rippling morphology existing in the bilayer region. A specific region is chosen and displayed in color from **Figure 6-9**(c-i) as a function of temperature. Line profiles were taken across the ripples and shown in **Figure 6-9**(j-l), respectively. The average FWHM of ripples under each temperature is shown in **Figure 6-9**(m). Noticeably, the ripples were gradually diminished when the sample was cooled down and completely annihilated under room temperature, and gradually came back and built up width with rising temperature, which is indicated by the FWHM, confirming that the rippling morphology in the bilayer system is attributed to the strain applied. Due to the in-plane thermal expansion coefficient (TEC) difference between MoS_2 bilayers and the Si_3N_4 film as mentioned above, compressive strain applied to the sample is positively correlated with the temperature. The ripples under 300°C and 600°C are randomly distributed and oriented whereas they are more likely to follow the dopant distribution under 1000°C, as these dopants may work as pining sites for the rippling morphology.

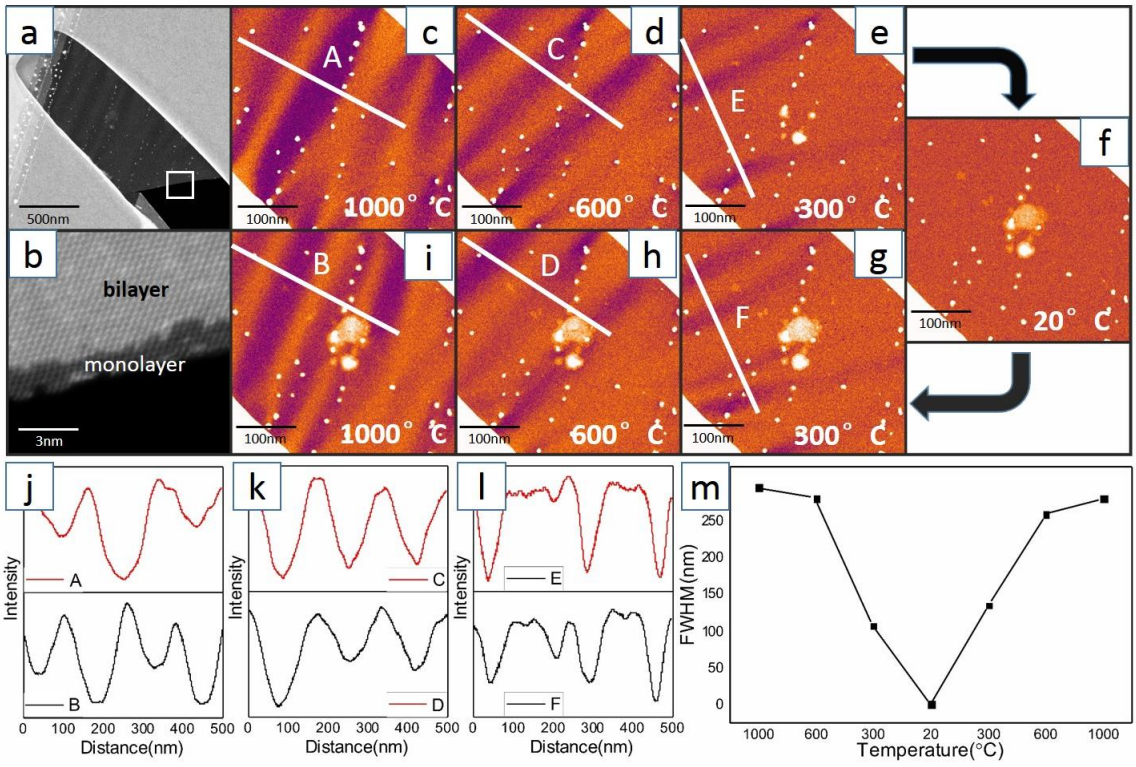

Figure 6-9 (a) Low magnification ADF-STEM image showing a bilayer MoS_2 suspended on the *in-situ* heating chip, the boxed region is zoomed in in (b) showing the monolayer-bilayer step edge. (c-i) The same region showing the reversibility of ripples during cooling and heating. The transition regions are quantitatively analyzed by taking line intensity profile as shown in (j-l), respectively. (m) The FWHM of the transition regions as a function of temperature.

6.2.5 Dynamics under Prolonged Beam Irradiation

To understand the behavior of ripples under prolonged beam irradiation, we take another WS_2 bilayer sample under 500°C as shown in **Figure 6-10**(a) and observed the rippling region for 15s as shown in **Figure 6-10**(b) and (c). The boxed region in **Figure 6-10**(b) shows two perfect stacking sequences spaced by a trainstion region with a few nanometer width along armchair direction. After 15s of observation, the local lattice registration of the same region switches into two perfect stacking sequences with an atomically sharp interface. Atomic models are conducted in **Figure 6-10**(f-h), showing the relaxation of the

ripples due to missing one line of surphur atoms. Corresponding ADF-STEM image simulations in **Figure 6-10**(i) and (k) well match the experimental results, as an indicator that the transition region and the sharp interface in **Figure 6-10**(d) and (e) are attributed to ripples and line defects in the top layer, respectively. The formation of the line defect under prolonged beam irradiation is a processs to release the residual compressive strain in the ripples.

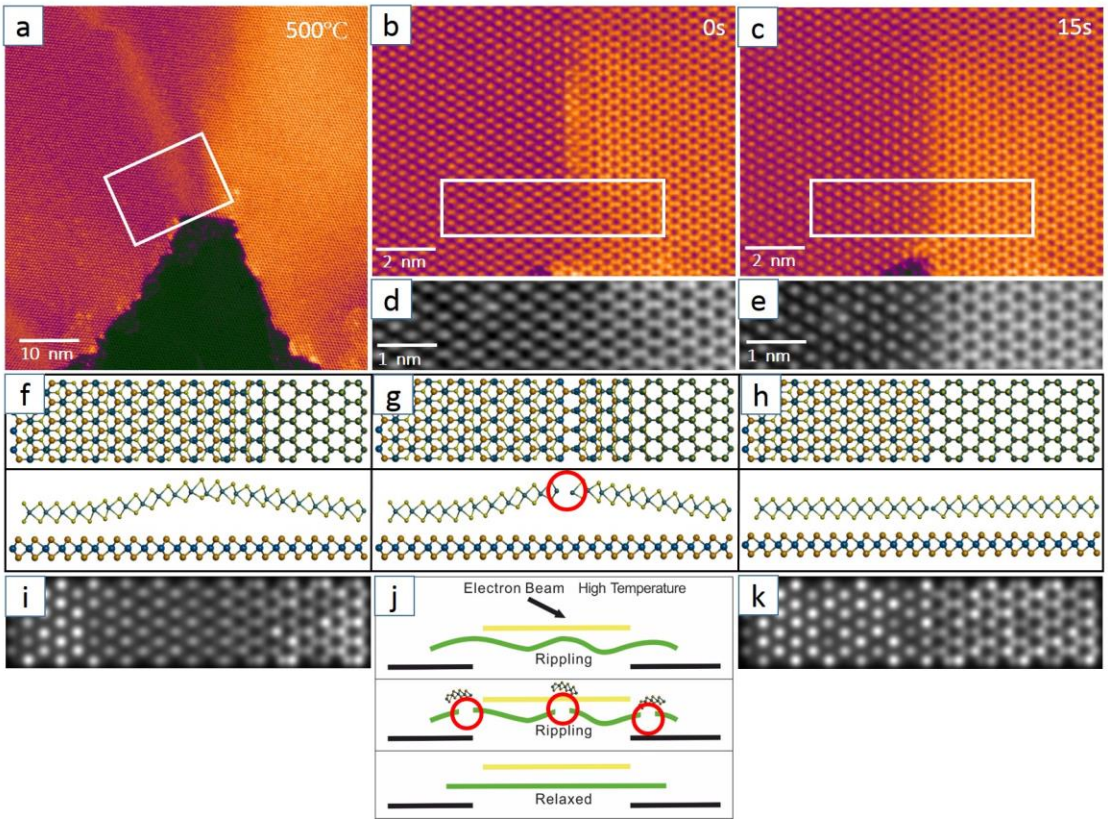

Figure 6-10 (a) Low magnification ADF-STEM image showing a rippled WS_2 bilayer under 500°C. (b-c) boxed region in a under prolonged beam irradiation. (d-e) High magnification ADF-STEM images taken from the boxed areas in b and c, respectively. (f-h) Atomic models showing the relaxation of ripples due to missing one line of sulfur atoms and (i and k) corresponding image simulations. (j) Schematic illustration showing the process of ripple relaxation under prolonged beam irradiation

6.2.6 Interaction with Holes in Top Layer

Finally, we also observerd several MoS_2 samples with triangular holes in the top layer as shown in **Figure 6-11**(a). Upon heated to 700°C, irragular wrinkles rather than periodically-spaced ripples come into scene, which can be distinguished by the irregular contrast in **Figure 6-11**(b). This is caused by both the compressive strain introduced by heating and also the nonuniformity of the top layer in the first place due to the existence of holes. The boxed region was taken a closer observation in **Figure 6-11**(c), showing that between two triangular holes in the top layer, the ripples or wrinkles show different mophologies and orientations. Line profiles in **Figure 6-11**(d) taken across the ripples indicate that the they have different widths and are nonuniformly spaced. Image frames taken from a wrinkled region are displayed in **Figure 6-11**(e-h), showing the fading and vanishing of the ripples under prolonged beam irradiation. The wrinkles are also relaxed with the aggregation of vacancies and line defects

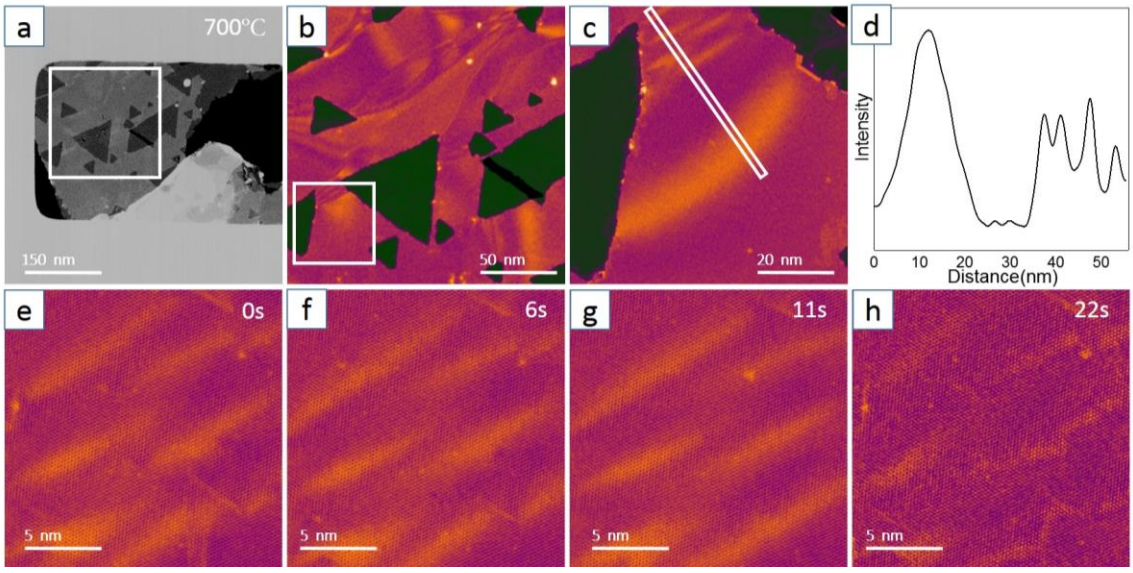

Figure 6-11 (a) Low magnification ADF-STEM image showing a MoS_2 bilayer suspended on a heating chip with triangular holes in the top layer, the boxed region is zoomed in the (b) showing

the wrinkles. (c) Magnified images taken from b showing the non-periodically spaced and shaped wrinkles and (d) corresponding line intensity profile. (e-h) ADF-STEM image frames showing the evolution of wrinkles under beam irradiation as a function of time.

6.3 Conclusion

We have observed the formation of periodically spaced transition regions in a perfectly stacked MoS_2 and WS_2 bilayer under 500°C. The stacking boundaries are confirmed to be surface ripples existing in the top layer of the bilayer system. The ripples are formed due to the compressive strain introduced into the bilayer system upon heating, which is attributed to the thermal expansion coefficient difference between the substrate and the 2D materials. The local lattice registration of the rippling is dot-like moiré pattern which contributes to its distinct contrast from the macroscale review. We also demonstrated that these ripples are highly reversible under heating and cooling cycles. The ripples disappear under room temperature due to the compressive strain fully released. Under prolonged beam irradiation, ripples are relaxed due to the introduction of line defects, which release the residual compressive strain in the bilayer system. Overall, we present a compressive study across length scales from discrete atoms to the macroscopic continuum of the ripples in TMD bilayers as well as their dynamics, which will help guide the understanding of their structure-property correlation.

6.4 References

(1) Ci, P.; Chen, Y.; Kang, J.; Suzuki, R.; Choe, H.S.; Suh, J.; Ko, C.; Park, T.; Shen, K.; Iwasa, Y. and Tongay, S. Quantifying van der Waals Interactions in Layered Transition Metal Dichalcogenides from Pressure-Enhanced Valence Band Splitting. *Nano letters.* **2017**, 17, 4982-4988.

(2) Splendiani, A.; Sun, L.; Zhang, Y.; Li, T.; Kim, J.; Chim, C.Y.; Galli, G. and Wang,

F. Emerging Photoluminescence in Monolayer MoS_2. *Nano letters*. **2010**, 10, 1271-1275.

(3) He, J.; Hummer, K. and Franchini, C. Stacking effects on the electronic and optical properties of bilayer transition metal dichalcogenides MoS_2, $MoSe_2$, WS_2, and WSe_2. *Physical Review B*. **2014**, 89, 075409.

(4) Li, H.; Zhang, Q.; Yap, C.C.R.; Tay, B.K.; Edwin, T.H.T.; Olivier, A. and Baillargeat, D. From Bulk to Monolayer MoS_2: Evolution of Raman Dcattering. *Advanced Functional Materials*. **2012**, 22, 1385-1390.

(5) Li, H.; Yin, Z.; He, Q.; Li, H.; Huang, X.; Lu, G.; Fam, D.W.H.; Tok, A.I.Y.; Zhang, Q. and Zhang, H. Fabrication of Single and Multilayer MoS_2 Film-based Field-effect Transistors for Sensing NO at Room Temperature. *Small*. **2012**, 8, 63-67.

(6) Late, D.J.; Huang, Y.K.; Liu, B.; Acharya, J.; Shirodkar, S.N.; Luo, J.; Yan, A.; Charles, D.; Waghmare, U.V.; Dravid, V.P. and Rao, C.N.R. Sensing Behavior of Atomically Thin-layered MoS_2 Transistors. *ACS Nano*. **2013**, 7(6), 4879-4891.

(7) Liu, K.; Zhang, L.; Cao, T.; Jin, C.; Qiu, D.; Zhou, Q.; Zettl, A.; Yang, P.; Louie, S.G. and Wang, F. Evolution of Interlayer Coupling in Twisted Molybdenum Disulfide Bilayers. *Nature communications*. **2014**, 5, 4966.

(8) Van Der Zande, A.M.; Kunstmann, J.; Chernikov, A.; Chenet, D.A.; You, Y.; Zhang, X.; Huang, P.Y.; Berkelbach, T.C.; Wang, L.; Zhang, F. and Hybertsen, M.S. Tailoring the Electronic Structure in Bilayer Molybdenum Disulfide via Interlayer Twist. *Nano letters*. **2014**, 14, 3869-3875.

(9) Suzuki, R.; Sakano, M.; Zhang, Y.J.; Akashi, R.; Morikawa, D.; Harasawa, A.; Yaji, K.; Kuroda, K.; Miyamoto, K.; Okuda, T. and Ishizaka, K. Valley-dependent Spin Polarization in Bulk MoS_2 with Broken Inversion Symmetry. *Nature nanotechnology*. **2014**, 9, 611.

(10) Wilson, J.A. and Yoffe, A.D. The Transition Metal Dichalcogenides Discussion and Interpretation of the Observed Optical, Electrical and Structural Properties. *Advances in Physics*. **1969**, 18, 193-335.

(11) Xia, M.; Li, B.; Yin, K.; Capellini, G.; Niu, G.; Gong, Y.; Zhou, W.; Ajayan, P.M. and Xie, Y.H. Spectroscopic Signatures of AA' and AB Stacking of Chemical Vapor Deposited Bilayer MoS_2. *ACS nano*. **2015**, 9, 12246-12254.

(12) Lee, J.U.; Kim, K.; Han, S.; Ryu, G.H.; Lee, Z. and Cheong, H. Raman Signatures of Polytypism in Molybdenum Disulfide. *ACS nano*. **2016**, 10, 1948-1953.

(13) Shmeliov, A.; Shannon, M.; Wang, P.; Kim, J.S.; Okunishi, E.; Nellist, P.D.; Dolui, K.; Sanvito, S. and Nicolosi, V. Unusual Stacking Variations in Liquid-phase

Exfoliated Transition Metal Dichalcogenides. *ACS nano*. **2014**, 8, 3690-3699.

(14) Levita, G.; Cavaleiro, A.; Molinari, E.; Polcar, T. and Righi, M.C. Sliding Properties of MoS_2 Layers: Load and Interlayer Orientation Effects. *The Journal of Physical Chemistry C*. **2014**, 118, 13809-13816.

(15) Liu, K.; Zhang, L.; Cao, T.; Jin, C.; Qiu, D.; Zhou, Q.; Zettl, A.; Yang, P.; Louie, S.G. and Wang, F. Evolution of Interlayer Coupling in Twisted Molybdenum Disulfide Bilayers. *Nature communications*. **2014**, 5, 4966.

(16) Xia, J.; Zeng, Q.; Zhou, J.; Zhou, W.; Zhang, Q.; Yan, J.; Liu, Z. and Shen, Z.X. Current Rectification and Ssymmetric Photoresponse in MoS_2 Stacking-induced Homojunctions. *2D Materials*. **2017**, 4, 035011.

(17) Zhou, S.; Wang, S.; Shi, Z.; Sawada, H.; Kirkland, A.I.; Li, J. and Warner, J.H. Atomically Sharp Interlayer Stacking Shifts at Anti-phase Grain Boundaries in Overlapping MoS_2 Secondary Layers. *Nanoscale*. **2018**, 10, 16692-16702.

(18) Lin, J.; Fang, W.; Zhou, W.; Lupini, A.R.; Idrobo, J.C.; Kong, J.; Pennycook, S.J. and Pantelides. AC/AB Stacking Boundaries in Bilayer Graphene. *Nano letters*. **2013**, 13, 3262-3268.

(19) Brown, L.; Hovden, R.; Huang, P.; Wojcik, M.; Muller, D.A. and Park, J. Twinning and Twisting of Tri-and Bilayer Graphene. *Nano letters*. **2012**, 12, 1609-1615.

(20) Hibino, H.; Mizuno, S.; Kageshima, H.; Nagase, M. and Yamaguchi, H. Stacking Domains of Epitaxial Few-layer Graphene on SiC (0001). *Physical Review B*. **2009**, 80, 085406.

(21) Tapasztó, L.; Dumitrică, T.; Kim, S.J.; Nemes-Incze, P.; Hwang, C. and Biró, L.P. Breakdown of Continuum Mechanics for Nanometre-wavelength Rippling of Graphene. *Nature physics*. **2012**, 8, 739.

(22) Brivio, J.; Alexander, D.T. and Kis, A. Ripples and Layers in Ultrathin MoS_2 Membranes. *Nano letters*. **2011**, 11, 5148-5153.

(23) Kushima, A.; Qian, X.; Zhao, P.; Zhang, S. and Li, J. Ripplocations in van der Waals Layers. *Nano letters*. **2015**, 15, 1302-1308.

(24) Lui, C.H.; Liu, L.; Mak, K.F.; Flynn, G.W. and Heinz, T.F. Ultraflat Graphene. *Nature*. **2009**, 462, 339.

(25) Bonilla, L.L. and Carpio, A. Model of Ripples in Graphene. *Physical Review B*. **2012**, 86, 195402.

(26) Deng, S. and Berry, V. Wrinkled, Rippled and Crumpled Graphene: An Overview

of Formation Mechanism, Electronic Properties, and Applications. *Materials Today*. **2016**, 19, 197-212.

(27) Vasić, B.; Zurutuza, A. and Gajić, R. Spatial Variation of Wear and Electrical Properties across Wrinkles in Chemical Vapour Deposition Graphene. *Carbon*. **2016**, 102, 304-310.

(28) Schiefele, J.; Martin-Moreno, L. and Guinea, F. Faraday Effect in Rippled Graphene: Magneto-optics and Random Gauge Fields. *Physical Review B*. **2016**, 94, 035401.

(29) Liang, T.; He, G.; Wu, X.; Ren, J.; Guo, H.; Kong, Y.; Iwai, H.; Fujita, D.; Gao, H.; Guo, H. and Liu, Y. Permeation through Graphene Ripples. *2D Materials*. **2017**, 4, 025010.

(30) He, K.; Poole, C.; Mak, K.F. and Shan, J. Experimental Demonstration of Continuous Electronic Structure Tuning via Strain in Atomically Thin MoS_2. *Nano letters*. **2013**, 13, 2931-2936.

(31) Lin, Z.; Carvalho, B.R.; Kahn, E.; Lv, R.; Rao, R.; Terrones, H.; Pimenta, M.A. and Terrones, M. Defect Engineering of Two-dimensional Transition Metal Dichalcogenides. *2D Materials*. **2016**, 3, 022002.

(32) De Juan, F.; Cortijo, A. and Vozmediano, M.A. Charge Inhomogeneities due to Smooth Ripples in Graphene Sheets. *Physical Review B*. **2007**, 76, 165409.

(33) Herbut, I.F.; Juričić, V. and Vafek, O. Coulomb Interaction, Ripples, and the Minimal Conductivity of Graphene. *Physical review letters*. **2008**, 100, 046403.

(34) Guinea, F.; Horovitz, B. and Le Doussal, P. Gauge Field Induced by Ripples in Graphene. *Physical Review B*. **2008**, 77, 205421.

(35) Guinea, F.; Horovitz, B. and Le Doussal, P. Gauge Field Induced by Ripples in Graphene. *Physical Review B*. **2008**, 77, 205421.

(36) Guinea, F.; Horovitz, B. and Le Doussal, P. Gauge Fields, Ripples and Wrinkles in Graphene layers. *Solid State Communications*. **2009**, 149, 1140-1143.

(37) Guinea, F.; Katsnelson, M.I. and Geim, A.K. Energy Gaps and a Zero-field Quantum Hall Effect in Graphene by Strain Engineering. *Nature Physics*. **2010**, 6, 30.

(38) Zhou, S.; Wang, S.; Li, H.; Xu, W.; Gong, C.; Grossman, J.C. and Warner, J.H. Atomic Structure and Dynamics of Defects in 2D MoS_2 Bilayers. *ACS Omega*. **2017**, 2, 3315-3324.

(39) Tien, C.L. and Lin, T.W. Thermal Expansion Coefficient and Thermomechanical

Properties of SiN_x Thin Films Prepared by Plasma-enhanced Chemical Vapor Deposition. *Applied optics*. **2012**, 51, 7229-7235.

(40) Gan, C.K. and Liu, Y.Y.F. Direct Calculation of the Linear Thermal Expansion Coefficients of MoS_2 via Symmetry-preserving Deformations. *Physical Review B*. **2016**, 94, 134303.

(41) Bano, A.; Khare, P. and Gaur, N.K. Thermal Transport Properties of Bulk and Monolayer MoS_2: An ab-initio Approach. In Journal of Physics: *Conference Series*. **2017**, 836, 012052.

(42) Ding, Y. and Xiao, B. Thermal Expansion Tensors, Grüneisen Parameters and Phonon Velocities of Bulk MT_2 (M= W and Mo; T= S and Se) from first principles calculations. *Rsc Advances*. **2015**, 5, 18391-18400.

(43) Hosokawa, F.; Sawada, H.; Kondo, Y.; Takayanagi, K.; Suenaga, K. Development of Cs and Cc Correctors for Transmission Electron Microscopy Microscopy. *Microscopy*. **2013**, 62, 23-41.

Chapter 7

Conclusion and future work

7.1 Conclusion

This doctorate projects focuses on a systematical and comprehensive studies of TMD bilayers, especially MoS_2 and WS_2. I am particularly interested in investigating different stacking possibilities both theoretically and experimentally of these 2D materials when an extra layer degree of freedom is added. For their superior properties over the monolayer counterparts in future device applications, a detailed study in observing, analyzing and controlling of defective structures is also conducted to differentiate from those in monolayers. To begin with, in Chapter 4, through AC-TEM imaging the production of point defects and their aggregation into line defects in bilayer MoS_2, we prove the different production and migration mechanisms between sulfur vacancies in monolayer and bilayer system and reveal that the main discrepancy between defective monolayer and bilayer system is the out-of-plane lattice distortion. The ability for the bilayer sheet to accommodate the buckling and compression caused by line defects can be assigned to the competition between compression in one layer from the loss of S atoms and the interlayer van der Waals force.

In Chapter 5, we moved forward to a more complex line defect, the grain boundary, specifically the antiphase GB existing in the MoS_2 bilayers. We have demonstrated that the propagation of an antiphase GB from a MoS_2 monolayer into a bilayer region causes atomically sharp stacking changes from 2H-3R, which is reversed upon a second antiphase

GB crossing. Antiphase GBs within the monolayer section can propagate with arbitrary direction by the combination of 4-fold and 8-fold rings, where the ratio depends upon GB angle relative to the zig-zag lattice direction of MoS_2. Large turning angles of the antiphase GB were also observed and are mediated by a specific 8-member ring defect that has different positions of the attaching 4-member rings. Antiphase GBs in the MoS_2 bilayer region exhibit larger lattice shrinkage along the Mo-Mo direction compared to the pure monolayers which is confirmed by DFT calculations. Overall, our data show that there is an energetic competition between a perfect 2H-3R stacking interface and buckling, in which interlayer van der Waals forces cause a reduction in buckling in MoS_2 due to antiphase GBs in order to achieve atomically sharp 2H-3R stacking sequences in the bilayer. These results provide a detailed characterization of antiphase GBs in monolayer MoS_2.

Ripples, as one of the 2D defects, were theoretically studied in monolayer and few-layer TMDs, but scarcely experimentally observed or investigated. In Chapter 6, We have observed the formation of periodically spaced transition regions in a perfectly stacked MoS_2 and WS_2 bilayer under 500°C. The stacking boundaries are confirmed to be surface ripples existing in the top layer of the bilayer system. The ripples are formed due to the compressive strain introduced into the bilayer system upon heating, which is attributed to the thermal expansion coefficient difference between the substrate and the 2D materials. The local lattice registration of the rippling is dot-like moiré pattern which contributes to its distinct contrast from the macroscale review. We also demonstrated that these ripples are highly reversible under heating and cooling cycles. The ripples disappear under room temperature due to the compressive strain fully released. Under prolonged beam irradiation, ripples are relaxed due to the introduction of line defects, which release the residual

compressive strain in the bilayer system. Overall, we present a compressive study across length scales from discrete atoms to the macroscopic continuum of the ripples in TMD bilayers as well as their dynamics, which will help guide the understanding of their structure-property correlation.

7.2 Future Work

To expand my current research, I would like to take another three approaches. The first is to apply my current research methodologies and outcomes to TMD bilayers other than MoS_2 and WS_2 bilayers, to explore how defects could behavior differently in these bilayer systems. I would also deepen my understanding of TEMs and relevant imaging techniques, which, as the most advanced method for atomic-level study of nanomaterials, could lead me to reveal the structures and behaviors of more complex defects in both monolayer and few-layer 2D materials. Finally, through controlled nanoengineering of defects ranging from vacancies to ripples, I am thrilled to figure out how these defects and the stacking sequences in bilayer system could exert influences on their optical, mechanical and chemical properties, and find their application in device uses.